

DESIGN AND MANUFACTURING OF FLEXIBLE
OPTICAL AND MECHANICAL METAMATERIALS

A Dissertation

Submitted to the Faculty

of

Purdue University

by

Debkalpa Goswami

In Partial Fulfillment of the

Requirements for the Degree

of

Doctor of Philosophy

August 2020

Purdue University

West Lafayette, Indiana

**THE PURDUE UNIVERSITY GRADUATE SCHOOL
STATEMENT OF DISSERTATION APPROVAL**

Dr. Ramses V. Martinez, Chair

School of Industrial Engineering

Dr. Karthik Ramani

School of Mechanical Engineering

Dr. Mohit S. Verma

Department of Agricultural & Biological Engineering

Dr. Wenzhuo Wu

School of Industrial Engineering

Approved by:

Dr. Abhijit V. Deshmukh

Head of the School Graduate Program

ACKNOWLEDGMENTS

Over the past five years, several individuals have contributed, directly or indirectly, to my research efforts and without whose support this dissertation would not have seen the light of day. This is an opportune moment for me to place on record my gratitude for them.

At first, I would like to express my deepest appreciation and sincerest gratitude toward my advisor, Prof. Ramses V. Martinez, for his expert guidance and constructive criticism, as well as for being a constant source of inspiration throughout my PhD journey. When I first arrived at Purdue in 2015, I had almost no “wet lab” skills. I will be forever indebted to Prof. Martinez for personally providing me with innumerable hours of hands-on training, working late hours with me at the lab bench. He also encouraged me to always keep acquiring new skills and broaden my domain of expertise—my PhD research experience has been truly interdisciplinary and diverse thanks to him. His tireless pursuit of innovative ideas, attention to detail, and transparent prose has profoundly influenced both my sentiments and my professionalism. I intend to pay it forward.

I thank Prof. Karthik Ramani, Prof. Wenzhuo Wu, and Prof. Mohit Verma for kindly volunteering their time to serve on my dissertation committee, and for providing valuable feedback on my research. I am also grateful to Prof. Ramani for enabling valuable collaborations with Luis Paredes and Javier Belmonte—members of the C-Design Lab—on wearable devices and machine learning.

I was fortunate to work with several helpful and supportive lab-mates at the FlexiLab—Aniket, Ben, Bikram, Juan Camilo, Marina, and Sheng—all of whom I collaborated with professionally and learnt a lot from personally. I also had the opportunity to mentor several talented undergraduate and masters students, each of whom made significant contributions to at least one of my research projects: Abdul, Caio Lui, Hugo, Lucas, Nahrin, Omar, Sahil, Shuai, and Vlad.

I thank Dr. Kenneth Kesler, Dr. Caleb Matthews, and Dr. Peter Jenkins, of the Indiana University School of Medicine, for providing me with the invaluable opportunity to work in their surgical skills laboratory. I look forward to continuing fruitful collaborations with them. I also thank Prof. Pablo Zavattieri for making mechanical testing equipment in his lab available for my research, and Dr. Yunlan Zhang for teaching me the nuances of finite element simulations.

Although my PhD journey formally started in August 2015, several important individuals actively shaped my academic pursuits through my high-school and undergraduate days. I am eternally grateful to: my early mentors Diptendu Ray and Dr. Debasis Barman, who never allowed me to fall into the abyss of mediocrity; Prof. Shankar Chakraborty (Jadavpur University, India), with whom I first learned the art of scientific research; Dr. Anoop Mukhopadhyay and Dr. Payel Bandyopadhyay (Central Glass & Ceramic Research Institute, India), who trusted me with expensive equipment in their lab and gave me my first experimental research experience. I also thank Dr.-Ing. Ingrid Rügge and Dr.-Ing. Torsten Hildebrandt (Universität Bremen, Germany) for their mentorship and support.

West Lafayette life tends to become mundane. Thank you to Prakash Chakraborty and Aniket Pal for being such amazing roommates and for their companionship through the frustrating and difficult times.

Finally, to my family.

Dr. Suvajyoti Guha, thank you for providing continued motivation right from my childhood and for being someone I could always look up to.

My mother and father have sacrificed a lot to bring me up. My achievements have been, and will continue to be, a reflection of their love. Although words of gratitude will never justify their contribution, I thank them for their relentless spontaneous support and sacrifice of personal gratifications towards the realization of my own academic ambitions. I know they are very proud of me, and that gives me immense happiness.

Ishita has stood by me through thick and thin, and supported me unconditionally. This is just the beginning, and I look forward to our many wonderful years together.

-DG

TABLE OF CONTENTS

	Page
LIST OF FIGURES	viii
ABSTRACT	xii
1 INTRODUCTION	1
1.1 Motivation	1
1.2 Background and Literature Review	2
1.2.1 Challenges in Scalable Fabrication of Metallic Nanostructures	2
1.2.2 Soft-Lithographic and Imprint-based Nanopatterning Techniques	2
1.2.3 Lasers as Micro- and Nanofabrication Tools	3
1.2.4 Soft Machines and Current Design Challenges	4
1.2.5 Need for Architected, Mechanical Metamaterial-based Soft Robots	4
1.2.6 Exploiting Mechanical Instabilities for Soft Robotic Actuation	5
1.2.7 Magnetic and Tendon-based Actuation Mechanisms	5
1.2.8 Approaches to Manufacture Soft Robots and Mechanical Metamaterials	6
1.2.9 Achieving Compression-Twist Coupling with Mechanical Metamaterials	6
1.3 Organization of this thesis	7
2 ROLL-TO-ROLL NANOFORMING OF METALS USING LASER-INDUCED SUPERPLASTICITY	8
2.1 Introduction	8
2.2 Rationale for the use of CO ₂ lasers in nanomanufacturing	8
2.3 Results	9
2.3.1 Pilot Line for Roll-to-Roll Nanofforming of Metals	9
2.3.2 Selective Nanofforming, Welding, and Cutting	15
2.3.3 Conditions for Nanofforming, Welding, and Cutting using R2RLIS	18
2.3.4 Nanoscale Deformation Mechanisms of R2RLIS	20
2.3.5 Tunability of the Mechanical and Optical Properties of the Fabricated Nanostructures	21
2.4 Conclusion	25
2.5 Experimental Section	26
2.5.1 Confinement layers for R2RLIS	26
2.5.2 Substrate Preparation	27
2.5.3 Fabrication of the metal/epoxy nanomolds used in R2RLIS	27
2.5.4 R2R set-up	29
2.5.5 Microscopic imaging	30

	Page
2.5.6	Nanomechanical characterization 30
2.5.7	Molecular dynamics simulations 33
2.5.8	Finite element analysis 35
2.5.9	Optical characterization 36
2.5.10	Finite-difference time domain (FDTD) simulations 36
3	SCALABLE FABRICATION OF FLEXIBLE METASURFACES USING LOW-COST LASER DIODE ENGRAVERS 38
3.1	Introduction 38
3.2	Results 39
3.3	Conclusion 42
4	3D-ARCHITECTED SOFT MACHINES WITH TOPOLOGICALLY ENCODED MOTION 43
4.1	Introduction 43
4.2	Mathematical description of Voronoi tessellations and Delaunay triangulations 44
4.3	Results 44
4.3.1	Design, Fabrication, and Actuation of ASMs 44
4.3.2	Programming Motion by Controlling Beam Orientation 47
4.3.3	Programming Motion by Tuning Beam Thickness 52
4.3.4	Topologically Encoding Motion by Locally Tuning Voronoi Cell Size . . 56
4.3.5	Modular Approach to Build ASMs 57
4.3.6	Highly Compressible and Stretchable Elastomeric ASMs 58
4.4	Conclusion 62
4.5	Experimental Section 63
4.5.1	Rapid design of ASMs using Voronoi tessellation 63
4.5.2	3D printing ASMs 64
4.5.3	Fabrication of elastomeric ASMs by injection molding 64
4.5.4	Actuation and control 65
4.5.5	Mechanical characterization 66
4.5.6	Finite element simulations 66
5	MECHANICAL METAMATERIALS WITH PROGRAMMABLE COMPRESSION-TWIST COUPLING 67
5.1	Introduction 67
5.2	Results 67
5.2.1	Design, Fabrication, and Characterization of TMMs 67
5.2.2	Rotation Regimes in TMMs 74
5.2.3	Compression-Twist Coupling Optimization 82
5.2.4	Size-effect Independence of the Compression-Twist Coupling in TMMs 85
5.2.5	Programmable Auxetic Behavior of TMMs 87
5.2.6	Non-reciprocity and Path-dependence in TMMs 92
5.3	Conclusion 94
5.4	Experimental Section 95
5.4.1	Rational, automated design of TMMs 95
5.4.2	Finite element simulations 96

	Page
5.4.3 Fabrication of TMMs	97
5.4.4 Mechanical characterization of TMMs	97
6 OUTLOOK	99
A MATLAB CODES	101
B SUPPLEMENTARY MOVIES	106
REFERENCES	107
VITA	120
PUBLICATIONS	121

LIST OF FIGURES

Figure	Page
2.1 R2RLIS set-up and capabilities.	10
2.2 Schematic diagram summarizing the steps followed to load the feed roll into the custom-made R2R system.	11
2.3 Schematic diagram of the nanoforming process in R2RLIS.	12
2.4 Transmission spectra of commonly used laser windows.	12
2.5 Demonstration of the transparency of ZnSe and CaF ₂ windows to continuous CO ₂ laser beams.	13
2.6 Images of the Ti/epoxy nanomolds after being used to create nanostructures 75 times using R2RLIS.	14
2.7 Operating regimes of conventional CO ₂ laser systems for 5- μ m-thick Au films.	16
2.8 Ultrasmooth, 3D nanostructures fabricated by R2RLIS.	17
2.9 Discrete 3D Ag nanopillars.	18
2.10 Multi-scale simulations describing the mechanisms of R2RLIS.	21
2.11 Atomic snapshots from molecular dynamics (MD) simulations.	22
2.12 Strain hardening and grain refinement of the nanostructures fabricated by R2RLIS.	23
2.13 Force (F)-indentation depth (h) curves before and after R2RLIS.	24
2.14 Controlling the aspect ratio and the optical properties of the fabricated nanostructures by tuning the laser power applied during R2RLIS.	25
2.15 Determination of AFM cantilever sensitivity for nanomechanical characterization.	31
2.16 Nanomechanical characterization using AFM nanoindentation.	32
2.17 MD simulation domain.	34
2.18 Schematics of the FDTD simulation domain used to model gold nanogratings.	37
3.1 Schematic diagram of the electronic circuit used to pulse a 450 nm diode laser.	39
3.2 Ultrasmooth, 3D Au nanostructures fabricated by diode-laser-induced superplasticity.	40

Figure	Page
3.3 Grain refinement due to diode-laser-induced superplasticity.	41
3.4 Modulating aspect ratio, hardness, and reflectance of Au nanogratings by tuning the power of the diode laser.	41
4.1 Design, fabrication, and actuation of ASMs.	45
4.2 ASM gripper fabricated by 3D printing.	46
4.3 Programming motion of auxetic ASMs by controlling beam orientation.	48
4.4 Initial vertices, Delaunay triangulation, and Voronoi tessellation.	49
4.5 Comparison between the compressive nominal stress-strain characteristics of a solid cylinder and that of an ASM.	50
4.6 Pure compression ASM fabricated by 3D printing.	50
4.7 Design principle for twisting ASMs.	51
4.8 Bidirectional twisting ASM fabricated by 3D printing.	51
4.9 Programming motion of ASMs by tuning beam thickness.	53
4.10 Simulated bending angle of the cyclic bending ASM.	54
4.11 Programming motion in ASMs by locally tuning Voronoi cell size.	55
4.12 ASM hand fabricated by 3D printing.	56
4.13 Modular design of ASMs—example of a quadruped.	58
4.14 ASM quadruped fabricated by 3D printing.	59
4.15 Kinematic analysis of a crawling ASM quadruped.	60
4.16 Highly deformable elastomeric ASMs with embedded electronics.	61
4.17 Mechanical characterization of flexible photopolymers used to 3D print ASMs.	65
5.1 Design, fabrication, and characterization of TMMs.	68
5.2 Illustration of TMM design parameters n (number of levels) and m (number of Voronoi cells on each level).	69
5.3 Selected TMM CAD models for $n = 1$: $\alpha_d \in \{0, 30, 60, 90, 120\}$ mm, $\varphi \in \{0, 4, 8, 12, 16, 20\}^\circ$	70
5.4 Selected TMM CAD models for $n = 2$: $\alpha_d \in \{0, 30, 60, 90, 120\}$ mm, $\varphi \in \{0, 4, 8, 12, 16, 20\}^\circ$	71
5.5 Selected TMM CAD models for $n = 3$: $\alpha_d \in \{0, 30, 60, 90, 120\}$ mm, $\varphi \in \{0, 4, 8, 12, 16, 20\}^\circ$	72
5.6 Selected TMM CAD models for $n = 4$: $\alpha_d \in \{0, 30, 60, 90, 120\}$ mm, $\varphi \in \{0, 4, 8, 12, 16, 20\}^\circ$	73

Figure	Page	
5.7	Illustration of the frustum apex semi-angle φ , and the 3D curve angle α . For multi-level TMMs ($n > 1$), α at each level is slightly different.	74
5.8	Dependence of the 3D curve angle α on the planar curve angle α_{2D} for φ ranging 0–20°. For multi-level TMMs ($n > 1$), $\alpha_{avg} = \frac{1}{n} \sum_{i=1}^n \alpha_i$	74
5.9	Setups for FEA simulation and experimental characterization.	75
5.10	Comparison between TMMs fabricated out of different flexible materials.	76
5.11	Rotation regimes in TMMs.	77
5.12	Illustration of the critical strain $\varepsilon_{\theta_{max}}$ at which the direction of rotation reverses for bidirectional TMMs, and the effective rotation angle (θ_{eff}) used to quantify the uni- or bidirectionality of TMMs.	78
5.13	Illustration of the critical buckling strain ε_b , beyond which a snap-through instability is triggered.	79
5.14	θ - ε , F - ε , and weight-normalized F - ε curves for families of TMMs with $n = 2$, $\alpha_d = 0$ –130 mm, and $\varphi = 0^\circ$; $\varphi = 8^\circ$; and $\varphi = 14^\circ$	79
5.15	Chirality in TMMs.	80
5.16	Force analysis heatmaps for $n = 1$ –4.	81
5.17	Contour plots of the maximum reaction force (F_{max}), the weight of the TMM, and the weight-normalized maximum reaction force ($F_{max}/wt.$), for $n = 2$, φ ranging 0–20°, and α_d ranging 0–500 mm.	82
5.18	Compression-twist coupling optimization strategy and size effects for TMMs.	83
5.19	Exact locus and its zeroth order approximation of $\theta_{final,max} \varphi$ from Figure 5.18.	84
5.20	Contour plot of $d\theta/d\varepsilon$ as $\varepsilon \rightarrow 0$ for $n = 2$, φ ranging 0–20°, and α_d ranging 40–500 mm. $\alpha_d = 180$ mm is a zeroth-order approximation of the locus of $d\theta/d\varepsilon_{max} \varphi$	84
5.21	Contour plots of θ , $d\theta/d\varepsilon$, and $d^2\theta/d\varepsilon^2$ at $\varepsilon = 0.075$ for $n = 2$, φ ranging 0–20°, and α_d ranging 40–500 mm. $\alpha_d = 180$ mm (gray dotted vertical line) is a zeroth-order approximation of the locus of $\theta_{max} \varphi$	85
5.22	Dependence of the twisting angle θ , instantaneous twist per unit strain $d\theta/d\varepsilon$, normalized instantaneous angular acceleration $d^2\theta/d\varepsilon^2$ on the nominal strain ε for bidirectional TMMs with $n = 2$, $\alpha_d = 30$ mm, and φ ranging 0–20°.	85
5.23	Heatmap of the effective twisting angle θ_{eff} for $n = 1$, $n = 2$, $n = 3$, and $n = 4$; φ ranging 0–20° and α_d ranging 0–130 mm. Shades of blue ($\theta_{eff} > 0$) indicate unidirectional twisting, while shades of red ($\theta_{eff} < 0$) denote bidirectional twisting.	86
5.24	Programmable auxetic behavior of TMMs.	88
5.25	Spatiotemporal evolution of Poisson’s ratio of TMMs with $n = 2$, as a function of α_d (horizontal axes; ranging 0–500 mm) and φ (vertical axes; ranging 0–20°).	89

Figure	Page
5.26	Locations of occurrence of ν_{max} and ν_{min} 90
5.27	Variation of the local displacement and local strain at the deformation-tracking sections S_1 – S_9 as a function of the applied strain. 90
5.28	Evolution of the nominal Poisson’s ratio as a function of the applied strain at the nine deformation-tracking sections for TMMs with $\nu < 0$, $\nu > 0$, and ν close to 0 at all S_i ($i = 1, 2, \dots, 9$) and ε 91
5.29	Contour plots showing the regions on the α_d – φ landscape where (a) ν always > 0 (colored solid blue) for all ε at every S_i ($i = 1, 2, \dots, 9$); (b) ν always < 0 (colored solid red) for all ε at every S_i ($i = 1, 2, \dots, 9$). 92
5.30	Non-reciprocity and path-dependence in bidirectional TMMs. 93
5.31	Experimental stress-strain curves from uniaxial tensile testing of dogbone samples and Ogden model fit of the two photopolymers, FLGR02 and ELCL01, used to 3D print TMMs. 97

ABSTRACT

Goswami, Debkalpa Ph.D., Purdue University, August 2020. Design and Manufacturing of Flexible Optical and Mechanical Metamaterials. Major Professor: Ramses V. Martinez.

Metamaterials are artificially structured materials which attain their unconventional macroscopic properties from their cellular configuration rather than their constituent chemical composition. The judicious design of this cellular structure opens the possibility to program and control the optical, mechanical, acoustic, or thermal responses of metamaterials. This Ph.D. dissertation focuses on scalable design and manufacturing strategies for optical and mechanical metamaterials.

The fabrication of optical metamaterials still relies heavily on low-throughput process such as electron beam lithography, which is a serial technique. Thus, there is a growing need for the development of high-throughput, parallel processes to make the fabrication of optical metamaterials more accessible and cost-effective. The first part of this dissertation presents a scalable manufacturing method, termed “roll-to-roll laser induced superplasticity” (R2RLIS), for the production of flexible optical metamaterials, specifically metallic near-perfect absorbers. R2RLIS enables the rapid and inexpensive fabrication of ultra-smooth metallic nanostructures over large areas using conventional CO₂ engravers or inexpensive diode lasers. Using low-cost metal/epoxy nanomolds, the minimum feature size obtained by R2RLIS was <40 nm, facilitating the rapid fabrication of flexible near-perfect absorbers at visible frequencies with the capability to wrap around non-planar surfaces.

The existing approaches for designing mechanical metamaterials are mostly ad hoc, and rely heavily on intuition and trial-and-error. A rational and systematic approach to create functional and programmable mechanical metamaterials is therefore desirable to unlock the vast design space of mechanical properties. The second part of this dissertation introduces a systematic, algorithmic design strategy based on Voronoi tessellation to create

architected soft machines (ASMs) and twisting mechanical metamaterials (TMMs) with programmable motion and properties. ASMs are a new class of soft machines that benefit from their 3D-architected structure to expand the range of mechanical properties and behaviors achievable by 3D printed soft robots. On tendon-based actuation, ASMs deform according to the topologically encoded buckling of their structure to produce a wide range of motions such as contraction, twisting, bending, and cyclic motion. TMMs are a new class of chiral mechanical metamaterials which exhibit compression-twist coupling, a property absent in isotropic materials. This property manifests macroscopically and is independent of the flexible material chosen to fabricate the TMM. The nature of this compression-twist coupling can be programmed by simply tuning two design parameters, giving access to distinct twisting regimes and tunable onset of auxetic (negative Poisson's ratio) behavior. Taking a metamaterial approach toward the design of soft machines substantially increases their number of degrees of freedom in deformation, thus blurring the boundary between materials and machines.

CHAPTER 1. INTRODUCTION

Metamaterials are artificially structured materials which attain their unconventional macroscopic properties from their cellular structure rather than their constituent materials. The judicious design of this cellular structure opens the possibility to program and control the optical,¹ mechanical,² acoustic,³ or thermal⁴ responses of metamaterials. My Ph.D. thesis focuses on scalable design and manufacturing strategies for optical and mechanical metamaterials.

1.1 Motivation

Optical metamaterials exhibit unusual and exciting responses such as anomalous reflection⁵ or refraction,⁶ perfect absorption,⁷ and sub-wavelength focusing⁸ to incident electromagnetic radiation. While these properties may be predicted theoretically using Maxwell's equations, optical metamaterials have only flourished in the present century thanks to combined advances in nanofabrication techniques, numerical modeling, and characterization tools.⁹ The fabrication of optical metamaterials, however, still relies heavily on low-throughput process such as electron beam lithography, which is a serial technique. Thus, there is a growing need for the development of high-throughput, parallel processes to make the fabrication of optical metamaterials more accessible and cost-effective.

Mechanical metamaterials, similarly, exhibit mechanical properties and functionalities that differ from and surpass those of their constituent bulk materials rather than simply combining them. In addition to achieving unusual (negative or zero) values of familiar mechanical parameters such as Poisson's ratio, density, and compressibility, emerging classes of mechanical metamaterials demonstrate exotic functionalities such as shape-morphing or topological protection.¹⁰ The approaches for designing mechanical metamaterials, however,

are mostly *ad hoc*, and rely heavily on intuition and trial-and-error. A rational and systematic approach to create functional and programmable mechanical metamaterials is therefore desirable to unlock the vast design space of mechanical properties.

My Ph.D. thesis consists of two parts: the first part presents a scalable manufacturing method for the production of flexible optical metamaterials, specifically metallic near-perfect absorbers. The second part introduces a systematic design strategy based on the Voronoi tessellation algorithm to create soft robotic structures with programmable mechanical metamaterial properties.

1.2 Background and Literature Review

1.2.1 Challenges in Scalable Fabrication of Metallic Nanostructures

Exploiting the potential applications of metallic nanostructures in a variety of fields such as plasmonics,¹¹⁻¹⁴ electronics,¹⁵ and biosciences¹⁶⁻¹⁸ requires the large-scale manufacture of such structures with high quality and nanoscale resolution. Although many nanopatterning processes enable the cost-effective fabrication of metallic nanostructures over large areas, the required post-patterning steps (such as metallization and lift-off) increase the cost, complexity, and processing time of these techniques, reducing their throughput. Additionally, post-patterning processes generally affect the crystallinity, sharp corners, and homogeneity of the lateral walls of the final nanostructures.^{19,20} The development of a high-throughput manufacturing method capable of producing ultrasMOOTH crystalline metallic nanostructures at ambient conditions using a roll-to-roll approach still remains a challenge.

1.2.2 Soft-Lithographic and Imprint-based Nanopatterning Techniques

Several patterning techniques have been developed to enable nanofabrication over large areas in a relatively rapid and low-cost fashion using nanostamps.²¹⁻²⁴ Soft elastomeric nanostamps, most notably made of polydimethylsiloxane (PDMS), have been used to replicate nanoscale features in a variety of low cost and highly parallel “soft lithographic” processes, enabling sub-100 nm resolution patterning over curved surfaces and large areas.²⁵ The

low Young's modulus of the PDMS stamps, however, makes it difficult to replicate < 100 nm patterns as well as high aspect ratio (> 2) nanostructures due to the self-adhesion of the features of the stamps as a consequence of electrostatic attraction, mechanical stress, or capillary forces.²⁶ After patterning, typical soft lithography processes—such as microcontact printing, solvent-assisted micromolding, replica molding, and nanotransfer printing—often require additional time-consuming etching or metallization steps to fabricate metallic nanostructures.²⁷ Nanoimprint lithography (NIL)²⁸ and step-and-flash imprint lithography (SFIL)²⁹ circumvent the resolution limits of soft lithographic techniques by using hard stamps to pattern photoresists with sub-50 nm accuracy. Additionally, nanoimprint lithography has demonstrated the continuous production of polymeric nanopatterns over large areas using a roll-to-roll system (R2RNIL).^{24,30} Although R2RNIL is scalable, the required etching of the residual polymer layer, and the subsequent metal deposition and lift-off steps needed to generate the final metallic arrays add complexity to the process and reduce the throughput of this nanomanufacturing technique.

1.2.3 Lasers as Micro- and Nanofabrication Tools

Lasers are extensively used as processing and manufacturing tools due to their unique advantage of being a non-contact process with flexible setups that can operate in air, vacuum, or liquid environments.³¹ Lasers offer many attractive possibilities as a micro- and nanofabrication tool since their intense radiation can be easily focused down to the micrometer scale and can cause the melting and ablation of a large variety of materials, enabling their drilling,^{32–34} cutting,^{35,36} welding,^{37,38} annealing,^{39,40} and surface modification.^{41–43} Laser interference lithography (LIL) has proved to be a versatile technique to cure large areas coated with photoresist so that, after developing, metallization, and lift-off, uniform arrays of metallic nanostructures (typically lines and dots) can be fabricated.^{44–46} The generation of internal reflections in the photoresist layer limits the resolution of LIL, requiring the deposition of an anti-reflection coating layer between the substrate and the photoresist, adding further complexity to a process that often requires cumbersome laser systems, cleanroom facilities, and special vibration isolation to operate. Purdue researchers recently demonstrated Laser Shock Imprinting (LSI), a cost-effective nanopatterning method for the fabrication of

smooth metallic nanostructures at ambient conditions.⁴⁷ LSI uses ultra-short laser pulses to compress metallic sheets into silicon nanomolds, generating metallic nanopatterns over large areas. Unfortunately, LSI has only been demonstrated, with nanoscale resolution, using costly nanomolds and high-energy nanosecond laser systems that are expensive and not as vastly used as CO₂ lasers for manufacturing and rapid prototyping.^{47,48}

1.2.4 Soft Machines and Current Design Challenges

Soft machines with continuously deformable bodies are advantageous for safe physical human-robot interactions⁴⁹ and the manipulation of delicate objects,⁵⁰ as well as for withstanding large impact forces⁵¹ and achieving multiple locomotion gaits—such as crawling,⁵² undulation,⁵³ hopping,⁵⁴ rolling,⁵⁵ or growing⁵⁶—to adapt to their environment. Despite their advantages in safety, adaptability, and maneuverability, soft robots suffer from the lack of rigorous engineering methods since traditional rigid-body mechanics cannot adequately describe continuum soft robotic motion.⁵⁷ Heuristic and intuition-driven approaches typically used in the design and fabrication of soft robots⁵⁸ are further strained in the case of multi-functional soft robotic systems, which have only been able to demonstrate reconfigurability *via* the removal and re-addition of parts relative to each other.⁵⁹

1.2.5 Need for Architected, Mechanical Metamaterial-based Soft Robots

The structure—architectural design—of a material determines its mechanical properties and performance.^{60–62} In other words, it is possible to tune the mechanical response of a material by controlling its architecture. Mechanical metamaterials illustrate this close relationship between architecture and functionality by exhibiting unusual physical properties such as negative Poisson’s ratio,^{63–65} multistability,^{66,67} phase shifting,⁶⁸ or programmability.⁶⁹ The structure of most mechanical metamaterials previously reported consist of periodic arrays of unit cells, which lead to materials with uniform mechanical responses upon actuation. Latest advances in soft robotics, wearable devices, and prosthetics, however, require spatially distributed functionality, which can only be produced by complex aperiodic architectures that are difficult to design. Naïve implementations of complex aperiodic structures often lead to

geometrical frustration zones (areas of the material where local constraints cannot be satisfied), which impede the coherent operation of the material and prevent metamaterial-like functionality.⁷⁰ The lack of rational design algorithms capable of rapidly creating aperiodic, yet frustration free, architected materials exhibiting localized actuation has hindered the development of soft machines that benefit from metamaterial behaviors.

1.2.6 Exploiting Mechanical Instabilities for Soft Robotic Actuation

Harnessing mechanical instabilities—considered signs of structural failure in hard actuators—has recently emerged as a robust strategy to design and fabricate functional soft actuators with highly controllable nonlinear behavior.^{71,72} The reversible buckling of elastomeric beams is an example of a mechanical instability that can be harnessed to enable applications in stretchable electronics,^{73,74} switchable metamaterials,⁶⁸ and soft fluidic actuators.^{75,76} Fluidic, buckling-based soft actuators typically consist of an elastomeric slab patterned with two-dimensional periodic arrays of holes perpendicular to the slab sealed by elastomeric membranes.^{75,76} Upon applying negative pressure (vacuum), the buckling of the internal cavities of the soft actuator produces a regular and reversible deformation capable of generating linear⁷⁵ and rotational motion.⁷⁷ Fluidic actuators can achieve motions with faster response times than actuators made of electroactive polymers⁵⁸ and larger amplitudes than dielectric elastomers^{78,79} and ionic conducting polymer films.⁸⁰ The variety of motions achievable by fluidic actuators is, however, limited by the need of bulky pneumatic or hydraulic sources, and the difficulty to design and manufacture soft actuators with tailored three-dimensional (3D) architectures.

1.2.7 Magnetic and Tendon-based Actuation Mechanisms

Recently, small soft robots with embedded magnetic microparticles demonstrated fast and untethered actuation using rotating and alternating magnetic fields.^{69,81} Unfortunately, the scalability of this actuation mechanism is limited by the difficulty to enlarge the area where the magnetic fields can be tuned, since the actuating electromagnets must be at least as large as the desired field of motion of the robots.⁸¹ Motor-tendon actuation approaches

in soft robotics have also demonstrated fast actuation using relatively small and inexpensive motors.⁸² Due to their small size, tendons can be attached at multiple locations within a soft robot—even in places where it would be difficult to house other actuators otherwise—providing distributed and continuum actuation. Additionally, tendons offer a lightweight, low inertia platform for long-range force transmission with negligible backlash.⁸³ The friction between the tendons and the soft body of the robot, however, introduces nonlinearities that reduce the controllability of the system.

1.2.8 Approaches to Manufacture Soft Robots and Mechanical Metamaterials

Several manufacturing strategies have been proposed for the design and assembly of 3D soft actuators and metamaterials, including casting using custom-designed molds,^{50,52,65} lithographic etching of silicones,⁸⁴ lost-wax approaches,⁸⁵ and inducing porosity in elastomeric composites.⁸⁶ Recent advances in the direct writing of elastomeric inks^{66,87} and other 3D⁸⁸ and 4D⁸⁹ additive manufacturing processes have expanded the number of flexible and stretchable polymers that can be printed and actuated with a high degree of control.^{90,91} In particular, 3D printing has enabled the fabrication of architected foams and mechanical metamaterials that bend along preferential directions to control the distribution of compressive forces or their deformation upon human interaction.^{60–62} The dense spatial distribution of beams in the volume of these structures, however, complicates their interfacing with actuation mechanisms, limiting their use in robotic applications.

1.2.9 Achieving Compression-Twist Coupling with Mechanical Metamaterials

The *in situ* conversion of a linear motion into rotation is an advantageous property ubiquitous in multi-component mechanisms and machines, yet unavailable in monolithic isotropic materials due to the invariance of the Cauchy elasticity tensor under space inversion.⁹² In a seminal 2017 work, Frenzel et al.⁹³ were the first to illustrate, using periodic arrays of tetrachiral unit cells, a microstructured 3D mechanical metamaterial which twists upon compression. These structures, however, could not sustain significant strains ($> 1.5\%$) or twist beyond 3° owing to mechanical frustration. More importantly, the chiral response

of these metamaterials was strongly size-dependent: the magnitude of the twist decayed as the system size increased. Although multiple researchers have since reported structures with compression/extension-twist coupling exhibiting larger absolute twists and a range of Poisson’s ratios,^{94–101} these designs still suffer from size effects, which compromise their scalability. Moreover, the design processes for these metamaterials are *ad hoc*, and simultaneous control of twisting and Poisson’s ratio remain a challenge.

1.3 Organization of this thesis

This introductory chapter outlined the primary motivations for undertaking the research projects detailed in the rest of this thesis, in light of the existing state of the art.

Chapters 2 and 3 deal with the fabrication of optical metamaterials. In Chapter 2, I describe a high-throughput and scalable nanomanufacturing process—roll-to-roll laser induced superplasticity (R2RLIS)—to create large arrays of robust, metallic optical metamaterials supported on flexible substrates. In Chapter 3, I propose a “bare-bones” ultra-low-cost version of R2RLIS, which uses a \sim \$200 diode laser to directly pattern thin metal foils.

Chapters 4 and 5 discuss automated design strategies of mechanical metamaterials for soft robotics. In Chapter 4, I introduce Voronoi tessellation as an accessible method to create 3D-printable soft actuators with metamaterial properties from any 3D CAD model. Chapter 5 describes mechanical-frustration-free twisting mechanical metamaterials designed using a generative parametric algorithm and exhibiting programmable properties.

Finally in Chapter 6, I unify and link the similar underlying principles governing both optical and mechanical metamaterial design.

CHAPTER 2. ROLL-TO-ROLL NANOFORMING OF METALS USING LASER-INDUCED SUPERPLASTICITY

Reproduced in part with permission from Ref.¹⁰² Copyright 2018 American Chemical Society.

2.1 Introduction

This chapter presents R2RLIS, a roll-to-roll laser-induced superplasticity method capable of fabricating ultra-smooth metallic nanostructures on a variety of polymeric substrates using a CO₂ laser as the radiation source. The relatively low acquisition price of CO₂ laser engravers compared to nanosecond pulsed-laser systems facilitates the adoption of R2RLIS for nanofabrication, particularly in academic research or resource-limited industrial settings. The basic principle of this roll-to-roll nanofabrication method is the induction of a high-strain-rate superplastic behavior into metallic films using shock waves generated by the laser ablation of graphite, enabling the cold nanofforming of metals using a low-cost, polymeric nanomold. R2RLIS is scalable, inexpensive, and can be easily implemented in conventional CO₂ laser cutters and engravers, improving their functionality, so they can also be used for fabricating metallic nanostructures and welding them to polymeric substrates to facilitate their manipulation. Moreover, the capability to control the hardness and the aspect ratio of the fabricated nanostructures by tuning the intensity of the laser makes R2RLIS an attractive high-throughput nanomanufacturing technique for the development of flexible plasmonic devices.

2.2 Rationale for the use of CO₂ lasers in nanomanufacturing

The carbon dioxide (CO₂) laser was invented in 1964 and is still among the highest power continuous wave lasers currently available.¹⁰³ CO₂ lasers, due to their reasonable

cost, high efficiency (20%), and reliability, are frequently used in industrial applications for cutting,^{104,105} welding,^{106,107} or engraving.¹⁰⁸ CO₂ lasers have also found a place in many microfluidics, micro-electromechanical, and optofluidics laboratories as a rapid prototyping tool since they are useful for engraving and cutting micro-channels in a variety of polymers.^{109–111} Using laser annealing and ablation-induced methods, CO₂ lasers have been employed in the past to fabricate random distributions of nanoparticles and nanopores.^{112,113} Nanofluidic channels and smooth nanostructures on SiO₂ were previously reported using a CO₂ laser as a melting tool that improves the lateral walls of the nanostructures or sealed SiO₂ nanotrenches fabricated using electron beam lithography (EBL) or focused ion beam (FIB). Unfortunately, due to the relatively large wavelength of CO₂ lasers ($\lambda = 10.6 \mu\text{m}$), the use of these lasers for the fabrication of periodic arrays of smooth metallic nanostructures over large areas remains a challenge. R2RLIS enables, for the first time, the fabrication of ultrasmooth metallic nanostructures on a roll-to-roll basis using conventional CO₂ lasers, making the nanomanufacturing of plasmonic devices accessible to resource-limited academic and industrial settings.

2.3 Results

2.3.1 Pilot Line for Roll-to-Roll Nanofforming of Metals

Figure 2.1a shows the two laser-based fabrication steps in R2RLIS: nanofforming and welding to a flexible substrate. Briefly, during the nanofforming step, a set of rubber rolls introduce a metallic film, coated with graphite on one of its sides, under a confinement layer (Figure 2.2). This confinement layer, controlled by a linear actuator, presses the metallic film against a tensioned belt carrying a metal/epoxy nanomold using a metal plate as a back support. We used a conventional CO₂ laser (60 W, $\lambda = 10.6 \mu\text{m}$, continuous wave) to ablate a $\sim 5\text{-}\mu\text{m}$ -thick graphite layer sprayed on the back of the metallic film (5–8 μm -thick). The shock wave generated by the ablation of the graphite layer and confined by a ZnSe or CaF₂ window induces the superplastic flow of the metal into the nanoscale features of the underlying nanomold (Figure 2.3). The peak pressure of the shock wave generated by the CO₂ laser depends on the power density used to ablate the graphite layer, reaching up to

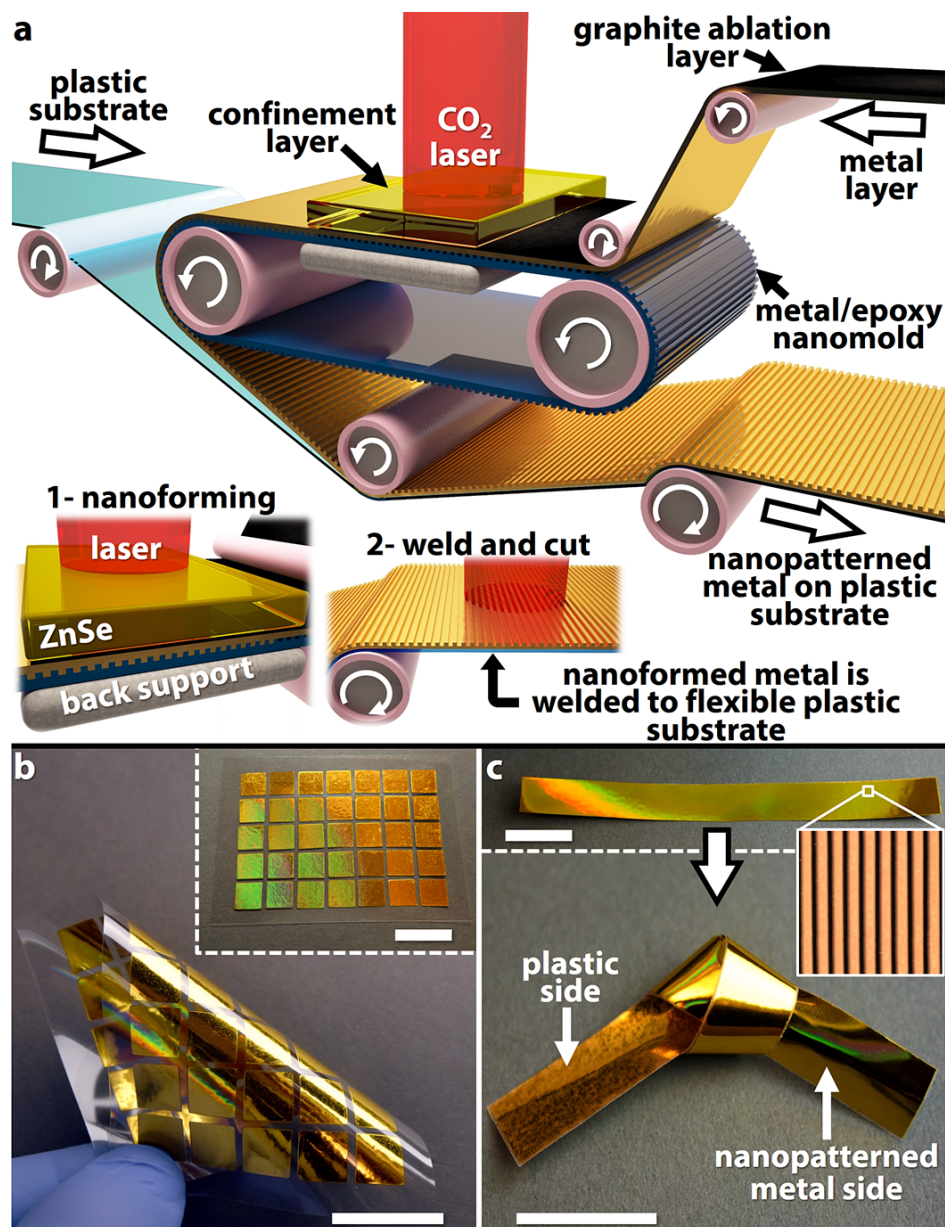


Figure 2.1. R2RLIS set-up and capabilities. (a) Schematic diagram of the pilot line for the roll-to-roll nanoforming of metals. 1) During the nanoforming of the metal film, an IR window (ZnSe) is used as a confinement layer, so that the expansion of the ablated graphite layer induces the superplastic deformation of the metal film into the nanomold upon laser irradiation. 2) After the nanopatterned metal is brought to contact with the supporting plastic film, a second laser scan welds the metal to the plastic substrate. (b) 5×7 array of 1 cm^2 nanoformed Au domains welded to a flexible PET substrate. (c) Nanopatterned Au/PET composite with enough flexibility and interfacial adhesion to withstand bending and being tied into a knot. Inset shows a high-resolution AFM image of the ultrasmooth Au nanogratings (350 nm linewidth). All scale bars are 2 cm.

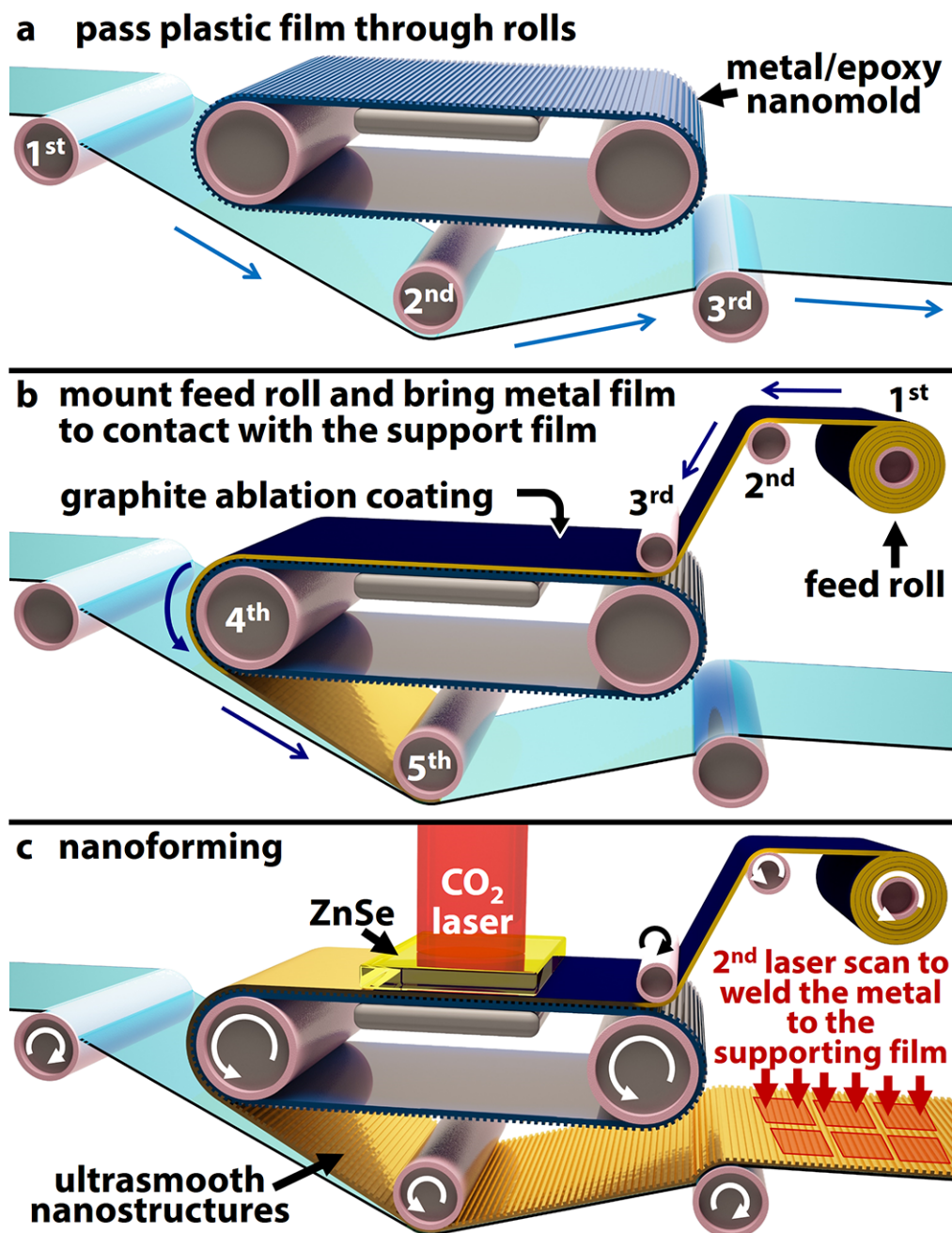


Figure 2.2. Schematic diagram summarizing the steps followed to load the feed roll into the custom-made R2R system. (a) The plastic support is fed from the left and passed through the rolls at the bottom of the R2R system (in the direction of the arrows, according to the order described in the figure). (b) The feed roll is added to the R2R system, placed over the metal/epoxy nanomold and brought into contact with the support film (following the direction of the arrows, in the order described). (c) An IR window (ZnSe) is used as a confinement layer, so that the expansion of the ablated graphite layer induces the superplastic deformation of the metal film into the nanomold upon laser irradiation.

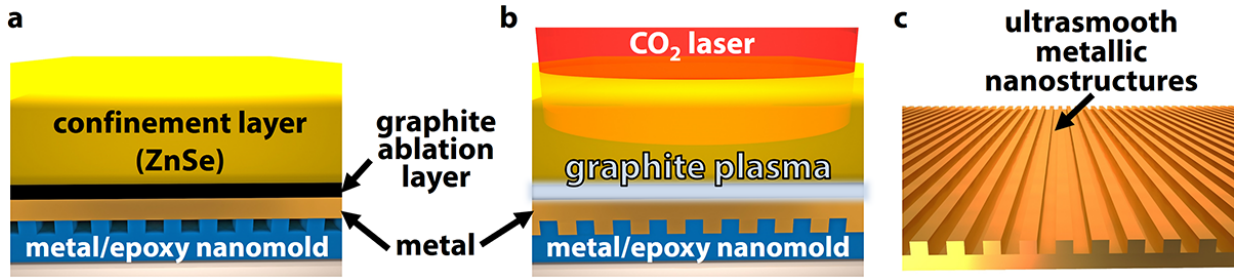


Figure 2.3. Schematic diagram of the nanoforming process in R2RLIS. (a) A free-standing metal film is spray-coated on one side with a $\sim 5\text{-}\mu\text{m}$ -thick layer of graphite and placed on top of an epoxy nanomold metallized with 50 nm of titanium. A ZnSe window is used to confine the shockwave produced by the laser ablation of the graphite layer. (b) A CO_2 laser beam locally ablates the graphite, generating a shockwave which induces the superplastic flow of the metal film into the nanomold. (c) Ultrasmooth crystalline metallic nanostructures are obtained after demolding the metal film from the nanomold. No lubricating layer is necessary to perform R2RLIS.

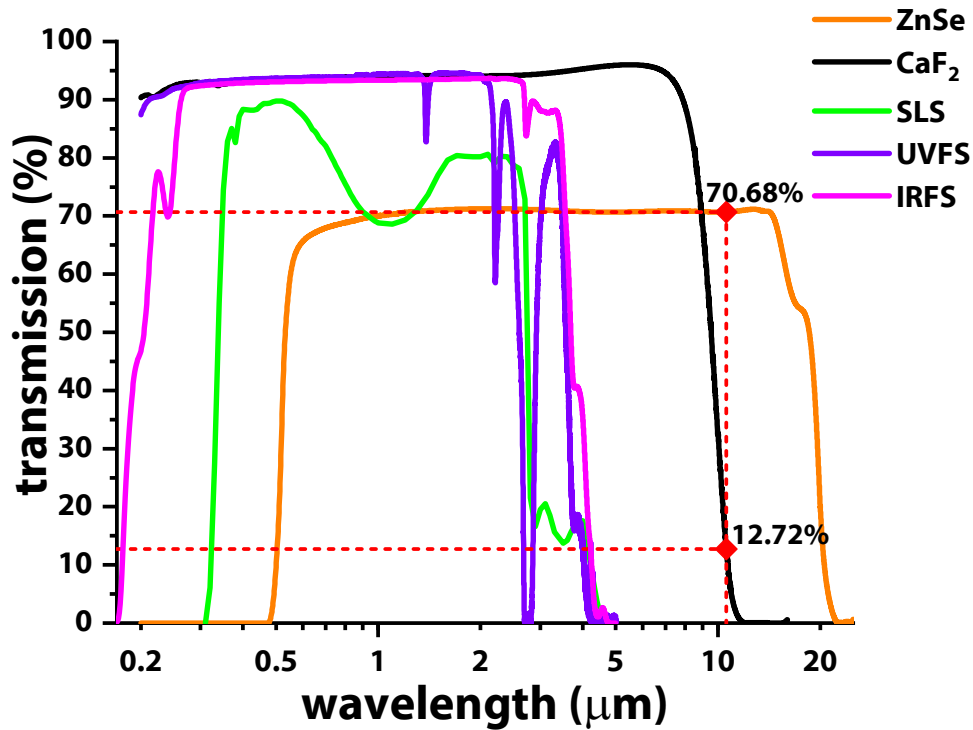


Figure 2.4. Transmission spectra of commonly used laser windows: zinc selenide (ZnSe), calcium fluoride (CaF_2), soda-lime silica (SLS), UV fused silica (UVFS) and IR fused silica (IRFS). The wavelength axis is plotted on a logarithmic scale. Only ZnSe and CaF_2 transmit at the operating wavelength of CO_2 lasers ($\lambda = 10.6\ \mu\text{m}$).



Figure 2.5. Demonstration of the transparency of ZnSe and CaF₂ windows to continuous CO₂ laser beams. These windows are used as confinement layers in R2RLIS. (a) The window is first placed on a sheet of paper with an inkjet-printed “P”. (b) A CO₂ laser beam is used to write the letters “urdue” through the window. (c) The window is then placed on another sheet of paper, showing no observable damage. The windows were also inspected at the microscopic level to verify that the lasing action did not cause any superficial damage or internal crack to the confinement layer.

1.5 GPa (at 5 MW/cm²), according to the Fabbro’s model.¹¹⁴ The propagation of the shock wave along the metallic film induces superplastic strain rates (10⁶–10⁷ s⁻¹),^{115,116} facilitating the conforming of the metal to the nanomold. The low absorbance of ZnSe and CaF₂ at $\lambda = 10.6 \mu\text{m}$ (Figure 2.4) prevents the confinement layer from damage by the laser pulses during the R2RLIS process, since the temperature of the graphite plasma is not sufficiently high to dry etch the confinement layer (Figure 2.5).

After the metal film is patterned with ultrasmooth nanostructures, a set of synchronized rubber rolls transfers it onto a thermo-adhesive plastic substrate (polyethylene terephthalate, PET). The localized heating of the polymer, once the CO₂ laser scans the final shape of the device ($\sim 1.6 \text{ J/mm}^2$), welds the patterned metal to the plastic. Figure 2.1b shows that metallic nanostructures welded to a flexible substrate are easy to manipulate and bend

(radius of curvature as low as 0.5 mm). The thin nanopatterned Au/PET composites fabricated by R2RLIS exhibit a robust interfacial contact and enough flexibility to be tied into a knot (Figure 2.1c).

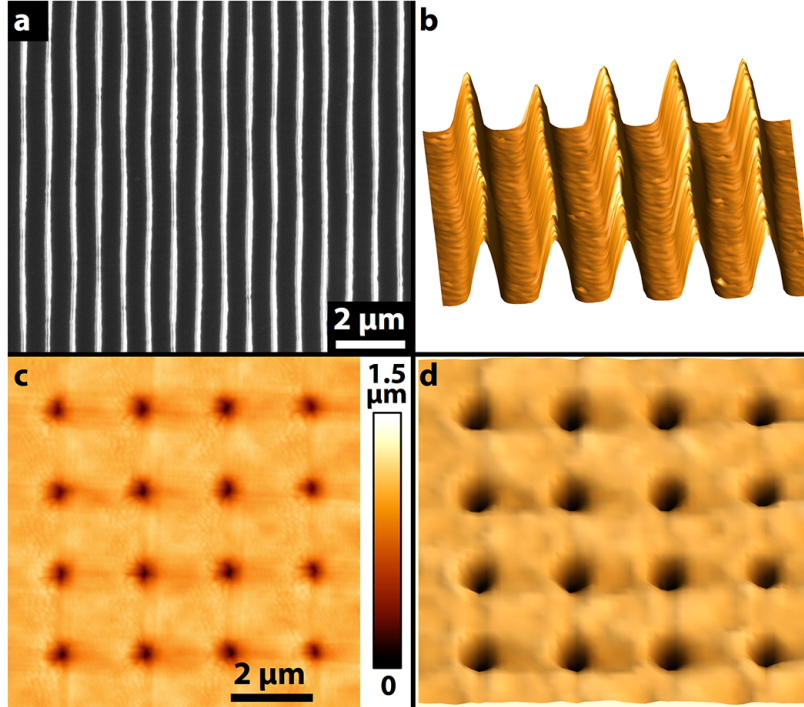


Figure 2.6. Images of the Ti/epoxy nanomolds after being used to create nanostructures 75 times using R2RLIS. (a) SEM image of the Ti/epoxy nanomold used to fabricate the Al nano V-grooves shown in Figure 2.8b. (b) 3D AFM image of the Ti/epoxy nanomold shown in (a). (c) High resolution AFM image of the Ti/epoxy nanomold used to fabricate the ultrasmooth 3D Ag nanopillars shown in Figure 2.8d and Figure 2.9. (d) 3D AFM image of the nanomold shown in (c).

Since nanomold cost is one of the main limitations of laser shock-based nanofabrication techniques,⁴⁷ we carried out R2RLIS using low-cost metal/epoxy nanomolds fabricated using soft lithographic tools.^{117,118} Briefly, we used silanized fused silica diffraction gratings and silicon nanomolds fabricated by electron beam lithography (EBL) and reactive ion etching (RIE) as masters for soft replica molding. We generated flexible h-PDMS/PDMS stamps from the masters and transferred the nanofeatures of the flexible stamps to a flexible PET film coated with a low-surface-energy epoxy. After UV-curing the epoxy through the h-PDMS/PDMS stamp, the epoxy replicas of the flexible stamp were metallized with a 50 nm thick layer of Ti and used as nanomolds for R2RLIS. We have used the h-PDMS/PDMS

stamps to fabricate epoxy nanomolds for this study more than 200 times with no apparent damage or degradation. The low laser power density used in R2RLIS enables the reusability of these low-cost nanomolds up to 90 times before the mechanical fatigue suffered by Ti/epoxy composite affects the quality of the nanostructures fabricated by R2RLIS (see Figure 2.6). Ti/epoxy nanomolds do not require any lubricant layer to work or to release the metal film after nanoforming.

2.3.2 Selective Nanoforming, Welding, and Cutting

R2RLIS makes it possible for conventional CO₂ lasers—typically used for cutting and welding—to perform roll-to-roll nanoforming processes, providing them with the functionality of patterning nanostructures on the surface of thin metallic films. Figure 2.7a shows the CO₂ laser power required to weld or cut 5- μm -thick Au films mounted on a PET substrate for different scanning speeds. We found that the laser dose necessary to weld and cut these Au/PET composites (not coated with an ablation layer) was 1.67 J/mm² and 3.33 J/mm², respectively (Figure 2.7b). Pressing the Au film with the confinement layer (~ 200 mbar), we found that the dose needed to induce superplastic flow to the film—coated with a ~ 5 - μm -thick graphite ablation layer—during the nanoforming process is 19.1 J/mm². Figure 2.7c shows the process followed to fabricate flexible plasmonic devices using R2RLIS. First, the Au film is nanoformed against a Ti/epoxy nanomold with a 375 nm linewidth and 120 nm height. After nanoforming the desired region of the metal film, consuming most of the graphite ablation coating on that area, the roll-to-roll system mounts the nanopatterned metal on the PET substrate. A second laser scan welds the nanoformed regions of the metal film to the underlying plastic substrate. Right after the welding scan, the CO₂ laser trims the final shape of the device according to the powers and scanning speeds described in Figure 2.7a. Finally, the robust interfacial contact between the substrate and the welded nanoformed region of the metal film allows for the removal of the unwelded regions of the device using conventional adhesive paper or tape.

Figure 2.8 shows several examples of ultrasmooth metallic nanostructures fabricated by R2RLIS on Au, Al, Cu, and Ag films. Figure 2.8a,b shows ultrasmooth gratings with square and triangular nanogrooves fabricated in Au and Al films. Nano V-grooves fabricated in Al

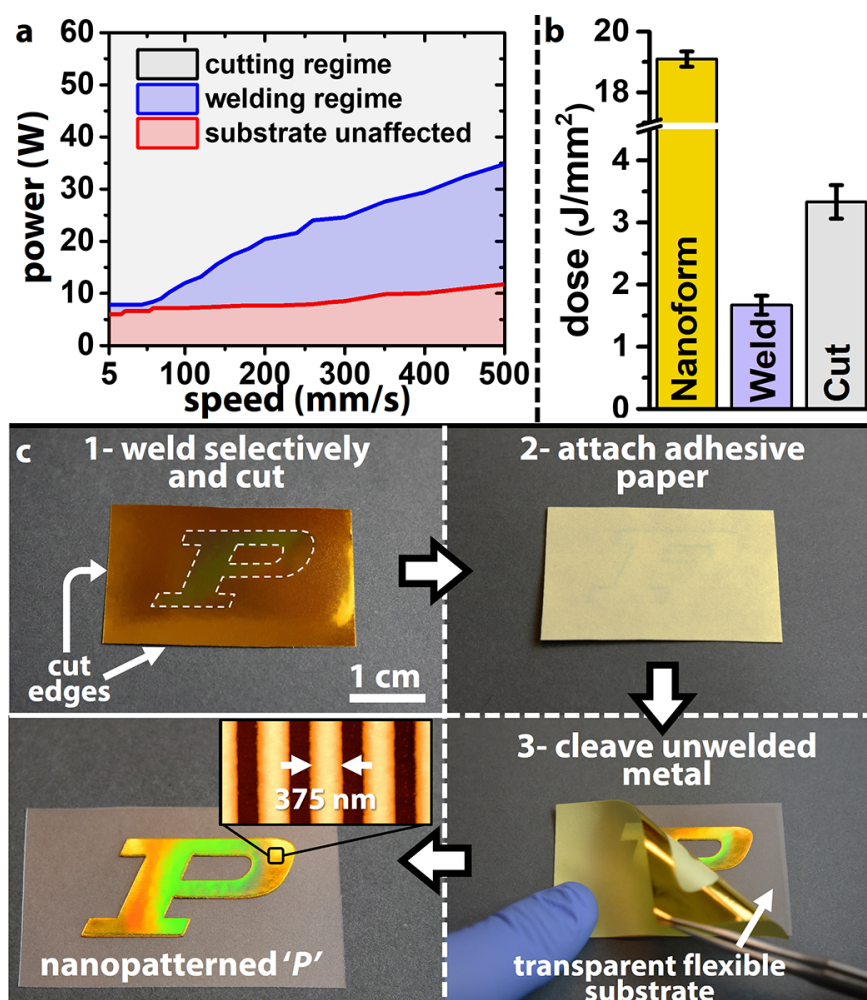


Figure 2.7. Operating regimes of conventional CO₂ laser systems for 5- μm -thick Au films. (a) Cutting and welding regimes for Au films not coated with an ablation layer. (b) Typical doses necessary for achieving nanoforming (using an ablation layer), welding, and cutting. (c) Fabrication of flexible plasmonic devices using R2RLIS: 1) After the nanoforming of the metal, the highlighted region of the film (dashed “P”) is welded to the flexible PET substrate, and the perimeter of the device is cut; 2) adhesive paper is attached to the Au/PET composite; 3) the removal of the adhesive paper cleaves the unwelded regions of the device, leaving the welded nanoformed region intact. Inset shows a high-resolution AFM image of the ultrasmooth Au nanograting.

using R2RLIS reached uniform aspect ratios of 5 (200 nm depth, 40 nm width) over large areas (Figure 2.8b). Similar nanogratings have been demonstrated to support the propagation of channel plasmon polaritons, which makes them attractive for photonic applications.¹¹⁹ R2RLIS also enables the possibility of creating nanoscale fishnet structures by nanoforming a metal film twice using the same square groove nanomold (Figure 2.8c). Once the nanograting

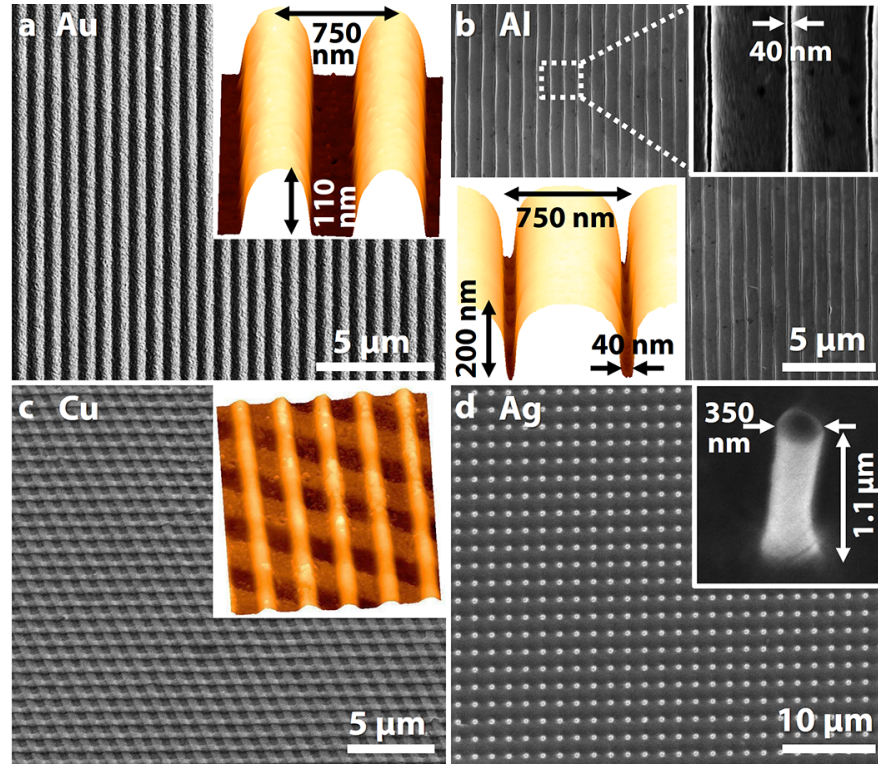


Figure 2.8. Ultrasmooth, 3D nanostructures fabricated by R2RLIS. (a) Au nanograting with a 350 nm linewidth and a 110 nm height. (b) Nano V-grooves with an aspect ratio of 5 (200 nm depth, 40 nm width) fabricated on Al. (c) Nanoscale fishnet fabricated on a Cu film. (d) Array of Ag nanopillars with a diameter of 350 nm and height 1.1 μm . SEM and AFM are used to visualize the nanostructures.

is formed on the surface of the metal film, after the first nanoforming process, the ablation coating is re-applied on the back of the film and a second nanoforming process is performed against the nanomold, perpendicularly oriented with respect to the first nanoforming process. To compensate for the strain hardening of the sample after the first nanoforming step (CO_2 laser power density of $2.12 \text{ MW}/\text{cm}^2$), a higher laser power density is applied ($4.05 \text{ MW}/\text{cm}^2$) to create a uniform nanoscale fishnet (Figure 2.8c). Such nanoscale fishnet designs have been proposed as left-handed metamaterials for high resolution focusing and invisibility cloaks.¹²⁰ Figure 2.8d and Figure 2.9 show that R2RLIS is also compatible with the fabrication of arrays of discrete 3D nanostructures such as cylindrical Ag nanopillars with ultrasmooth lateral surfaces and a diameter of 350 nm and height 1.1 μm (aspect ratio of ~ 3). The superplastic flow of the metal into the nanomold justifies its ultrasmooth lateral surface and the high-fidelity replication of the Ti/epoxy nanomolds (see nanomold in Figure 2.6).

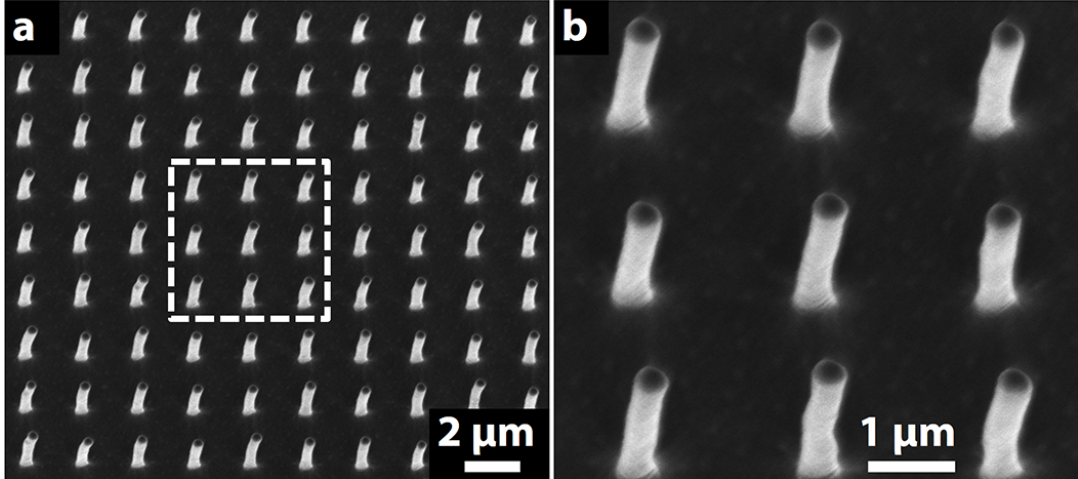


Figure 2.9. (a) SEM image showing an array of discrete 3D Ag nanopillars. (b) High resolution SEM image of the area marked in (a). These 3D nanopillars have a diameter of 350 nm and a height of 1.1 μm .

2.3.3 Conditions for Nanoforming, Welding, and Cutting using R2RLIS

We coupled a commercially available CO₂ laser engraver (MT3050D, MornTech Inc.; Stockton, CA) with a custom-built roll-to-roll system to perform R2RLIS. The maximum pulse energy is 60 mJ/pulse; the pulse width of the laser is 1 ms. We measured the laser pulse energy using an optical power meter (Newport, type: 1916c). The size of the beam at best focus is $\sim 40 \mu\text{m}$ and was measured using photosensitive paper (Kodak Linagraph, type: 1895). The extent of the nanoforming, welding, and cutting regimes were determined experimentally (Figure 2.7a). We calculated the optimal laser dose, D , in terms of the fluence (energy per unit area) of the CO₂ laser beam (Figure 2.7b). We used the following symbols and assumptions in our calculations:

P = maximum output power of the laser,

f_P = fraction of P used,

v = traverse speed of laser beam,

d = beam spot size,

f_T = fraction of incident energy transmitted by IR window,

τ = laser pulse duration

Assumptions:

1. The expressions for dose assume that the power of the beam is uniform over the spot size. Laser beams, however, are often Gaussian, in which case the effective power is approximately half of the peak power P ; i.e., a Gaussian distribution with peak power P can be replaced by a constant distribution of power $P/2$.
2. The rastering speed, v , of the laser beam is assumed to be constant. Experimentally, however, the mechanical constraints of our system decrease the rastering speed on every change of direction, not making the speed constant on the edges of the rastered area.

Cutting and welding

We considered a laser beam of spot size d focused on the substrate, and moving at a speed v mm/s relative to the substrate. In 1 s, the area irradiated by the beam is $v \times d$. During this 1 s, the energy supplied to the substrate is $f_P P$. Therefore,

$$D_{cut,weld} = \frac{f_P P}{vd},$$

showing that the locus of a point of constant dose in the v - P plane is a straight line. Our experimental measurements (Figure 2.7a), especially in the welding regime, deviate slightly from the predicted linear behavior, since the local welding phenomenon is dictated by the heat affected zone (HAZ) rather than the area of irradiation, and the HAZ is an ill-determined function of the power and speed.

Nanoforming

In the case of nanoforming, the rapid (~ 1 ms) ablation of the graphite layer results in no relative motion between the laser beam and the substrate during the patterning process. Considering a laser pulse of width τ incident normally on an IR window, the fraction of the incident energy transmitted through the window, accounting for Fresnel reflection losses and

absorption within the window, is f_T . The effective energy supplied to the substrate in a time τ is $f_T f_P P \tau$. Therefore, we calculate the dose ($D_{nanoforming}$) for a beam of spot size d as

$$D_{nanoforming} = \frac{f_T f_P P \tau}{\frac{\pi d^2}{4}} = \frac{4 f_T f_P P \tau}{\pi d^2}.$$

2.3.4 Nanoscale Deformation Mechanisms of R2RLIS

To understand the underlying mechanism of R2RLIS and to estimate the critical strain rate necessary to activate superplasticity in metals, we investigated the nanoforming of Au films by combining finite element method (FEM) and molecular dynamics (MD) simulations with atomic force microscopy (AFM), see Figure 2.10, 2.12.

MD simulations reveal that the strains suffered by the metal during the nanoforming process are much higher on the areas closer to the corners and edges of the nanomold than inside the nanomold due to a nanoscale geometrical confinement effect and a low-temperature dynamic recrystallization (Figure 2.10a). The new grain boundaries generated during the nanoforming process efficiently absorb dislocations, prevent dislocation avalanches and strain bursts, and enable the reduction of the grain sizes (Figure 2.11), providing uniformity to the nanoforming process and enabling the fabrication of nanostructures with ultrasoft surfaces. According to FEM simulations (Figure 2.10b,c), this high-strain-rate deformation process induces a low temperature rise on the nanomold ($\leq 90^\circ\text{C}$), which is efficiently dissipated by the Ti/epoxy composite, preserving the structural integrity of the nanomold after the nanoforming process (Figure 2.6). The generation of complex stresses (Figure 2.10b) facilitates the nucleation of subgrains and grains, reducing the grain size. We experimentally found that laser power densities lower than 1.45 MW/cm^2 were not able to generate enough pressure to activate superplasticity in $5\text{-}\mu\text{m}$ -thick Au films. This critical nanoforming laser intensity depends on the mechanical properties of the metallic film, its thickness, the efficiency of the confinement layer, and the thickness of the graphite ablation layer.

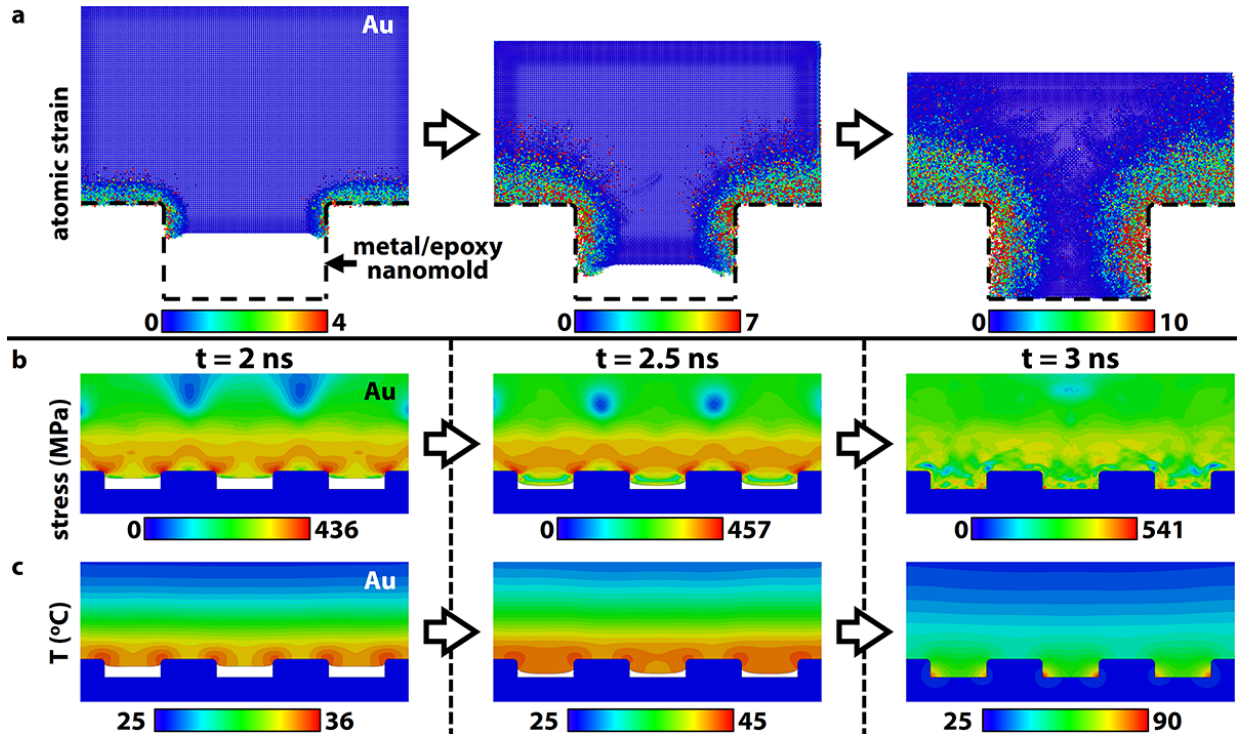


Figure 2.10. Multi-scale simulations describing the mechanisms of R2RLIS. (a) Atomic snapshots from MD simulations showing the evolution of atomic strain distribution as a single-crystal Au slab flows superplastically into the nanomold. The atoms at the edges and corners of the mold experience large strains while a low strain field exists in the interior regions. (b, c) Coupled thermo-mechanical FEM simulations showing the stress distribution and temperature rise in an Au slab during R2RLIS. $t = 0$ is defined as the instant at which the graphite layer ablates, triggering the superplastic flow of the metal. High-strain-rate processes like R2RLIS (the nanoforming time is ~ 3 ns) are realized by a low-temperature dynamic recrystallization, as predicted by the low temperature rise ($\leq 90^\circ\text{C}$) in the Au slab.

2.3.5 Tunability of the Mechanical and Optical Properties of the Fabricated Nanostructures

Figure 2.12 shows the increase of the hardness of several metal films processed by R2RLIS using a flat silicon wafer as a mold. We used AFM nanoindentation to characterize the strength of the metal films before and after R2RLIS. The hardness of as-received Au films is ~ 1.96 GPa, whereas the hardness of the film after R2RLIS is ~ 2.55 GPa (30% increase, see Figure 2.12a). Similarly, we achieved increments in the strength of Ag, Al, and Cu of 41.4%, 27.6%, and 25.8%, respectively (Figure 2.12b, 2.13). Additionally, the superplastic

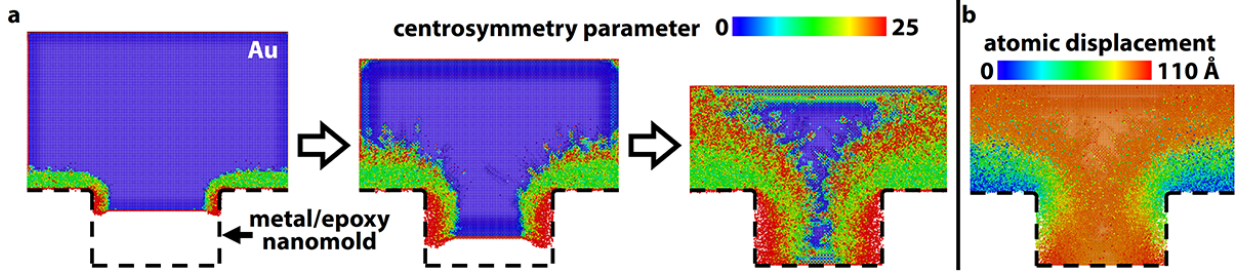


Figure 2.11. Atomic snapshots from molecular dynamics (MD) simulations. (a) Evolution of the microstructure of the gold film during the nanoforming process. The non-centrosymmetric values are visualized using OVITO, considering that for a gold atom on a perfect FCC lattice site, the centrosymmetry parameter is 0. When a dislocation is created, the centrosymmetry parameter increases to a larger positive value. The dislocation density increases greatly as the metal flows superplastically near the corners and edges of the nanomold. The crystalline structure of the gold becomes almost amorphous near the corners of the mold as a result of the severe plastic flow. (b) Absolute atomic displacement map indicating the flow pattern of the gold atoms during R2RLIS. Although the gold atoms at the edges and corners experience large atomic strains (Figure 2.10a), they have relatively small absolute displacements.

deformation of the metal film against a flat mold reduces the surface roughness of the metal significantly (from 41.8 nm to 1.2 nm in the case of 5- μm -thick Au films, see Figure 2.12c). Figure 2.12d,e shows that the improved strength and ultrasmooth surfaces of the fabricated nanostructures are due to the grain/subgrain refinement achieved during the nanoforming process, as predicted by MD simulations (Figure 2.10a). This increase in hardness of polycrystalline metallic films caused by grain size refinement is consistent with the Hall–Petch relation,¹²¹ $\text{hardness} \propto (\text{grain size})^{-0.5}$. Using high-resolution AFM, we found that R2RLIS decreases the grain sizes of an Au film from 117 ± 23 nm to 31 ± 4 nm, applying a laser power density of 4.77 MW/cm^2 . Since all grain sizes measured after R2RLIS were >10 nm, we can neglect small grain softening.¹²² We found that the laser power density irradiated over the ablation layer correlates with the grain boundary disorder imparted to the metal, increasing its hardness and reducing its surface roughness.

To demonstrate the nanomanufacturing of large-area arrays of plasmonic nanostructures active in the optical range using R2RLIS, we fabricated eleven Au nanogratings with different aspect ratios (Figure 2.14a). We chose Au as the plasmonic material due to its low ohmic loss at optical frequencies and its high oxidation resistance.¹²³ We fabricated all Au

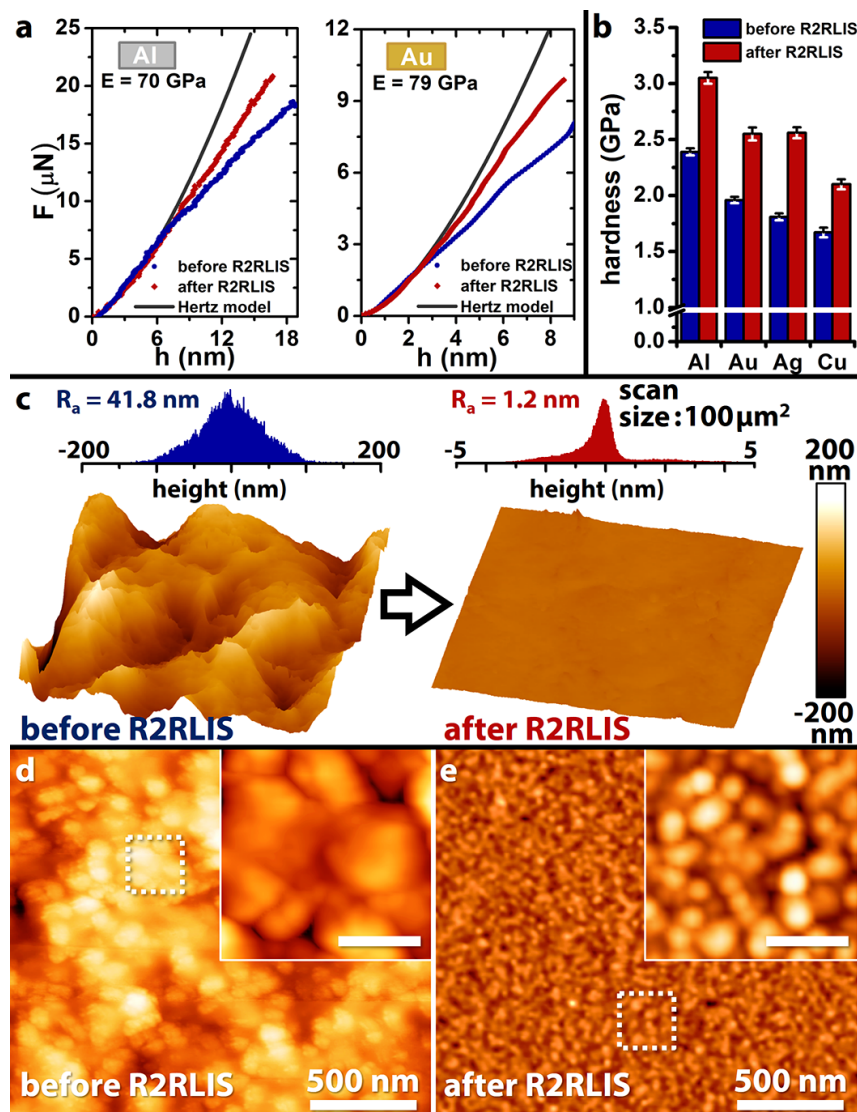


Figure 2.12. Strain hardening and grain refinement of the nanostructures fabricated by R2RLIS. (a) Force (F)–indentation depth (h) curves obtained by the AFM nanoindentation of Al and Au films showing the strain hardening due to R2RLIS. Deviation from the Hertz model indicates plastic deformation of the metals. Higher forces are required to attain equivalent indentation depths after R2RLIS. (b) Increase in hardness achieved by R2RLIS for Al (27.6% increase), Au (30% increase), Ag (41.4% increase), and Cu (25.8% increase). Error bars indicate standard deviation from 21 nanoindentations on each sample. (c) $10 \mu\text{m} \times 10 \mu\text{m}$ AFM topography images of Au surface before and after their nanoforming against a flat mold by R2RLIS. The histograms show that R2RLIS reduces the average surface roughness (R_a) from 41.8 nm to 1.2 nm. (d, e) $2 \mu\text{m} \times 2 \mu\text{m}$ AFM topography images showing the grain structure of the Au surface before and after R2RLIS. Insets show high-resolution scans of the indicated regions. The average grain size is reduced from 117 ± 23 nm to 31 ± 4 nm by R2RLIS. Scale bars in the insets are 100 nm.

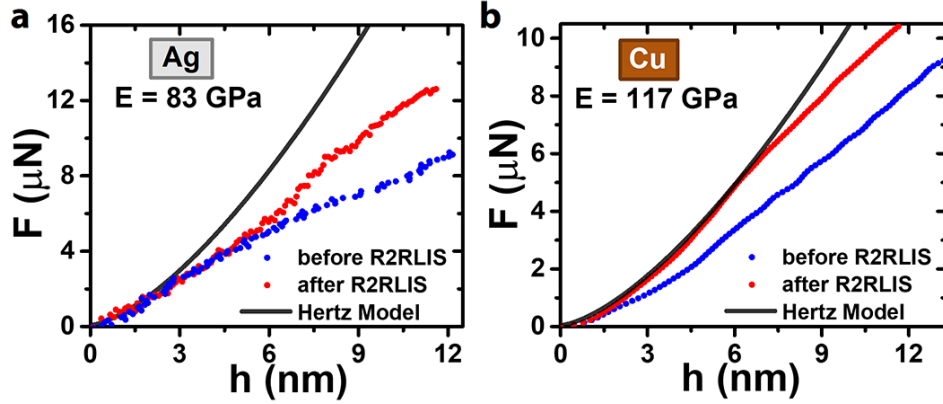


Figure 2.13. Force (F)-indentation depth (h) curves before and after R2RLIS for (a) silver, and (b) copper. Deviation from the Hertz model indicates plastic deformation of the metallic samples. The strain hardening of the metals nanoformed by R2RLIS is evident from the graphs: more force is required to attain equivalent indentation after R2RLIS.

nanogratings using the same Ti/epoxy nanomold (350 nm width, 220 nm depth); however, by applying different laser power densities during the nanoforming process, we obtained nanostructures with different aspect ratios and hardness values (Figure 2.14b). The capability of tuning the aspect ratio of the fabricated nanostructures by controlling the laser power used in R2RLIS enables the customization of the optical reflection of the resulting flexible plasmonic device from near-perfect reflection (Au flat surfaces planarized by R2RLIS) to near-zero reflection at $\lambda = 450 \text{ nm}$ (Au nanogratings 350 nm width and 140 nm height), see Figure 2.14c. Slight differences in the shape between the experimental resonance peaks and the finite difference time domain (FDTD) simulations are likely due to the losses in the experimental system. We found from further simulations that the reflection-dip red shifts as the height of nanograting increases (Figure 2.14e). To verify this point, we fabricated seven representative samples featuring nanogratings with heights of 50, 75, 100, 120, 136, 169, and 220 nm, as indicated by the white circles in Figure 2.14e. The closeness of the minimum reflection values—measured experimentally using a UV-Vis-NIR spectrophotometer—to the FDTD model predictions, demonstrates that R2RLIS can be used for the large-scale production of ultrasmooth plasmonic nanostructures of sufficient quality for optical applications (Figure 2.14f).

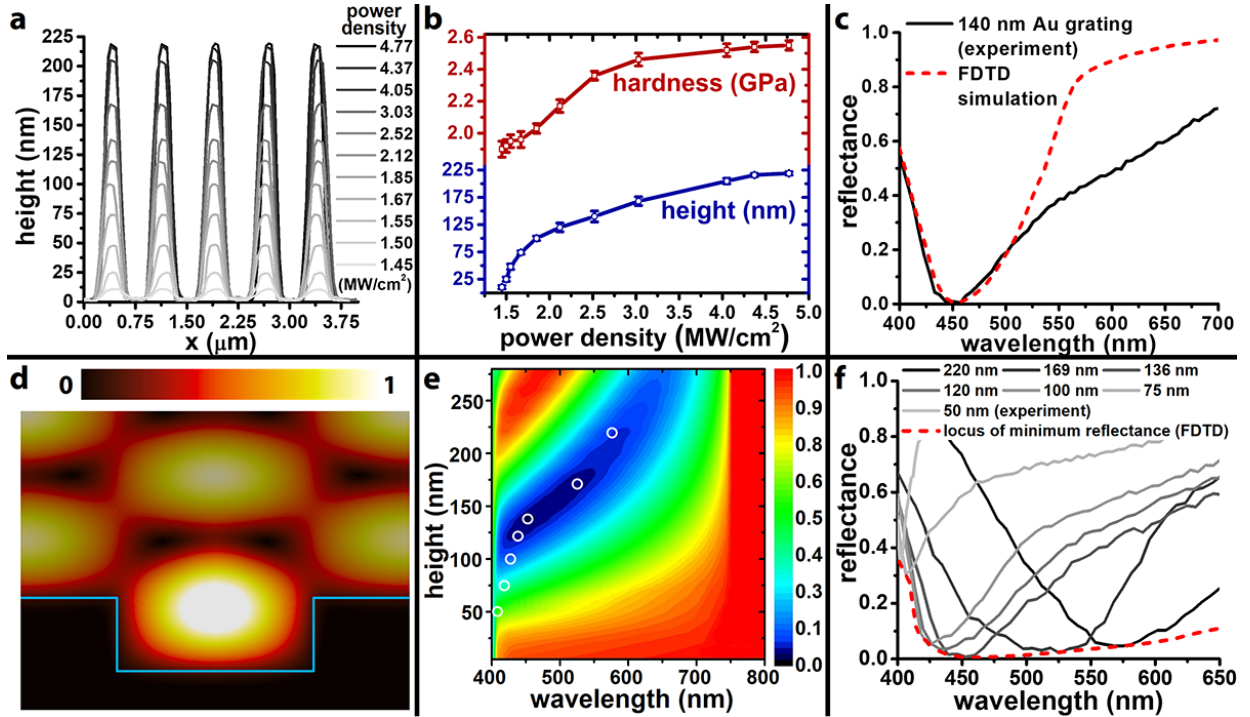


Figure 2.14. Controlling the aspect ratio and the optical properties of the fabricated nanostructures by tuning the laser power applied during R2RLIS. (a) AFM cross-section of the Au nanogratings patterned on an Au film by applying different laser power densities. All nanogratings were formed using the same Ti/epoxy nanomold (222 nm height and 350 nm linewidth). (b) Dependence on the power density of the height and hardness of the fabricated nanostructures. (c) Comparison of the experimental reflectance at normal incidence of an Au grating produced by R2RLIS with the FDTD simulation of the same grating with an idealized geometry (140 nm height and 350 nm linewidth). (d) Simulated normalized electric field distribution of the Au grating measured in panel (c) under TM polarized incident light at the wavelength of 450 nm. (e) Map of the reflectance of the gold nanogratings versus wavelength and height of the nanostructures. The linewidth is fixed to 350 nm. White circles indicate the minimum reflection values obtained from experimental reflectance measurements. (f) Experimental reflection spectra of seven representative Au nanogratings with specific heights. The locus of the minimum reflectance of the experimental measurements are in good agreement with FDTD simulations.

2.4 Conclusion

R2RLIS enables the rapid and inexpensive fabrication of ultra-smooth metallic nanostructures over large areas using conventional CO_2 engravers. Using low-cost metal/epoxy nanomolds, the minimum feature size obtained by R2RLIS was 40 nm, facilitating the rapid fabrication of flexible near-perfect absorbers at visible frequencies with the capability to

wrap around non-planar surfaces. R2RLIS has five significant advantages over other roll-to-roll nanomanufacturing processes: (i) it generates ultrasmooth metallic nanostructures using laser-induced superplasticity, overcoming coarse grain limitations on nanoforming; (ii) it can be performed at ambient conditions using conventional CO₂ engravers; (iii) it is scalable and inexpensive, using low-cost nanomolds easily fabricated by replica molding; (iv) it can attach the nanopatterned metallic films to flexible polymeric substrates with sufficient interfacial strength for practical applications; (v) tuning the laser intensity applied in the nanoforming process, enables the control of the final hardness and aspect ratio of the fabricated nanostructures. R2RLIS, at its present level of development, also has two limitations: (i) the rastering time of CO₂ lasers with small beam diameters limits the roll-to-roll fabrication speed. The use of wider or multiple beams has the potential to increase the speed of this roll-to-roll process at the cost of requiring laser systems with a higher power; (ii) the remnants of the graphite ablation coating are trapped between the metal film and the flexible substrate, which does not affect the fabrication of reflection-based optical devices, but could affect the performance of multifunctional devices based on the 3D stacking of nanopatterned layers. The complete removal of the residual graphite would require an additional step in the roll-to-roll process, increasing its complexity. The method proposed to fabricate ultrasmooth metallic nanostructures mounted on flexible substrates, however, is versatile and compatible with metals with Young's modulus as high as 130 GPa. R2RLIS, with the appropriate design of the nanomolds and configuration of the laser, could be extended to the cost-effective scalable fabrication of crystalline nanostructures for the development of future electronic, biosensing, and optical devices.

2.5 Experimental Section

2.5.1 Confinement layers for R2RLIS

We used CaF₂ or ZnSe optical windows (Thorlabs, Inc., Newton, NJ) to confine the expansion of the ablated graphite layer upon laser irradiation, since both materials exhibit a relatively low absorption at $\lambda = 10.6 \mu\text{m}$ (Figure 2.4). We use the confinement layer to drive the generated shockwave towards the metal/nanomold interface, inducing the superplastic

flow^{115,116} of the metal during the roll-to-roll nanoforming process. CaF₂ and ZnSe windows were not damaged by the CO₂ laser pulses even after more than one thousand printing cycles since the temperature reached by the graphite plasma was not enough to dry etch these materials. Additionally, the CO₂ laser intensities required to enable R2RLIS (\sim MW/cm²) were much lower than the breakdown threshold of CaF₂ and ZnSe (\sim GW/cm²),¹²⁴ see Figure 2.5.

2.5.2 Substrate Preparation

We used shims (5–8 μ m thick) of gold, silver, copper, and aluminum (Arnold Magnetic Technologies, Rochester, NY) as substrates for R2RLIS. We coated the back of the metallic films with a 5- μ m-thick graphite layer by spraying an aerosol lubricant (MG Chemicals, Burlington, Ontario, Canada). After the graphite ablation layer was dried with nitrogen, we rolled the metallic film on a feed roller (15.2 cm wide) and loaded it in a custom-made roll-to-roll system (Figure 2.1a, 2.2b) to perform R2RLIS.

2.5.3 Fabrication of the metal/epoxy nanomolds used in R2RLIS

To overcome the dependence of laser-based imprinting methods on expensive hard molds, we used soft lithography principles to fabricate epoxy nanomolds *via* replica molding.²⁷ We sputter-coated the fabricated epoxy nanomold with 50 nm of titanium, creating the Ti/epoxy nanomolds used to perform R2RLIS (see Figure 2.1a, 2.6, 2.2a, 2.3a).

To create the epoxy nanomolds, we used a variety of hard masters for soft replica molding: Polymeric gratings were obtained from DVDs and Blu-Ray discs (Sony Corp., USA). SiO₂ spectrometer gratings were obtained from Ibsen Photonics (UVVIS1250-702). Other arrays of silicon nanostructures, created by combining electron beam lithography (EBL) with reactive ion etching (RIE) and anisotropic KOH etching, were also used as hard masters.²²

Functionalization of hard silicon masters

Silicon-based hard masters were functionalized by exposure to vapors of tridecafluoro-1,1,2,2-tetrahydrooctyl-1-trichlorosilane (TFOCS; United Chemical Technology, cat. no. 6H-

9283) obtained by evaporating 100 mL of TFOCS in the desiccator where we kept the hard master and the silane at ~ 36 Torr for 5 h.¹²⁵ After silanization, the surface of the master becomes hydrophobic, preventing polydimethylsiloxanes (PDMS) to adhere to the master. We used the silanized silicon and SiO₂ masters to fabricate at least 20 copies of PDMS-based stamps without experiencing any significant adhesion during the unmolding process.

Fabrication of the soft elastomeric composite stamps

To replicate arrays of nanostructures with aspect ratios higher than one or linewidths smaller than 500 nm we used an elastomeric composite stamp comprising a ~ 5 μ m layer of h-PDMS (replicating the nanostructures) and a ~ 3 mm layer of s-PDMS (used as back support for the h-PDMS layer).

Preparation of the h-PDMS layer: We thoroughly mixed 3.4 g of a vinyl PDMS prepolymer (VDT-731, Gelest Corp.), 18 mL of a Pt catalyst (platinum divinyltetramethyldisiloxane, SIP6831.1, Gelest Corp.), and one drop of a modulator (2,4,6,8-tetramethyl-tetravinylcyclotetrasiloxane, 87927, Sigma-Aldrich) and degassed the mixture for 1 min. After all bubbles disappeared from the mixture, we added 1 g of a hydrosilane prepolymer (HMS-301, Gelest Corp.) and mixed it gently to prevent the formation of new bubbles. After stirring for ~ 30 s, the resulting mixture was spin-coated over the functionalized silicon master at 1000 rpm for 40 s and cured at 70 °C for 10 min.

Preparation of the s-PDMS (Sylgard 184, Dow Corning) layer: We thoroughly mixed the precursors of the base to a cross-linking agent at a ratio of 10:1 by weight. The air bubbles present in the prepolymer mixture were degassed at ~ 36 Torr for 30 min.

Assembly of the h-PDMS and s-PDMS layers: After the cured h-PDMS layer coating the silicon master was allowed to cool to room temperature, we cast a ~ 3 mm layer of Sylgard 184 PDMS (s-PDMS, Dow Corning) and baked the ensemble at 60 °C for 2 h. This curing time and temperature assures a good bond between the h-PDMS and the s-PDMS layers.

Fabrication of epoxy nanomolds using soft replica molding

After cutting and releasing the elastomeric composite stamp from the surface of the master, we used it to pattern an uncured layer of epoxy spread over a PET film (VWO100C-BE, Apollo Inc.). We achieved our best replica molding results using UVO-114 (Epotek), which is a UV-curable epoxy ($\lambda = 365 \text{ nm}$).¹²⁶ After several replica molding steps, the resulting epoxy nanostructures covering the PET film were metallized with 50 nm of titanium and wrapped onto a tensioned belt (15.2 cm wide), see Figure 2.2a.

Reusability of metal/epoxy nanomolds

We examined the structural integrity of the different Ti/epoxy nanomolds used in this study after performing multiple R2RLIS nanoforming cycles. Figure 2.6 shows that, even after using the Ti/epoxy nanomolds 75 times, the molds used to fabricate the nanostructures with the highest aspect ratios shown in this work do not show any significant degradation. Since the laser power density used in R2RLIS ($\sim \text{MW}/\text{cm}^2$) is several orders of magnitude less than that of pulsed nanosecond lasers ($\sim \text{GW}/\text{cm}^2$), the Ti/epoxy nanomolds can be reused up to 90 times during the roll-to-roll nanoforming process.

2.5.4 R2R set-up

We performed R2RLIS using a custom-made roll-to-roll system built inside a commercial CO₂ laser engraver (MT3050D; MornTech Inc., Stockton, CA). The metal film, coated with $\sim 5 \mu\text{m}$ of graphite on one side, is loaded as described in Figure 2.2. The plastic substrate, serving as a flexible support for the fabricated nanostructures, is also used during the R2R process to pull from the thin metal film, thanks to the action of the rubber-coated rolls used in our system (Figure 2.2b). After the metal film is nanoformed under the ZnSe confinement layer, the metal film and the plastic substrate are brought to contact with the metallic nanostructures facing up. A second irradiation with the CO₂ laser can be used to weld the metal film to the underlying plastic film over the scanned areas (Figure 2.1a₂, 2.7c, 2.2c).

2.5.5 Microscopic imaging

Scanning electron microscopy (SEM)

Scanning Electron Microscope (SEM) images of nanostructures fabricated by R2RLIS were taken using an FEI NOVA NanoSEM at 5.0 kV electron accelerating potential, spot size 3.0 and working distances between 3–5 mm. Low magnification images were obtained using an Everhart–Thornley Detector (ETD), while high magnification images were obtained using a Through–Lens Detector (TLD).

Atomic force microscopy (AFM)

AFM topography images were obtained in tapping mode using a Veeco Dimension 3100 AFM (Nanoscope III controller) with Tap300–G probes (BudgetSensors, Sofia, Bulgaria) having an average force constant of 40 N/m, resonant frequency in the range 250–300 kHz, and a tip radius ~ 10 nm.

2.5.6 Nanomechanical characterization

We used an Atomic Force Microscope (Dimension 3100 with Nanoscope III controller, Veeco) to characterize the hardness of the metal films tested in this study, before and after R2RLIS patterning, using nanoindentation force curves (Figure 2.12a, 2.13). Tap–150 DLC probes (BudgetSensors, Sofia, Bulgaria) with tip radius ~ 15 nm coated with a ~ 5 nm layer of diamond like carbon (DLC) were used for the nanoindentation experiments (Figure 2.16a). The force constant (k) of the cantilever was sufficiently high to induce the plastic deformation of the metallic samples, while still allowing for the extraction of the material properties in the elastic regime. The raw photodiode signal V_{pd} (in Volts) can be converted into a loading force (F) using the equation $F = kSV_{pd}$, where S is the cantilever sensitivity (in nm/V), see Figure 2.16b. To make quantitative comparisons from the force curves in terms of the force as a function of the indentation depth (h), it is necessary to obtain accurate values for k and S . A precise value for k can be readily calculated using Sader’s method^{127,128} when the resonant frequency, quality factor, and the geometry of the cantilever are known. S can be

experimentally determined from the slope of a force curve on a hard sample (e.g. Si, mica or sapphire),¹²⁹ so that the entire Z movement of the cantilever after contacting the sample can only be attributed to the deflection of the cantilever (Figure 2.15).

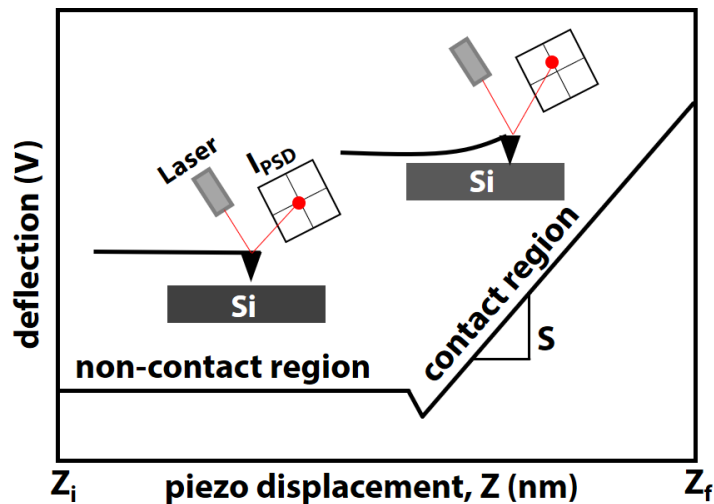


Figure 2.15. Determination of AFM cantilever sensitivity for nanomechanical characterization. Cantilevers are calibrated on a Si sample ($E \sim 180$ GPa), used as a non-deformable substrate to guarantee that all the photo-current (I_{PSD}) registered by the photodiode is attributed to pure deflection and no indentation. Schematics show the tip-substrate interaction in the non-contact and contact regions: when the tip is not in contact with the sample, there is no deflection and the laser spot in the photodiode is centered. The sensitivity of the cantilever is determined from the inverse of the slope of the contact region.

To calculate the hardness of a sample, we used the average value of at least 21 indentations performed on different locations over the sample, using a ramp speed of 50 nm/s. Although the AFM cantilever tip has a pyramidal geometry, the apex of the tip contacting the sample during nanoindentation can be assumed to have a hemispherical shape (Figure 2.16a inset). We first scanned the surface of the sample using non-contact tapping mode, chose a representative area, and performed the indentations. All the indentations were at least $1 \mu\text{m}$ apart to prevent interaction between deformation zones (Figure 2.16c).

Our nanoindentation system registered the applied force exerted by the tip of the cantilever as a function of the piezo displacement Z (Figure 2.16d). We then converted the piezo displacement to indentation depth h using standard force-curve analysis techniques available in the literature (Figure 2.16e).¹³⁰ The obtained $F-h$ curves were compared to the

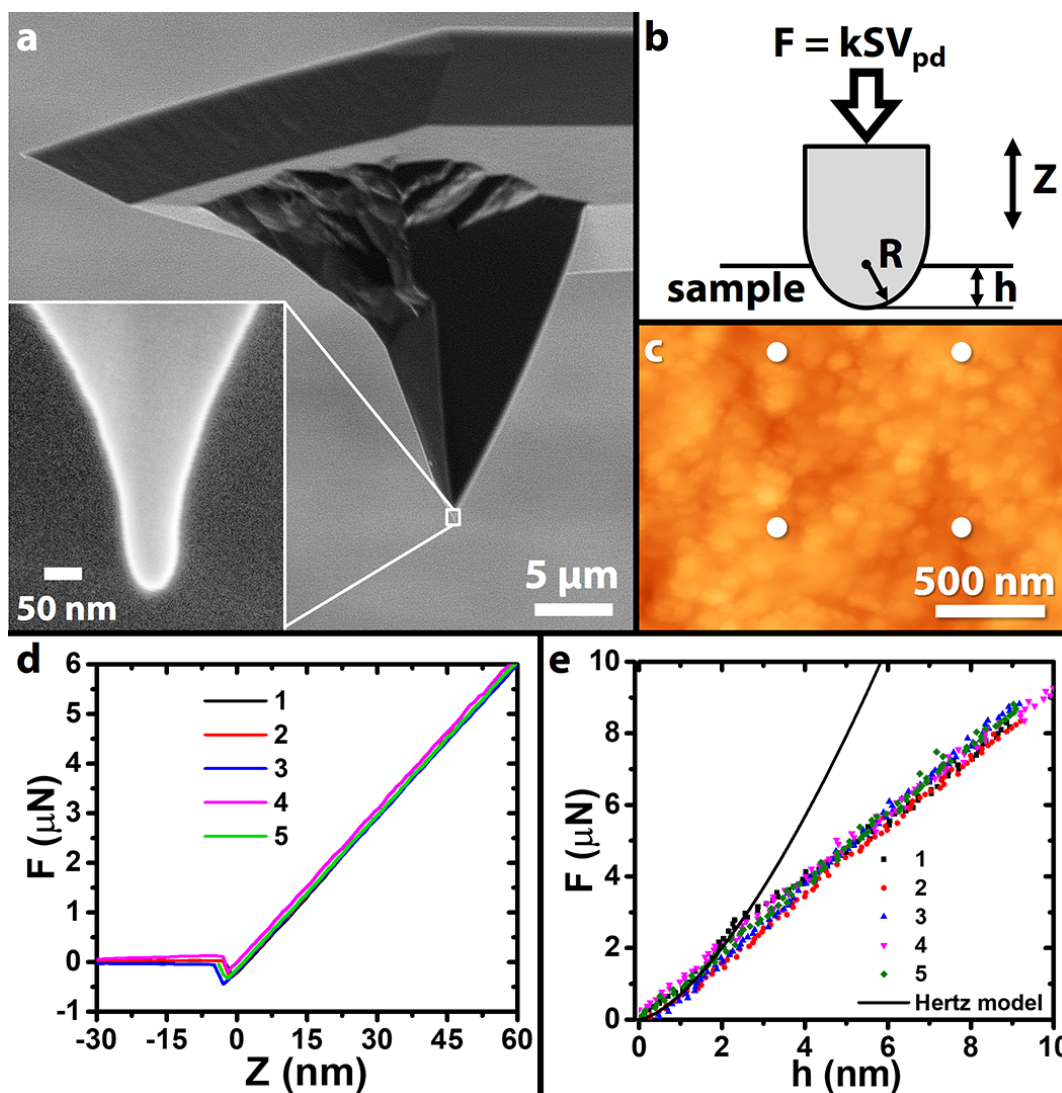


Figure 2.16. Nanomechanical characterization using AFM nanoindentation. (a) Representative SEM image of a Si cantilever tip coated with 5 nm DLC used for AFM nanoindentation. Inset shows that the end of the tip may be assumed to be spherical with radius $R \sim 20$ nm. (b) AFM topography image of one of the gold samples used to fabricate flexible plasmonic devices. The four white dots indicate the location of the indentations, spaced at least $1 \mu\text{m}$ apart to prevent interacting plastic deformation zones resulting from neighboring indentations. (c) Schematics of the experimental parameters describing the Hertz model. The force F on the cantilever is calculated as the cantilever spring constant (k) multiplied by the cantilever sensitivity (S) and the photodiode voltage (V_{pd}). h is the indentation depth and Z is the piezo displacement. (d) F - Z curves for nanoindentations performed at 5 locations on a gold sample nanoformed against a flat silicon wafer by R2RLIS. (e) Corresponding F - h curves for the 5 indentations showing the reproducibility of measurements. The Hertz model ($E = 79$ GPa) overlaps with experimental results during the elastic deformation of the sample.

theoretical Hertz Model,¹³¹ $F = (4/3)E^*R^{0.5}h^{1.5}$, where R is the tip radius and E^* is the effective Young's modulus of the tip-sample combination. E^* can be evaluated from:

$$\frac{1}{E^*} = \frac{1 - \nu^2}{E} + \frac{1 - \nu_i^2}{E_i},$$

where E and ν are the Young's modulus and Poisson's ratio of the sample respectively, and E_i and ν_i are for the indenter. The Poisson's ratio for all metals used in this study is assumed to be 0.33. When the force curves are close to the Hertz model, the deformation is elastic. Deviation from the Hertz model indicates permanent plastic deformation (Figure 2.16e). We divided the maximum force by the projected the area of the indenter at the corresponding indentation depth to obtain the hardness of the sample.¹³²

2.5.7 Molecular dynamics simulations

To investigate the evolution of the grain structure and the dislocations in the metal film (Figure 2.11a), and the distribution of atomic strain (Figure 2.10a) and displacement (Figure 2.11b) during R2RLIS, we performed molecular dynamics (MD) simulations using the open-source MD package LAMMPS (Oct 23, 2017 version, 64-bit).¹³³

To simplify the simulation, the Ti/epoxy nanomolds used in R2RLIS were modeled as if they were the hard silicon masters used for their fabrication (silicon with a diamond structure of lattice constant 5.48 Å). The lack of deformation of the Ti/epoxy nanomolds after R2RLIS is consistent with the previously described behavior of hard silicon molds,⁴⁷ in agreement with our approximation (see Figure 2.6). The metal film is modeled as single crystalline Au with an FCC structure of lattice constant 4.078 Å. The width of the grooves is 30 times (16.44 nm) the Si lattice constant and the depth is 20 times (10.96 nm). The metal slab thickness is 55 times (22.429 nm) the Au lattice constant. This leads to a simulation box containing ~ 1.78 million atoms. Periodic boundary conditions are implemented in the x and y directions, while "shrink-wrapped" fixed boundary conditions are employed in the z direction (to prevent any loss of atoms). An atomic snapshot of the simulation setup is depicted in Figure 2.17.

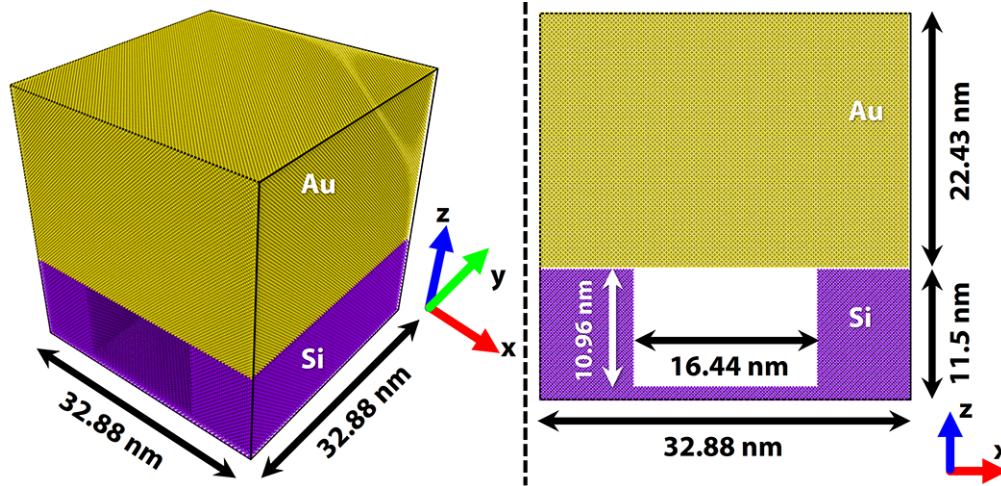


Figure 2.17. MD simulation domain. The supercell is composed of a silicon mold with a groove of 16.44 nm width and 10.96 nm depth. The gold slab measures 32.88 nm \times 32.88 nm \times 22.43 nm. Boundaries are periodic in x and y directions. “Shrink-wrapped” boundary conditions are applied in the z direction.

Since two types of atoms (Si and Au) are involved, hybrid pair-styles are used: Tersoff potential (Si.tersoff)¹³⁴ is used for silicon, EAM potential (Au_u3.eam)^{135,136} is used for gold, and Lennard–Jones (LJ) potential is used to account for the van der Waals (vdW) interactions between silicon and gold atoms. The $\sigma_{\text{Si–Au}}$ and $\epsilon_{\text{Si–Au}}$ parameters of the $\text{LJ}_{\text{Si–Au}}$ potential for Si–Au interactions are determined from LJ_{Si} (Si–Si interactions)¹³⁷ and LJ_{Au} (Au–Au interactions)¹³⁸ using the Lorentz rule (the effective σ is the arithmetic mean of individual σ ’s) and the Berthelot Rule (the effective ϵ is the geometric mean of the individual ϵ ’s). The cutoff distance for the $\text{LJ}_{\text{Si–Au}}$ potential is set to $2.5\sigma_{\text{Si–Au}}$.¹³⁹

To trigger the nanoforming process, an initial velocity of 80 Å/ps (= 8 km/s) in the $-z$ direction is applied to the Au atoms resting on the nanoscale features of the Si mold (fixed rigid). Our choice of the initial speed is reasonable, since shock waves travel through the propagating medium at speeds higher than speed of sound¹⁴⁰ (speed of sound in gold = 3.24 km/s).

The MD simulation is performed using a microcanonical (constant number of particles, constant volume, constant energy; NVE) ensemble with a time-integration step of 0.001 ps. Atomic snapshots were taken using the open-source visualization tool OVITO 2.9.0 (<https://ovito.org>).¹⁴¹

2.5.8 Finite element analysis

We performed finite element method (FEM) simulations to determine the localized stress (Figure 2.10b) and temperature rise (Figure 2.10c) in a gold film during nanoforming by R2RLIS. The computational limitations of current MD packages make it infeasible to simulate the temperature field at the nanosecond timescale in multi-million atom systems. Our FEM study, therefore, complements the MD results described above, and provides insight into the coupled thermo-mechanical behavior of the system.

Fabbro's model¹¹⁴ is employed for calculating the peak pressure (1.5 GPa) of the shock wave generated by the CO₂ laser.¹⁴² Since the laser beam spot size ($\sim 40 \mu\text{m}$) is much larger than the calculation domain ($\sim 2 \mu\text{m}$), the shockwave propagation can be assumed to be one dimensional. The Johnson-Cook strain-sensitive plasticity model¹⁴³ suitably describes the high strain-rate ($10^6\text{--}10^7 \text{ s}^{-1}$) deformation of metals in transient dynamic conditions, as shown below:

$$\bar{\sigma} = [A + B (\bar{\epsilon}^{pl})^n] \left[1 + C \ln \left(\frac{\dot{\bar{\epsilon}}^{pl}}{\dot{\epsilon}_0} \right) \right] [1 - \hat{\theta}^m]$$

where $\bar{\sigma}$ is the yield stress at non-zero strain-rate, A , B , C , n , m , and $\dot{\epsilon}_0$ are material parameters measured at or below the transition temperature θ_t . $\hat{\theta}$ is the dimensionless temperature defined as

$$\hat{\theta} \equiv \begin{cases} 0 & \text{for } \theta < \theta_t \\ (\theta - \theta_t) / (\theta_{melt} - \theta_t) & \text{for } \theta_t \leq \theta \leq \theta_{melt} \\ 1 & \text{for } \theta > \theta_{melt} \end{cases},$$

where θ is the current temperature, θ_{melt} is the melting temperature, and θ_t is the transition temperature. For temperatures below θ_t , the yield stress is no longer temperature dependent. $\bar{\epsilon}^{pl}$ is the equivalent plastic strain and $\dot{\bar{\epsilon}}^{pl}$ is the equivalent plastic strain rate.

The gold film was simulated with the Johnson-Cook hardening model described above using parameters available in the literature.⁴⁸ Temperature rise is considered by setting the inelastic heat fraction for plastic flow to 0.9, i.e. 90% of the work of plastic deformation is converted to heat in the thermal energy balance. The simulation was implemented in

Abaqus/CAE 6.13-1 (Simulia Corp., Providence, RI) using CPE4RT plane strain elements with 4-node bilinear displacement and temperature, reduced integration, and hourglass control.

2.5.9 Optical characterization

One of the primary goals of this study was to fabricate metallic nanostructures over large areas with sufficient quality for optical applications. To characterize the reflectance spectra of the nanostructure arrays produced by R2RLIS, we used a UV-Vis-NIR spectrophotometer (Perkin Elmer Lambda 950) in the spectral range of 200 nm–2.4 μm . A gridless photomultiplier (PMT) acts as the detector in the UV-Vis range, while a Peltier-cooled PbS detector is used in the IR range. The detector change wavelength is set at 790 nm. All measurements were performed with a fixed slit width of 4.0 nm for both detectors, and data interval of 2.0 nm, with the sample placed inside an integrating sphere. To ensure that the resonance peak exhibited by the gold nanostructures was not caused by the non-linear behavior of the gold film at optical wavelengths, we also collected reference spectra from flat gold films obtained by performing R2RLIS against a (100) silicon wafer.

2.5.10 Finite-difference time domain (FDTD) simulations

We used a commercial FDTD solver, Microwave Studio (CST GmbH, Germany), to simulate the reflection of the electromagnetic waves at the ultrasmooth nanostructures fabricated using R2RLIS. We simulated a unit cell of the metallic nanograting, as shown in Figure 2.18, applying the following periodic boundary conditions:

1. x - z plane: perfect electric conductor,
2. y - z plane: perfect magnetic conductor,
3. Open boundary conditions sealed by Perfectly Matched Layers (PML) are placed in the perpendicular direction of the top device surface. A TM wave propagating through this transmission line was simulated using two waveguide ports placed on the open boundaries.

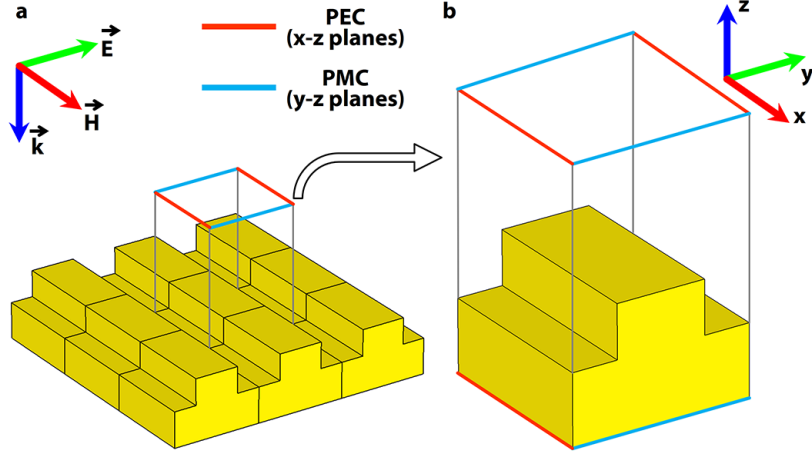


Figure 2.18. Schematics of the FDTD simulation domain used to model gold nanogratings. (a) Direction of the propagation \vec{k} , electric field \vec{E} , and magnetic field \vec{H} of the incident optical waves. (b) Representative unit cell of the gold nanogratings simulated in Figure 2.14. Perfect Electric Conductor (PEC) conditions were applied to the boundaries parallel to the x - z plane and Perfect Magnetic Conductor (PMC) conditions were applied to the boundaries parallel to the y - z plane.

The waveguide ports on the open boundaries of the transmission line, produced two complex frequency dependent S -parameters, S_{11} and S_{21} . We calculated the reflectance as $R(\omega) = |S_{11}|^2$. The thickness of the metal film prevented waves in the optical range to be transmitted across the material. We used a graded mesh to accurately discretize the geometry of the metallic nanostructures fabricated by R2RLIS. A maximum mesh size of 3 nm was used within the metallic nanostructures and a maximum mesh size of 20 nm was used to discretize the free space. The size of the mesh was enforced to change by a maximum factor of 1.4 per mesh cell. We modeled the dispersive complex dielectric function of gold over the range of wavelengths of 0.3–1.5 μm as a Drude metal,

$$\varepsilon = \varepsilon_{\infty} - \frac{\omega_p^2}{\omega^2 + i\Gamma\omega},$$

where $\varepsilon_{\infty} = 9$, $\omega_p = 1.38 \times 10^{16}$ rad/s, $\Gamma = 1.09 \times 10^{14}$ rad/s are the infinite frequency permittivity, the plasma frequency, and the collision frequency, respectively.⁹ Due to the experimental symmetries of the simulated grating, we could apply symmetric boundary conditions that reduced the requirement for computational resources by a factor of four.¹⁴⁴

CHAPTER 3. SCALABLE FABRICATION OF FLEXIBLE METASURFACES USING LOW-COST LASER DIODE ENGRAVERS

3.1 Introduction

In Chapter 2, we introduced R2RLIS, a roll-to-roll nanomanufacturing process that uses a CO₂ laser beam to nanoform metallic films and weld them to a flexible substrate. R2RLIS reduces the capital cost of equipment necessary for the laser-based direct nanopatterning of metals by a factor of 10 (when compared to Laser Shock Imprinting⁴⁷). R2RLIS employs infrared optical windows (ZnSe or CaF₂) as confinement layers to drive the generated shockwave toward the metal/nanomold interface, inducing superplastic flow.¹⁰² Although we demonstrated that these optical windows are undamaged up to 1000 laser pulses of the CO₂ laser, the long-term operation of R2RLIS requires the periodic replacement of these expensive (\$40/cm²) windows. At the operating wavelength of CO₂ lasers (10.6 μm), ZnSe has a transmission of ~71% while CaF₂ has a transmission of just ~11% (Figure 2.4), with all the absorbed energy being dissipated as heat inside the window and eventually damaging it upon prolonged operation. A cost-effective setup which circumvents this limitation is thus desirable to promote the adoption of R2RLIS in both academic and industrial settings. In this chapter, we explore the possibility of using a portable ~\$200 laser diode engraver (15 W; λ = 450 nm; [amazon.com](https://www.amazon.com)) as the laser source in R2RLIS, which then allows us to use conventional glass slides (soda-lime-silica glass) as the confinement layer (<\$0.02/cm²; transmission ~90% at 450 nm). This portable laser engraving system reduces the capital equipment cost by a further factor of 25 (compared to R2RLIS using CO₂ laser engravers) with comparable nanoforming performance.

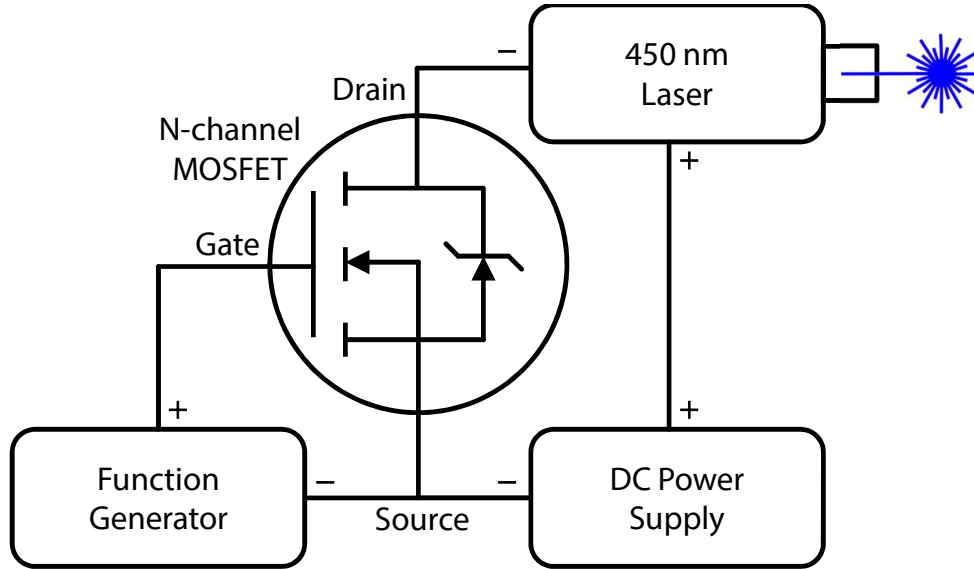


Figure 3.1. Schematic diagram of the electronic circuit used to pulse a 450 nm diode laser.

3.2 Results

We first set up an electronic circuit consisting of an N-channel MOSFET, a function generator, and a DC power supply to pulse the diode laser at a desired pulse width and power fraction (Figure 3.1). We then performed experiments using Si nanomolds (fabricated by electron beam lithography and wet etching) and gold foils to fabricate high-fidelity, ultrasmooth nanostructures (Figure 3.2). Ultra-sharp features of nano-pyramid arrays (Figure 3.2b) can be successfully reproduced by diode-laser-induced superplastic nanoforming. Such pyramidal nanostructures have been commonly used in surface-enhanced Raman scattering (SERS), due to the strong field enhancement achieved when surface plasmons propagating along non-adjacent faces converge at the tip of the pyramid.^{47,145}

The grain refinement observed previously in R2RLIS using CO₂ lasers (Figure 2.12) is also observed when using diode lasers, as evidenced by the AFM images in Figure 3.3. The reduction in average grain size of the gold foil from 202 ± 78 nm (before LIS) to 67 ± 7 nm (after LIS) is consistent with the Hall–Petch relation,¹²¹ $\text{hardness} \propto (\text{grain size})^{-0.5}$. Moreover, the nanoforming process makes the grains more uniform in size, as evidenced by the significantly lowered standard deviation of the grain sizes.

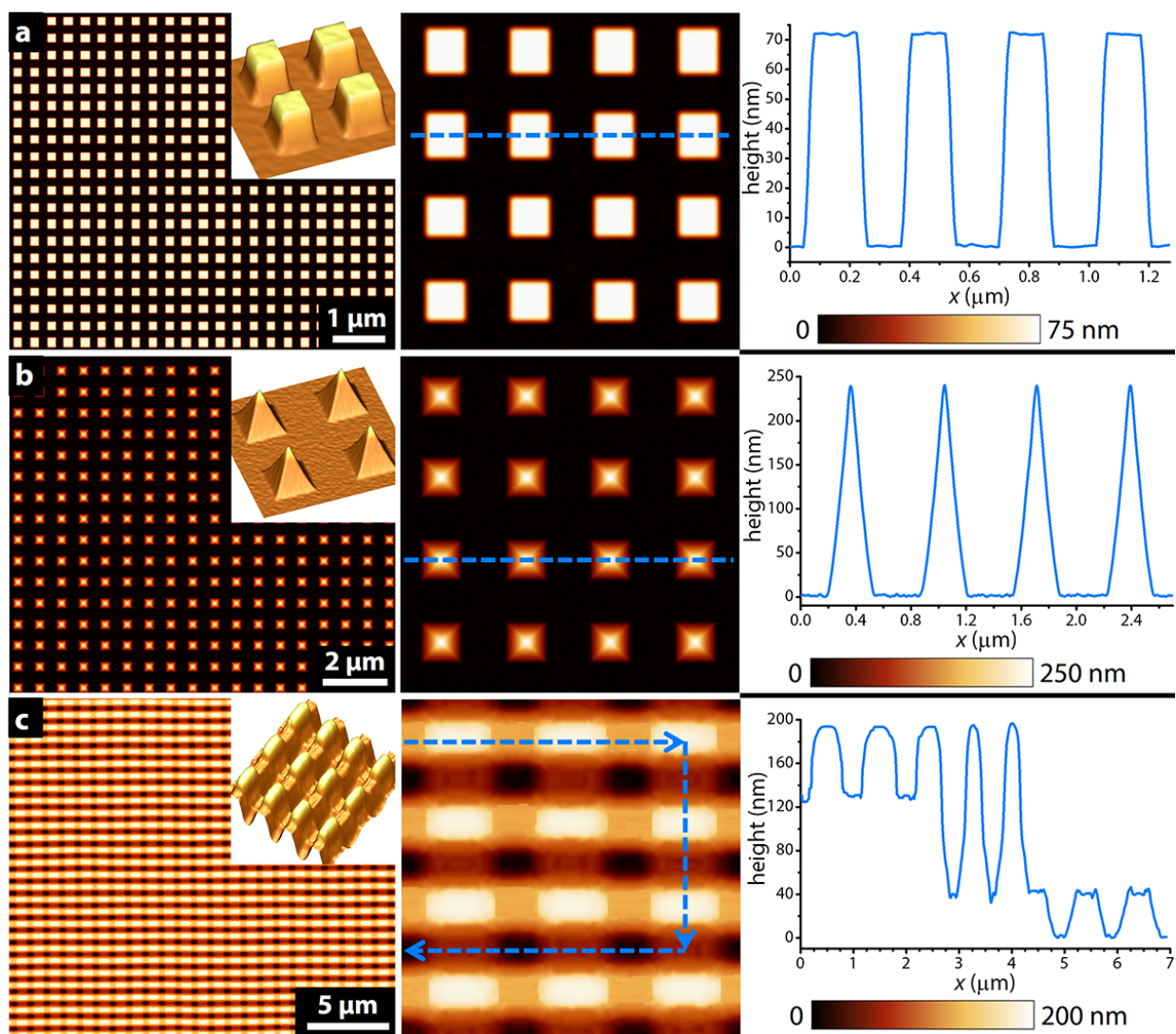


Figure 3.2. Ultrasmooth, 3D Au nanostructures fabricated by diode-laser-induced superplasticity. (a) Nanocuboid array with a period of 325 nm and a height of 75 nm. (b) Nanopyramids with tip-radius < 10 nm and height of ~ 250 nm. (c) Nanoscale fishnet fabricated by nanoforming the Au foil twice. Nanostructures are characterized using atomic force microscopy.

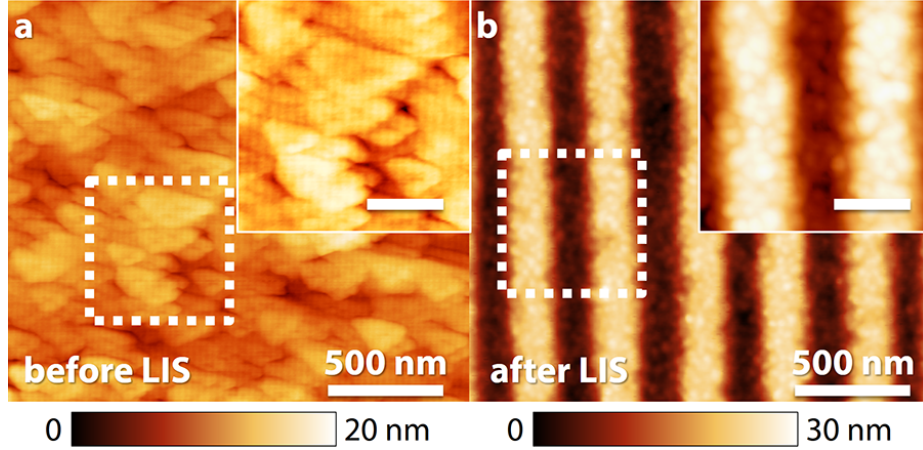


Figure 3.3. Grain refinement due to diode-laser-induced superplasticity. $2\ \mu\text{m} \times 2\ \mu\text{m}$ AFM topography images showing the grain structure of an Au foil surface (a) before and (b) after nanoforming. Insets are $600\ \text{nm} \times 600\ \text{nm}$. Inset scale bar is $200\ \text{nm}$.

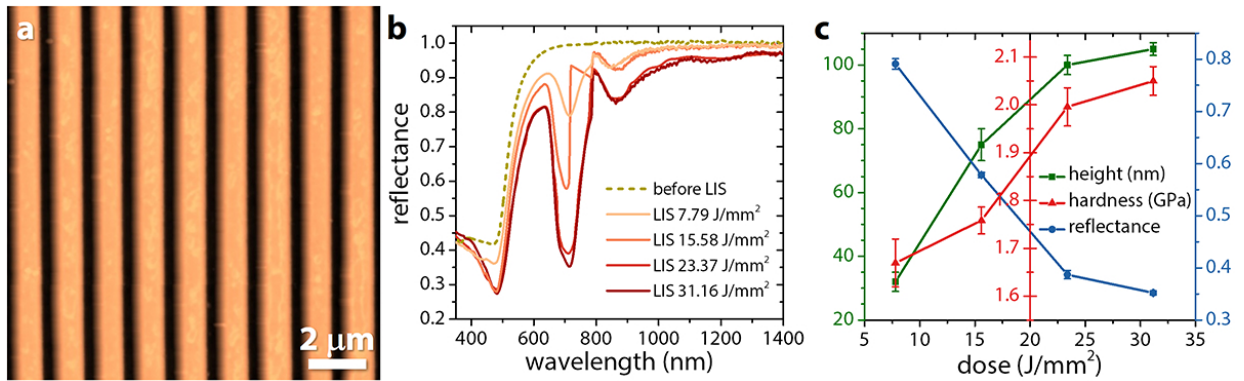


Figure 3.4. Modulating aspect ratio, hardness, and reflectance of Au nanogratings by tuning the power of the diode laser. (a) AFM topography image of an Au nanograting with a $350\ \text{nm}$ linewidth and a $110\ \text{nm}$ height. (b) Optical reflectance spectra of Au nanogratings of the same pitch ($700\ \text{nm}$) nanoformed at different diode laser doses. (c) Dependence of the height, hardness, and reflectance of Au nanogratings of $350\ \text{nm}$ linewidth on the nanoforming laser dose.

Since the aim of our proposed nanomanufacturing process is the production of flexible plasmonic metasurfaces, we verified that the nanostructures fabricated by diode-laser-induced superplasticity have sufficient quality for optical applications (Figure 3.4b). We used a UV-Vis-NIR spectrophotometer (Perkin Elmer Lambda 950) in the spectral range of $350\ \text{nm}$ – $1.4\ \mu\text{m}$ to experimentally measure the reflection spectra of the fabricated nanostructure arrays. Additionally, our results also demonstrate that the power of the incident diode

laser beam can be modulated to tune the aspect ratio, hardness, and optical properties of metallic nanostructures fabricated using the same mold (Figure 3.4c).

3.3 Conclusion

Diode-laser-induced superplastic nanoforming is a scalable and high-throughput method that further reduces the costs of an already inexpensive CO₂-LIS technique. The cost of the laser used in diode-LIS is ~ 25 times lower than that used in CO₂-LIS¹⁰² and ~ 250 times lower than Nd:YAG lasers used in Laser Shock Imprinting.⁴⁷ Moreover, diode-LIS mitigates another limitation of CO₂-LIS—the high replacement frequency and cost of the confinement layer. Since diode-LIS uses conventional glass slides instead of ZnSe or CaF₂ windows as the confinement layer, the replacement cost is lowered by a factor of over 2000.

CHAPTER 4. 3D-ARCHITECTED SOFT MACHINES WITH TOPOLOGICALLY ENCODED MOTION

Copyright 2019 Wiley. Used with permission from Ref.¹⁴⁶

4.1 Introduction

This chapter presents Architected Soft Machines (ASMs)—a form of low-density programmable matter—which encodes high-level robotic motion in its low-level topological architecture. ASMs can be designed by applying a Voronoi tessellation algorithm^{61,62,147,148} to the surface of any primitive solid (such as cuboids or cylinders); fabricated by 3D printing flexible photopolymers or by injection molding highly stretchable elastomers; and actuated by motor-tendons with minimal friction. A variety of high-level motions such as compression, twisting, bending, and cyclic motion can be encoded in the cellular topology of ASMs by controlling the beam orientation, cell size, or beam thickness of the Voronoi designs. Simple topological transformations applied to the primitive solids enable, after Voronoi tessellation, the design of ASMs with mechanical metamaterial behaviors. We demonstrate how existing complex computer-aided design (CAD) models can be converted to ASMs capable to perform multi-finger gripping or quadrupedal locomotion. Finally, we demonstrate that elastomeric ASMs with embedded functional components exhibit ultrahigh compression and stretching, heralding future applications in soft robotics and stretchable electronics. We also expect ASMs to be particularly advantageous in soft robotic applications requiring low density, independence from pressurized air sources, and the relatively fast response and simple control provided by tendon-based actuation.

4.2 Mathematical description of Voronoi tessellations and Delaunay triangulations

Given two sets A and B and a distance metric $d(a, b)$ defined for $a \in A$ and $b \in B$, a Voronoi tessellation is a subdivision of A into subsets, each of which contains the objects in A that are closer, with respect to the distance metric, to one object in B than to any other object in B .¹⁴⁷ Voronoi tessellations can be defined for many different sets and metrics. In this study, we consider the case for which the set A is a region of surface in Euclidean space, B is a finite set of points also in Euclidean space, and the metric is the Euclidean distance.

Consider an open bounded domain $\Omega \in \mathfrak{R}^d$ and a set of distinct points $\{\mathbf{x}_i\}_{i=1}^n \subset \Omega$. For each point \mathbf{x}_i , $i = 1, \dots, n$, the corresponding Voronoi region V_i , $i = 1, \dots, n$, is defined by $V_i = \{\mathbf{x} \in \Omega \mid \|\mathbf{x} - \mathbf{x}_i\| < \|\mathbf{x} - \mathbf{x}_j\| \text{ for } j = 1, \dots, n \text{ and } j \neq i\}$, where $\|\cdot\|$ denotes the Euclidean distance (the L^2 metric) in \mathfrak{R}^d . We refer to $\{V_i\}_{i=1}^n$ as the Voronoi tessellation of Ω associated with the point set $\{\mathbf{x}_i\}_{i=1}^n$.¹⁴⁸ A point \mathbf{x}_i is called a *generator*; a subdomain $V_i \subset \Omega$ is referred to as the Voronoi cell corresponding to the generator \mathbf{x}_i .

The dual of a Voronoi tessellation in the graph-theoretical sense (i.e., by connecting all pairs of neighbor generators) is called a Delaunay triangulation associated with the point set $\{\mathbf{x}_i\}_{i=1}^n$.

The MATLAB codes in the Appendix compute the Delaunay triangulation and Voronoi tessellation using the incremental Bowyer–Watson algorithm,¹⁴⁹ having a complexity of the order $O(n \log n)$ to $O(n^2)$.

4.3 Results

4.3.1 Design, Fabrication, and Actuation of ASMs

ASMs can be rapidly designed from any CAD model by applying an automated algorithm that first performs a Delaunay triangulation on the original lattice (topology) of the model, and then a Voronoi tessellation over the Delaunay triangles (Figure 4.1a; also see MATLAB codes in the Appendix). The Voronoi tessellation partitions the surface of the CAD model into cells using the vertices of the model (lattice points) as “seeds” or “generators”, such that

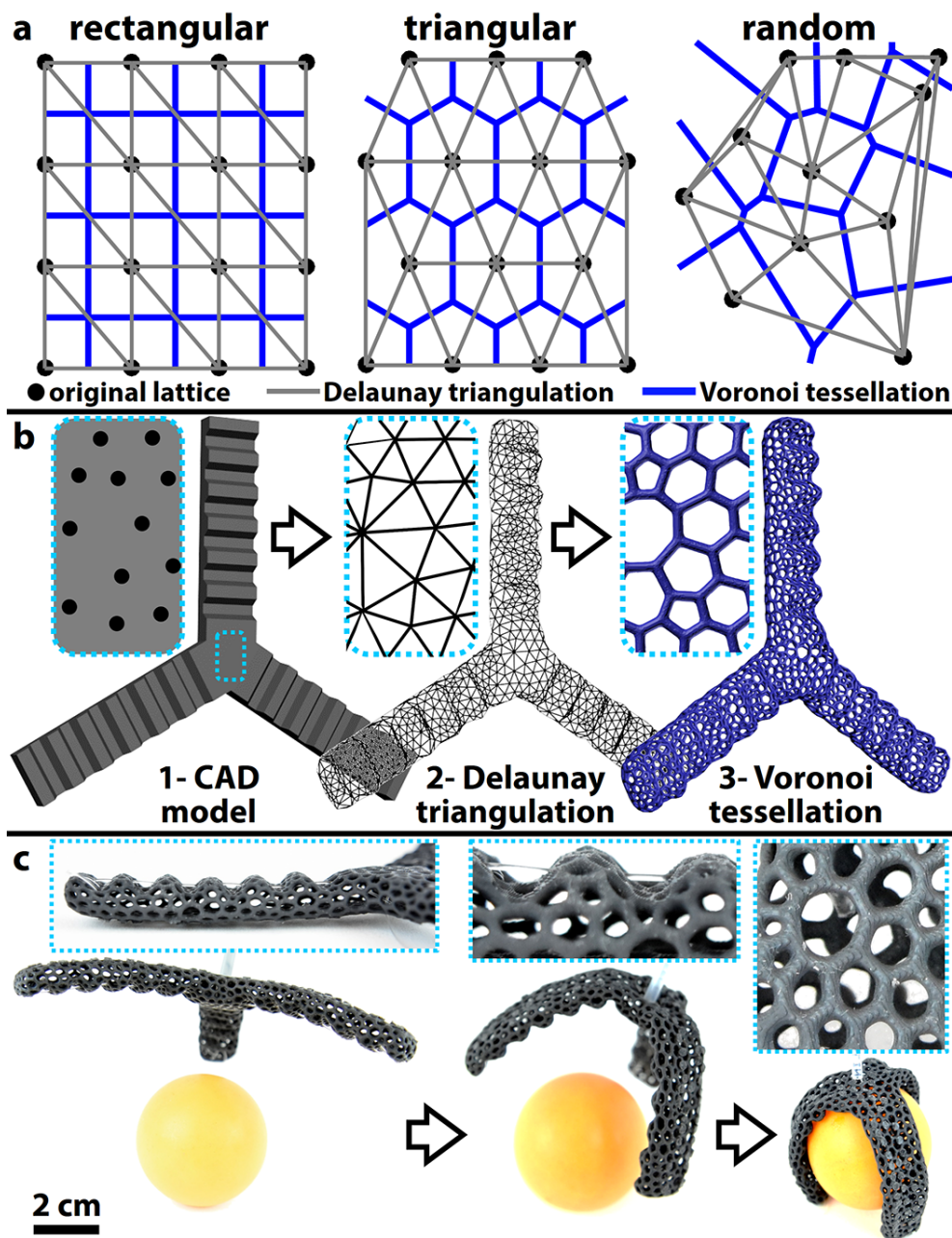


Figure 4.1. Design, fabrication, and actuation of ASMs. (a) Automated algorithms transform a set of lattice points to their Delaunay triangulation and Voronoi tessellation. Examples show rectangular, triangular, and random lattice arrangements. (b) Transformation of a simple model designed using commercial CAD software into its low-density ASM counterpart to design a functional gripper. The lattice points of the CAD model are randomly distributed. (c) Snapshots of the motor-tendon-based actuation mechanism of an ASM gripper 3D printed with a flexible photopolymer. Insets show the sparse, hollow structure, and how the nylon threads act as tendons to actuate the ASM gripper—enabling it to conformably grip a ping-pong ball.

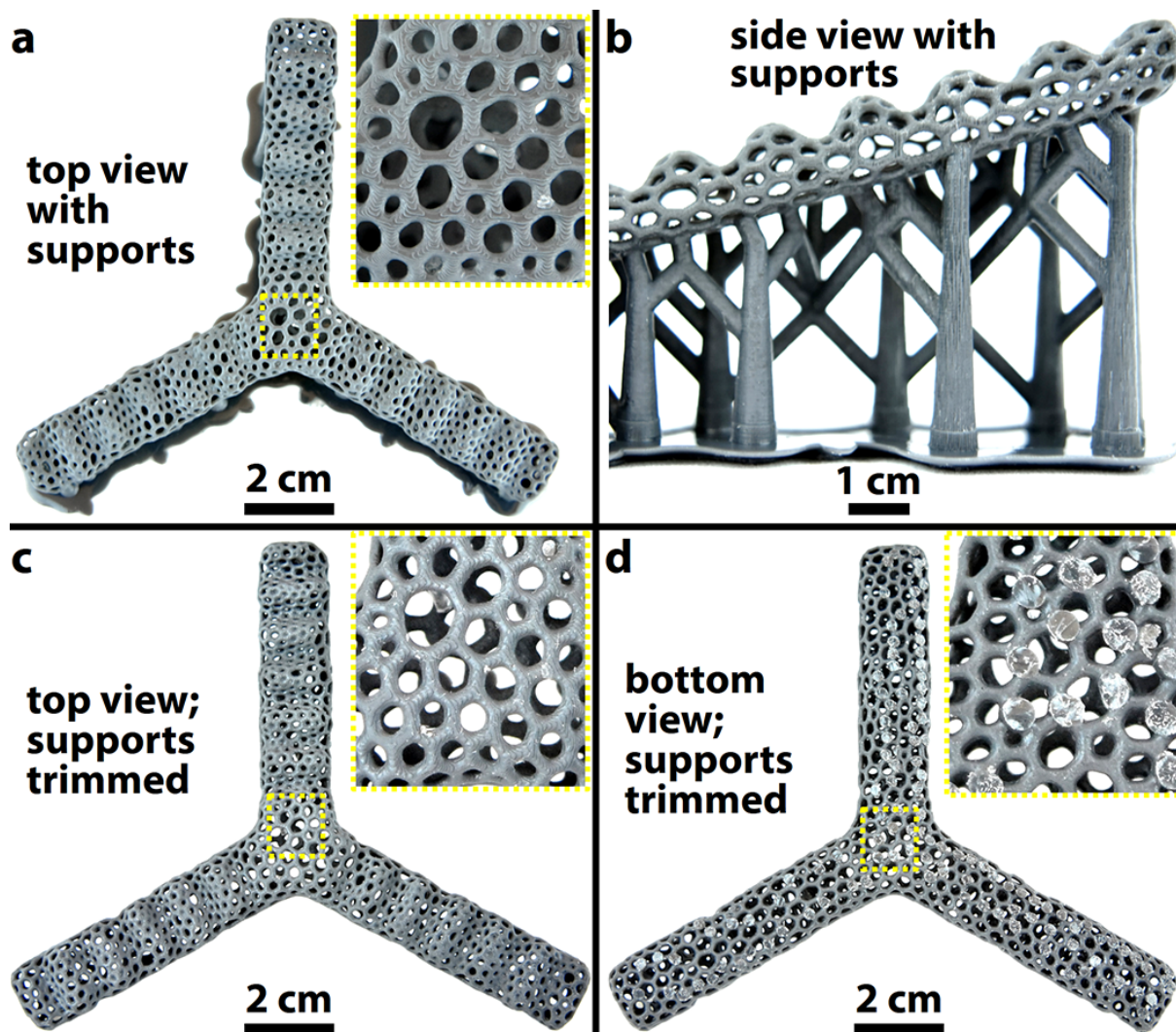


Figure 4.2. ASM gripper fabricated by 3D printing. (a) Top view of a 3D printed gripper with support structures. (b) Side view of the gripper showing the location and arrangement of the support structures. (c) Top view of the gripper (gripping surface), after the support structures are removed. (d) Bottom view of the gripper showing where the support structures were attached. The remnants of the support material on this (non-gripping) surface of the gripper do not affect its motion.

for each seed there is a corresponding cell consisting of all points closer to that seed than to any other.^{147,148} As a proof of principle, we show the simple and rapid design of a low-density soft gripper weighing 11.8 g (effective density = 0.28 g/cm^3 , 24% of bulk material), by combining standard primitives (cuboids) and applying the Delaunay and Voronoi algorithms to the model (Figure 4.1b). The resulting 3D-architected design is then 3D printed using a flexible photopolymer (Figure 4.2) to create an ASM. After the ASM is 3D printed, we

manually tied nylon threads to the Voronoi cells at the end of the soft gripper, passed these threads along its beam structure, and used small DC motors to compress the 3D-architected geometry and induce its controlled buckling to achieve conformal gripping (Figure 4.1c). This design, fabrication, and actuation approach enables users with minimal training in CAD modeling to rapidly create low-density soft machines with desired topologically encoded motion.

4.3.2 Programming Motion by Controlling Beam Orientation

The final motion of ASMs upon tendon actuation depends on their 3D architecture. Modifying the original topology of a 3D model using simple geometric transformations, it is possible to generate a wide range of ASMs exhibiting similar shapes but different beam configurations and final resulting motions (Figure 4.3). 3D models with rectangular lattices, such as the cylinder shown in Figure 4.3a, generate Voronoi-based architected structures with a 90° curve angle (α)—defined as the maximum acute angle that any beam in the structure makes with the horizontal (Figure 4.3b and Figure 4.4). After 3D printing, ASMs with $\alpha = 90^\circ$ exhibit pure compression upon tendon actuation, behaving as soft mechanical metamaterials with negative Poisson’s ratio (Figure 4.3c). The nominal stress–strain characteristics of this cylindrical ASM are significantly different from that of a solid cylinder 3D printed with the same photopolymer (Figure 4.5). The Voronoi cells of these auxetic ASMs accommodate compressive forces by collapsing along the compression axis (see Figure 4.6), preventing rotations (Figure 4.3i) and inducing negative Poisson’s ratio even when the cells are not reentrant.^{63,64}

Applying simple torsional transformations to the topology of right frustums allows for the generation, after Voronoi tessellation, of auxetic ASMs with different rotational actuation (see Figure 4.7). The magnitude of the torsion (ϕ) applied to the original frustum and the curve angle (α) of the resulting ASMs are experimentally found to be parabolically related (Figure 4.7b). Varying α from 40° – 90° enables the control of the rotation angle (θ) described by the top surface of the ASMs upon compression. Figure 4.3d–h demonstrates two representative examples of fabricated ASMs that undergo unidirectional and bidirectional twisting upon tendon-based actuation. The unidirectional twisting ASM ($\alpha = 55^\circ$;

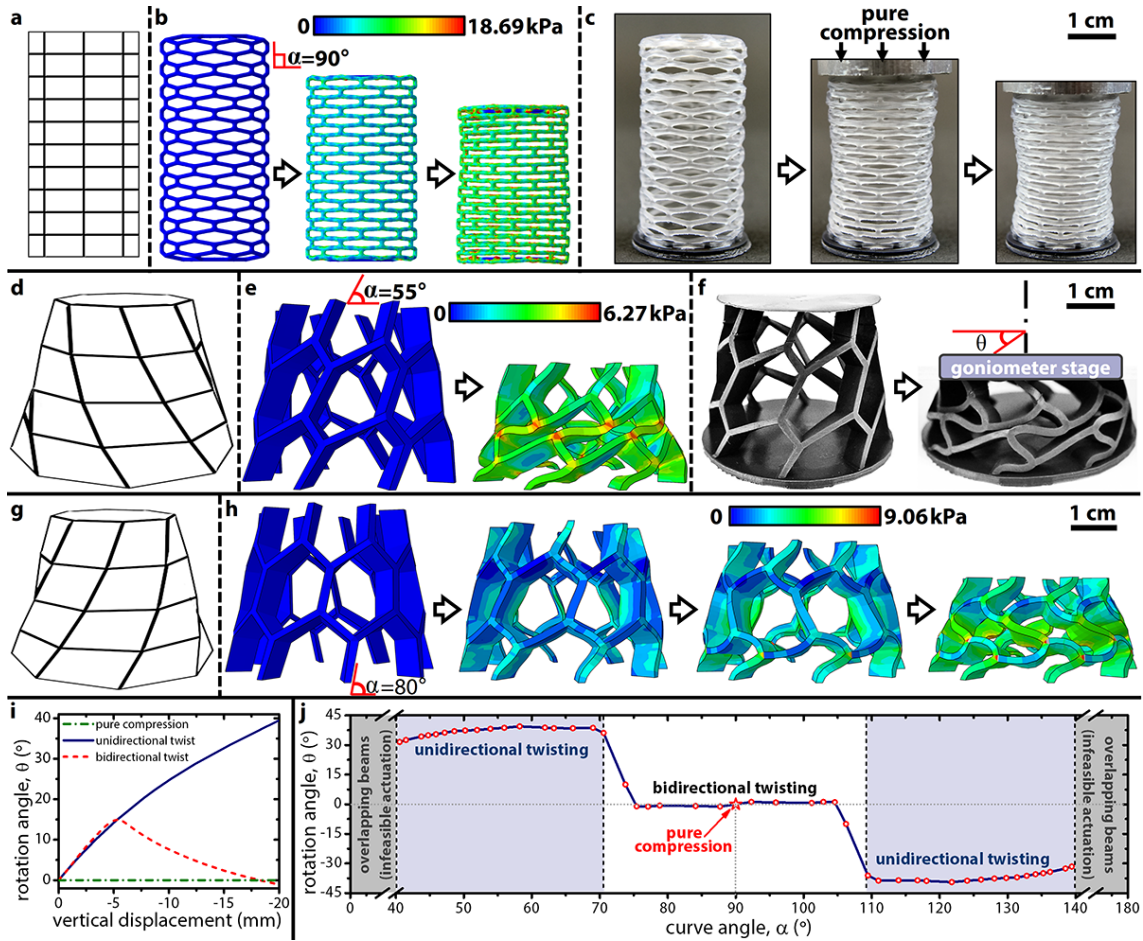


Figure 4.3. Programming motion of auxetic ASMs by controlling beam orientation. (a) Initial rectangular lattice used to design a compression ASM. (b) FEM simulation showing the stress distribution in an ASM designed for pure compression ($\alpha = 90^\circ$), as a displacement-controlled normal load is applied from the top. (c) Experimental demonstration of the negative Poisson's ratio exhibited by the ASM shown in (b). (d) Initial lattice used to design a unidirectional twisting actuator *via* Voronoi tessellation. (e) FEM simulation showing the stress distribution in the resulting ASM ($\alpha = 55^\circ$), under a displacement-controlled vertical load. (f) Experimental demonstration of the ASM shown in (e) twisting from $\theta = 0$ to 40° upon compression. (g) Initial lattice used to design a bidirectional twisting actuator. (h) FEM simulation showing the stress distribution in an ASM programmed for bidirectional twisting ($\alpha = 80^\circ$), under a displacement-controlled vertical load. The twisting direction of the top of the ASM switches from CCW to CW midway between the 2nd and 3rd frames shown, at a compression of ~ 5 mm (experimental realization in Figure 4.8). (i) Rotation of the top surface of the ASM as a function of the vertical displacement for compression and twisting ASMs. ASMs exhibiting pure compression do not rotate, while the rotation of unidirectional twisting ASMs increases monotonically with vertical displacement. The direction of rotation of bidirectional twisting ASMs switches at a vertical displacement of ~ 5 mm. (j) Actuation regimes obtained by varying the curve angle of the fabricated ASMs.

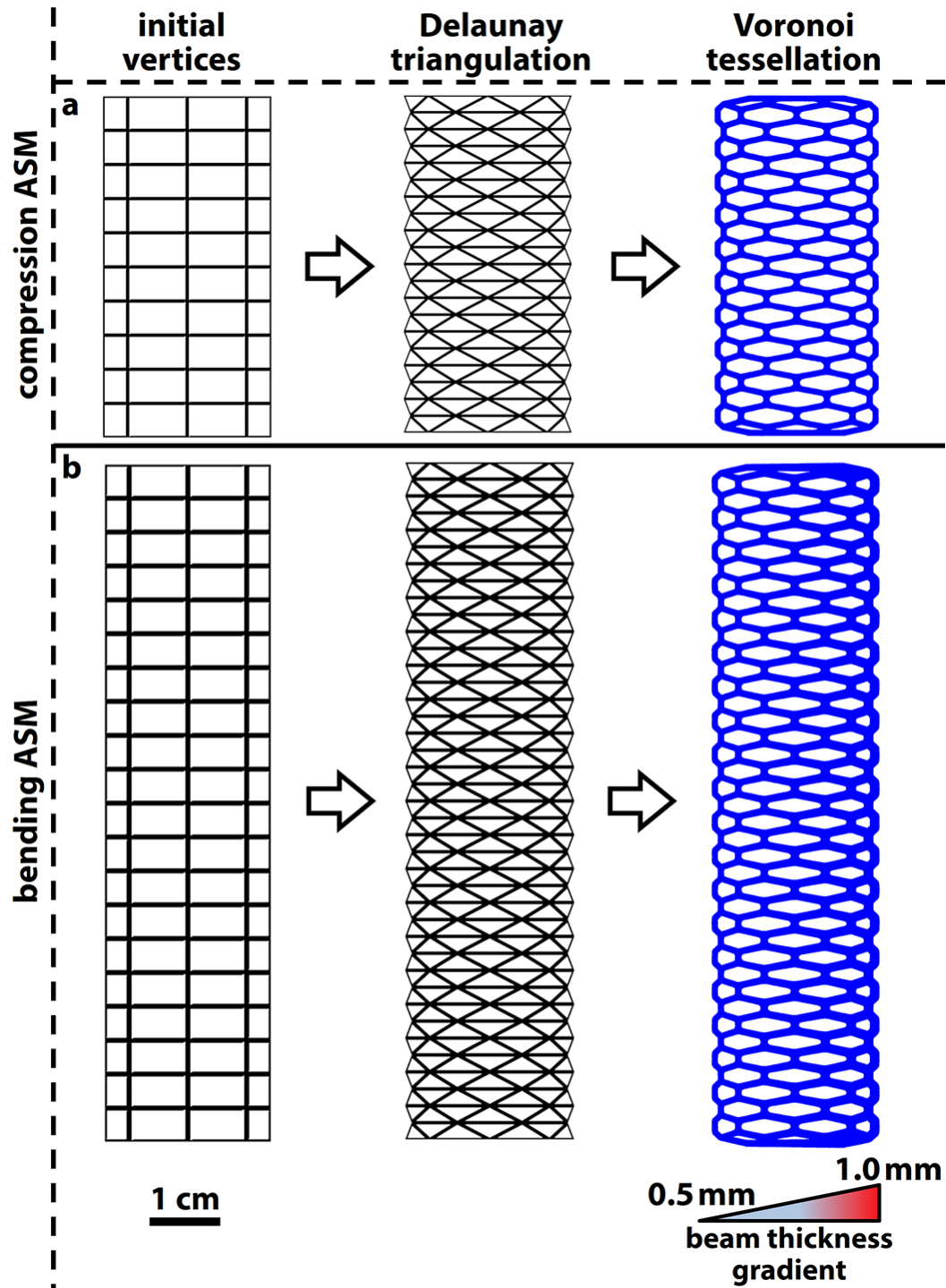


Figure 4.4. Initial vertices, Delaunay triangulation, and Voronoi tessellation for (a) pure compression ASM, and (b) bending ASM. Starting with the same basis of vertices, the pure compression ASM can be transformed into a bending ASM by applying a thickness gradient to its beams as shown in (b). The induced stiffness gradient enables the continuum bending of the ASM in a desired direction.

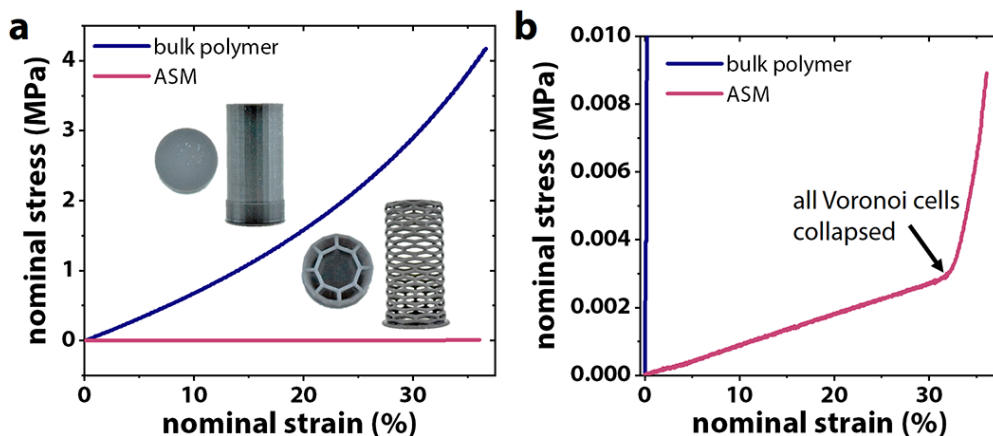


Figure 4.5. Comparison between the compressive nominal stress-strain characteristics of a solid cylinder and that of an ASM, both 3D printed with the same polymer, FLGR02 (v2 resin). (a) The ASM has an effective Young's modulus of ~ 0.0088 MPa, which is three orders of magnitude less than that of the bulk polymer ($E \approx 6.29$ MPa). Insets show the top and front views of the bulk and ASM samples used for the experiment. (b) Zoom-in of the stress-strain curve of the ASM showing its dual-stiffness behavior.

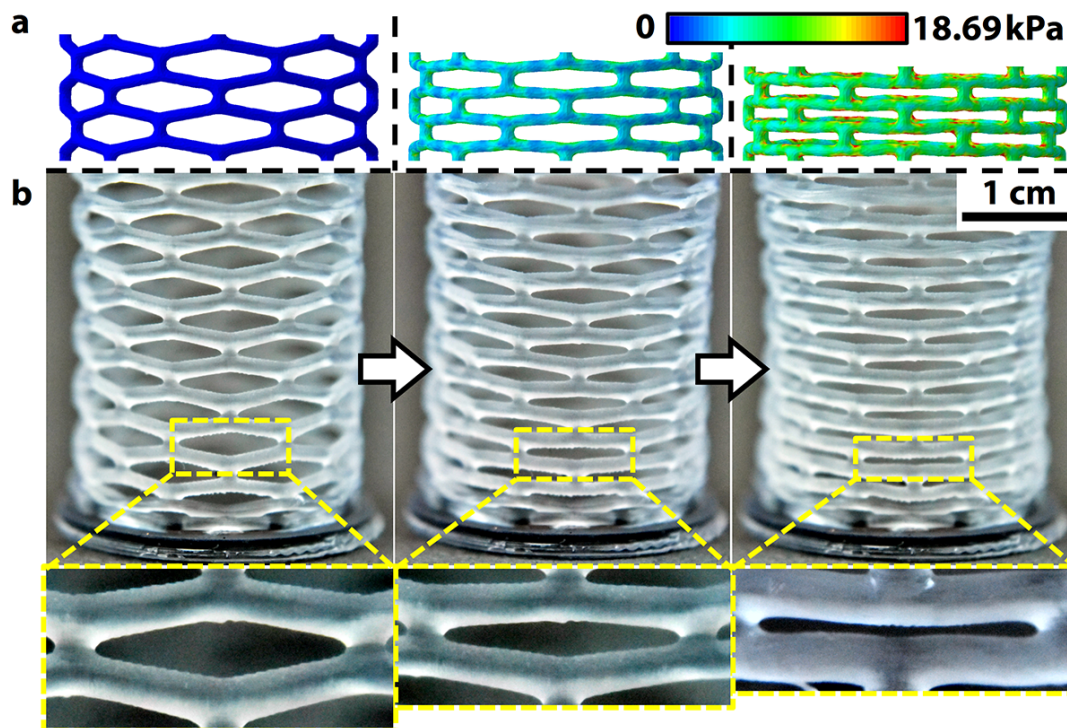


Figure 4.6. Pure compression ASM fabricated by 3D printing. (a) Finite element simulation and (b) experimental compression test showing the collapsing of the individual Voronoi cells of the ASM. The color bar in panel (a) represents the magnitude of the von Mises stress.

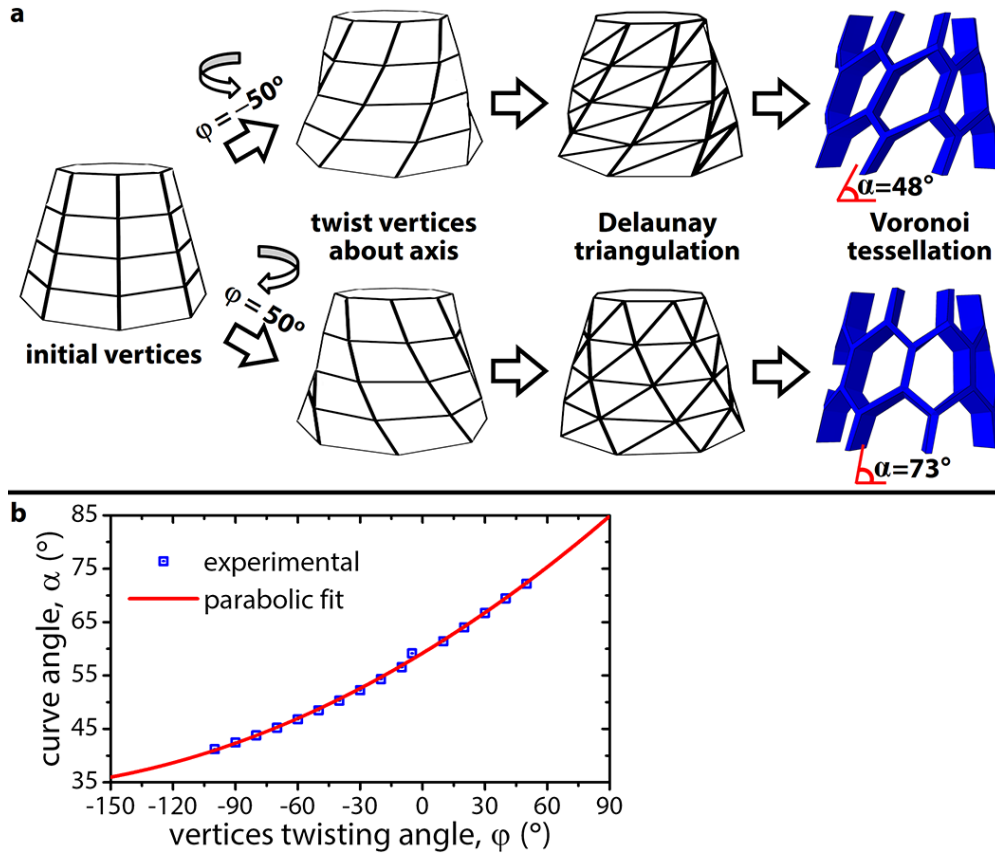


Figure 4.7. Design principle for twisting ASMs. (a) The initial set of vertices is defined by a solid CAD model. The model is then twisted about its vertical axis in the direction and angle desired, followed by application of the Delaunay triangulation and Voronoi tessellation algorithms. (b) The curve angle α (see Figure 4.3) is experimentally found to be parabolically related to the twisting angle ϕ .

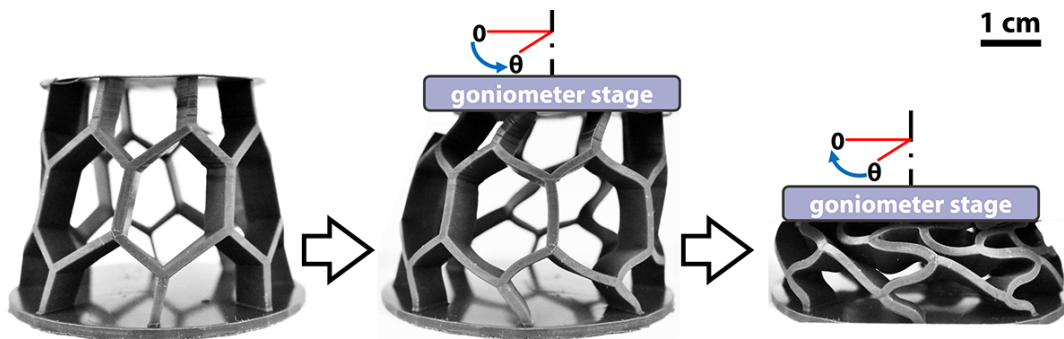


Figure 4.8. Bidirectional twisting ASM fabricated by 3D printing. The top surface of the ASM first rotates from $\theta = 0$ to 15° , while compressing 5 mm. Upon further compression, the direction of rotation reverses, returning to $\theta = 0^\circ$ at a compression of 20 mm.

Figure 4.3d–f) has a rotation angle that increases monotonically with compression, reaching a maximum rotation of $\theta = 40^\circ$ at a compression of 20 mm (Figure 4.3i). The bidirectional twisting ASM ($\alpha = 80^\circ$; Figure 4.3g, h and Figure 4.8) is a soft mechanical metamaterial whose top surface first rotates clockwise to a maximum of $\theta = 15^\circ$ at 5 mm compression, and then counterclockwise, returning to $\theta = 0^\circ$ at a compression of 20 mm (Figure 4.3i).

The application of topological torsional transformations to control the resulting α of the ASMs produces soft actuators with different twisting motions along the regimes depicted in Figure 4.3j. When α ranges from 40° – 70° , ASMs undergo unidirectional twisting, while $70^\circ < \alpha < 90^\circ$ induces bidirectional twisting in the ASMs. The regimes are symmetric about $\alpha = 90^\circ$, since obtuse angles only cause a reversal in sense. ASMs with $\alpha < 40^\circ$ or $\alpha > 140^\circ$ do not twist upon compression due to the physical contact among their beams. Since θ is almost constant within each of the regimes, unidirectional or bidirectional twisting motion can be encoded in the ASM without requiring an accurate control of α . ASMs with more slanted beams, however, require less force to be actuated, inducing lower stresses as predicted by the finite element method (FEM) simulations (Figure 4.3b, e and h).

4.3.3 Programming Motion by Tuning Beam Thickness

The motion of ASMs can be controllably modified by the simple incorporation of gradients and localized differentials in the thickness of the beams integrating their structure. As an example, ASMs with beam structures originally designed for pure compression (Figure 4.3a–c) can produce continuum bending on tendon actuation after applying a linear gradient of beam thickness perpendicular to the long axis (Figure 4.9a–c and 4.4). Similarly, it is possible to concentrate the bending at a desired location along the length of an ASM by combining multiple beam thickness gradients. Figure 4.9d shows an ASM where the application of orthogonal gradients enables the formation of a 90° elbow bend upon tendon-based compression along the indicated axis.

While it is straightforward for “hard” mechanical systems to accomplish cyclic motion (using wheels, axles, and bearings), the design of a soft actuator that generates rotary motion is not trivial.^{77,150} The local modification of beam thicknesses in ASMs enables the encoding of cyclic motion utilizing only a single structural component. To design a cyclic motion

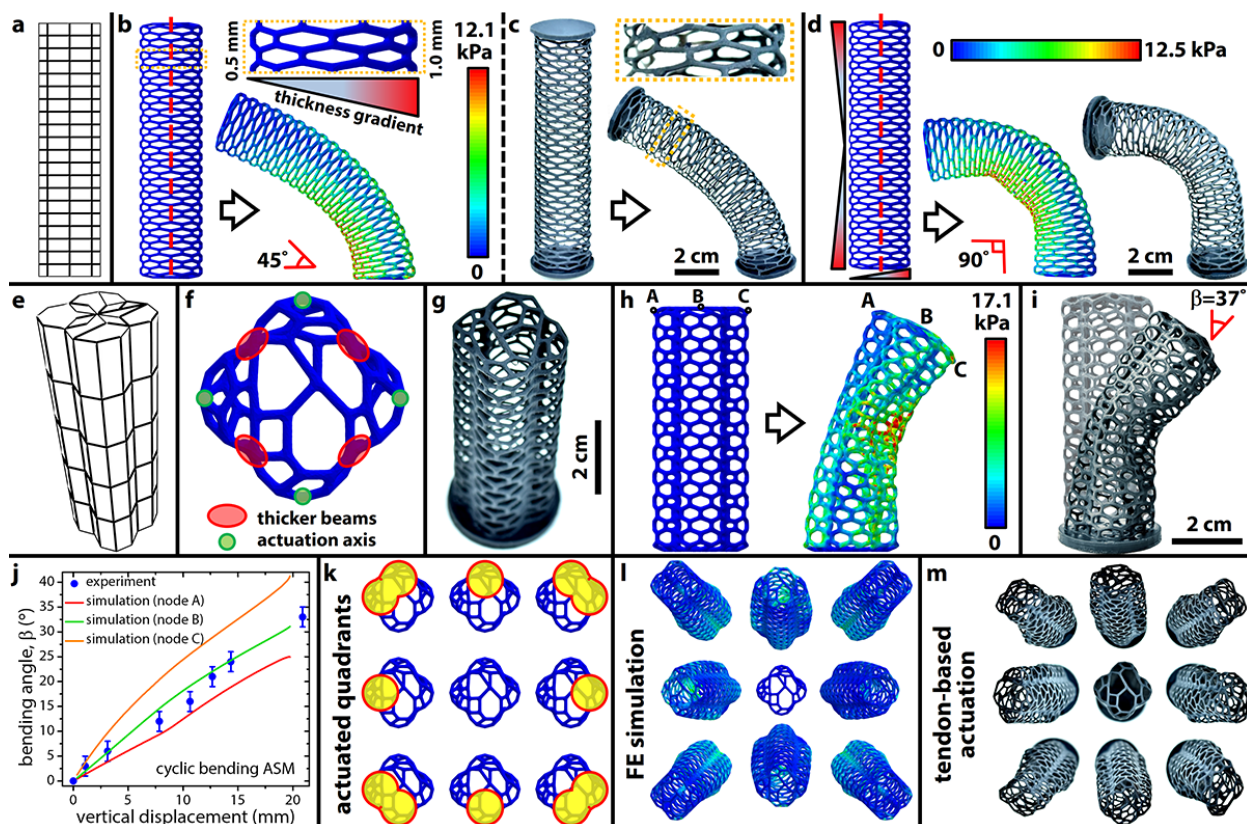


Figure 4.9. Programming motion of ASMs by tuning beam thickness. (a) Initial rectangular lattice used to design a bending actuator. (b) FEM simulation showing the stress distribution in an ASM with a gradient in the thickness of its beams (linearly increasing from 0.5 mm to 1 mm) perpendicular to the long axis of the structure. The bending axis is shown by a red dashed line. (c) Experimental realization of the ASM depicted in (b). (d) FEM simulation and experimental demonstration of an ASM with two gradients in the thickness of its beams to subtend a bending angle of 90° . (e) Initial lattice used to design an ASM capable of cyclic multi-directional bending. The lattice shown in (a) is replicated four times and joined. (f) Top view of the cyclic bending ASM highlighting the regions with thicker beams and the locations of the tendon-based actuation axes. (g) 3D printed cyclic bending ASM. (h) FEM simulation showing the stress distribution in the cyclic bending ASM upon actuation of one of its quadrants. (i) Experimental tendon-based actuation of the cyclic bending ASM showing a maximum bending angle $\beta = 37^\circ$. (j) Dependence of β on the vertical displacement due to compression at the three nodes A, B, C shown in (h). Experimentally measured values are for node B. (k) Top view of the cyclic bending ASM showing how rotary motion may be obtained by sequentially actuating different quadrants or combination of quadrants. (l) FEM simulation showing how the cyclic bending ASM responds when the different quadrants shown in (k) are actuated. (m) Experimental rotary motion obtained by the sequential tendon-based actuation of different quadrants (or combination of quadrants) of the ASM.

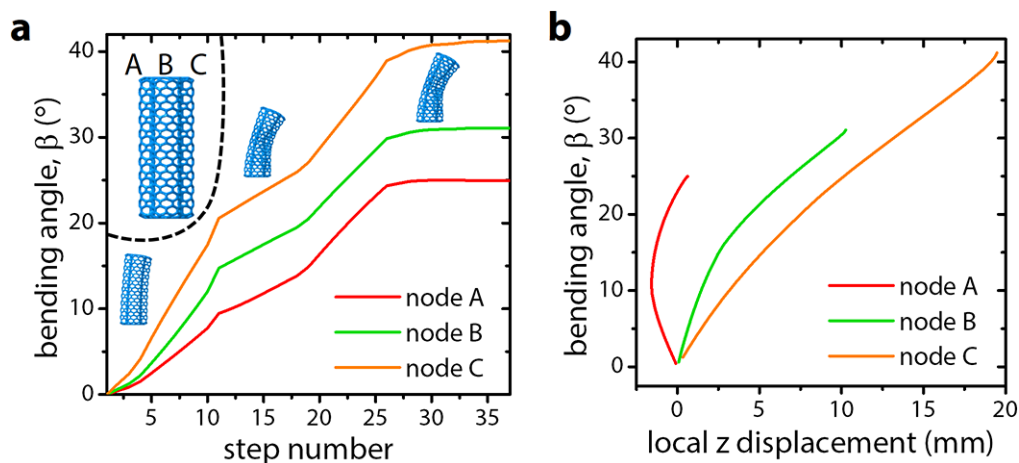


Figure 4.10. Simulated bending angle of the cyclic bending ASM. (a) Dependence of the bending angle β as a function of the FEM simulation step for three nodes (A , B , C ; shown in the inset). The simulations show the actuation of the quadrant containing node C . The sharp changes to the slopes of the curves indicate spontaneous buckling. (b) Dependence of β for the three nodes as a function of their local z displacement. Note that when the quadrant containing node C is actuated, the initial bending of the ASM forces node A to have a negative z displacement.

ASM, we use a primitive cylindrical lattice (Figure 4.3a, 4.9a), replicate it four times, and join it as shown in Figure 4.9e. We then increase the beam thickness of the resulting Voronoi structure locally in the four regions where the initial cylinders overlapped (Figure 4.9f), to get our final cyclic motion ASM (Figure 4.9g). This ASM has four quadrants, which can be independently actuated by individual tendons (Figure 4.9f). On actuation, the ASM bends towards the actuated quadrant due to the buckling of its thinner beams (Figure 4.9h, i). Through simulations and experiments, the bending angle (β) can be predicted and calibrated against the vertical displacement of the actuating tendon (Figure 4.9j, 4.10). Rotary motion is achieved by the sequential actuation of adjacent quadrants and pairs of quadrants (Figure 4.9k–m). Note that the rapid design approach of simply joining primitive shapes might produce ASMs with asymmetric top and bottom surfaces (Figure 4.9f). This asymmetry, however, is a negligible edge effect that does not compromise the symmetry of the rotary motion of the ASM—as demonstrated by simulations (Figure 4.9l) and experiments (Figure 4.9m).

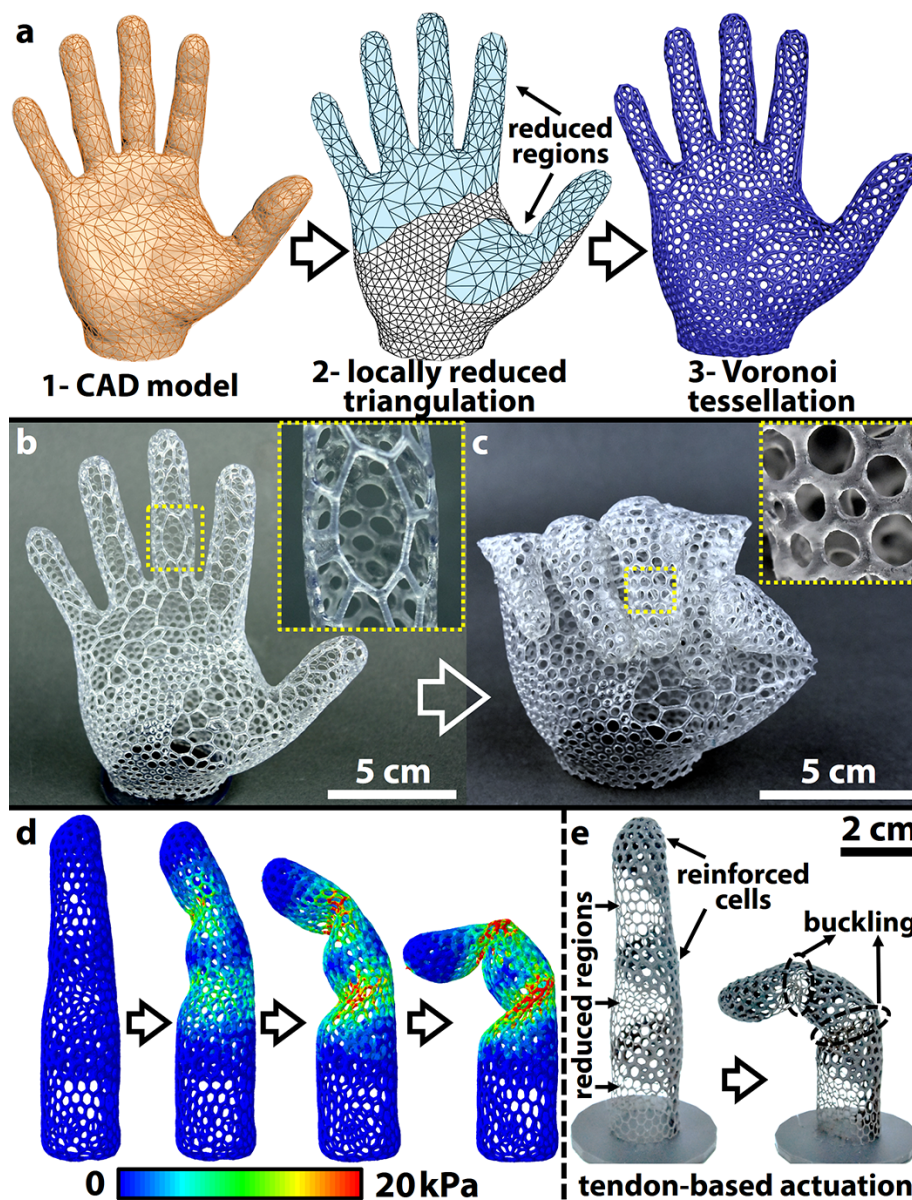


Figure 4.11. Programming motion in ASMs by locally tuning Voronoi cell size. (a) Starting with an existing CAD model of a hand, the Delaunay triangulation is made sparser over the highlighted areas of its topology, to ensure larger Voronoi cells in those regions. (b) Fabricated ASM hand. Inset shows how larger Voronoi cells are used in front while smaller cells are kept at the back of each finger, enabling their bending. (c) Actuated ASM hand with all fingers closed. Inset shows a zoom-in of the smaller Voronoi cells at the back of a finger. (d) FEM simulation showing the stress distribution in an ASM finger. Localized buckling of the two joints is encoded by tuning both cell size and beam thickness. (e) 3D printed ASM finger showing the regions with larger cells (thin beams) and smaller cells (thick beams). The buckling-induced motion is achieved by pulling a single tendon fastened at the tip of the finger.

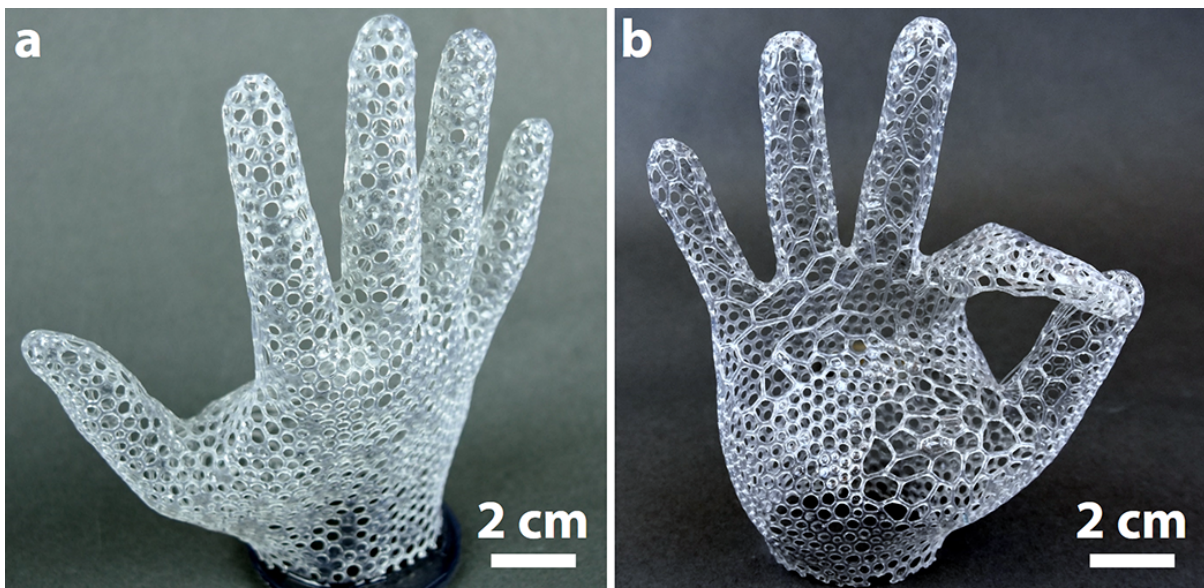


Figure 4.12. ASM hand fabricated by 3D printing. (a) Rear view of the ASM hand described in Figure 4.11, showing the smaller, uniformly distributed Voronoi cells. (b) ASM hand performing ‘OK’ gesture by simultaneously bending the index finger and thumb.

4.3.4 Topologically Encoding Motion by Locally Tuning Voronoi Cell Size

Most CAD tools allow the localized reduction of polygon count, decreasing the number of lattice points, in 3D models. When the Delaunay and Voronoi algorithms are applied to 3D models with non-uniform topological distributions of lattice points, the resulting architected materials will exhibit bigger Voronoi cells over the regions where the original lattice is sparse (Figure 4.11a). Tuning the cell density—number of Voronoi cells per unit area—of the resulting ASM enables the deliberate introduction of weak regions in its structure. Upon compression, the buckling of the ASM will concentrate on these weak regions making it possible to program the resulting motion of the ASMs by simply tuning the lattice density of the original CAD model.

We 3D printed a Voronoi-based soft robotic hand weighing 12.9 g (effective density = 0.094 g/cm^3 , 8.1% of bulk material; Figure 4.11b) actuated by five tendons tied to the tip of each finger and pulled through the center of the wrist. When the tendons inside the fingers are pulled, the bigger cells distributed over the palm side of the fingers accommodate the strain and induce their bending (Figure 4.11c). The fingers of this ASM can also be independently

actuated to perform different gestures (Figure 4.12). The judicious reduction of polygon count along the carpometacarpal joint enables the sequential flexion and abduction of the thumb upon compression and its adduction and extension when the force exerted by the tendon is released. The uniform distribution of small Voronoi cells over the back of this soft 3D-architected hand prevents the palm from collapsing on itself, even when all fingers are closed (Figure 4.11c). Multi-joint kinematics can be programmed in ASMs by distributing gradients of both beam thickness and cell size over their topology (Figure 4.11e). On tendon-based actuation, regions with larger Voronoi cells and thinner beams accumulate higher stresses (Figure 4.11d), localizing buckling and mimicking articular joints (Figure 4.11e).

4.3.5 Modular Approach to Build ASMs

The low density, easy-to-control actuation, and the adaptability to their environment through mechanical deformation provide ASMs with potential applications in devices that locomote/translate. Figure 4.13a–c shows the modular approach followed to design an architected soft robotic quadruped that crawls due to the combination of bending/twisting modules (legs) and compression modules (central body). The legs of this robot are independently actuated by one tendon (tied to the end of each leg). The four tendons operating the legs are pulled from a common Bowden cable placed in the center of the robot (Figure 4.13d–f). The beams of this Voronoi-based soft quadruped are designed so that the legs buckle first (Figure 4.13d) when they are pulled by the tendon, lifting the quadruped and transferring the strain to the central part of the robot, which then compresses and absorbs part of the localized deformation sustained by the leg (Figure 4.13e). We developed a basic crawling gait by simply pulling the tendons in sequence (Figure 4.13f), without requiring any asymmetric friction in the bottom side of the robot. Using this gait, we drove the robot at an average speed of 52.8 ± 6.6 m/h (~ 480 body lengths/h; 24% of body length/cycle; see Figure 4.15). The weight of this robot is 8.25 g (effective density = 0.153 g/cm³; 13.2% of bulk material) and that of the Bowden cable carried by the robot during crawling is 63 g.

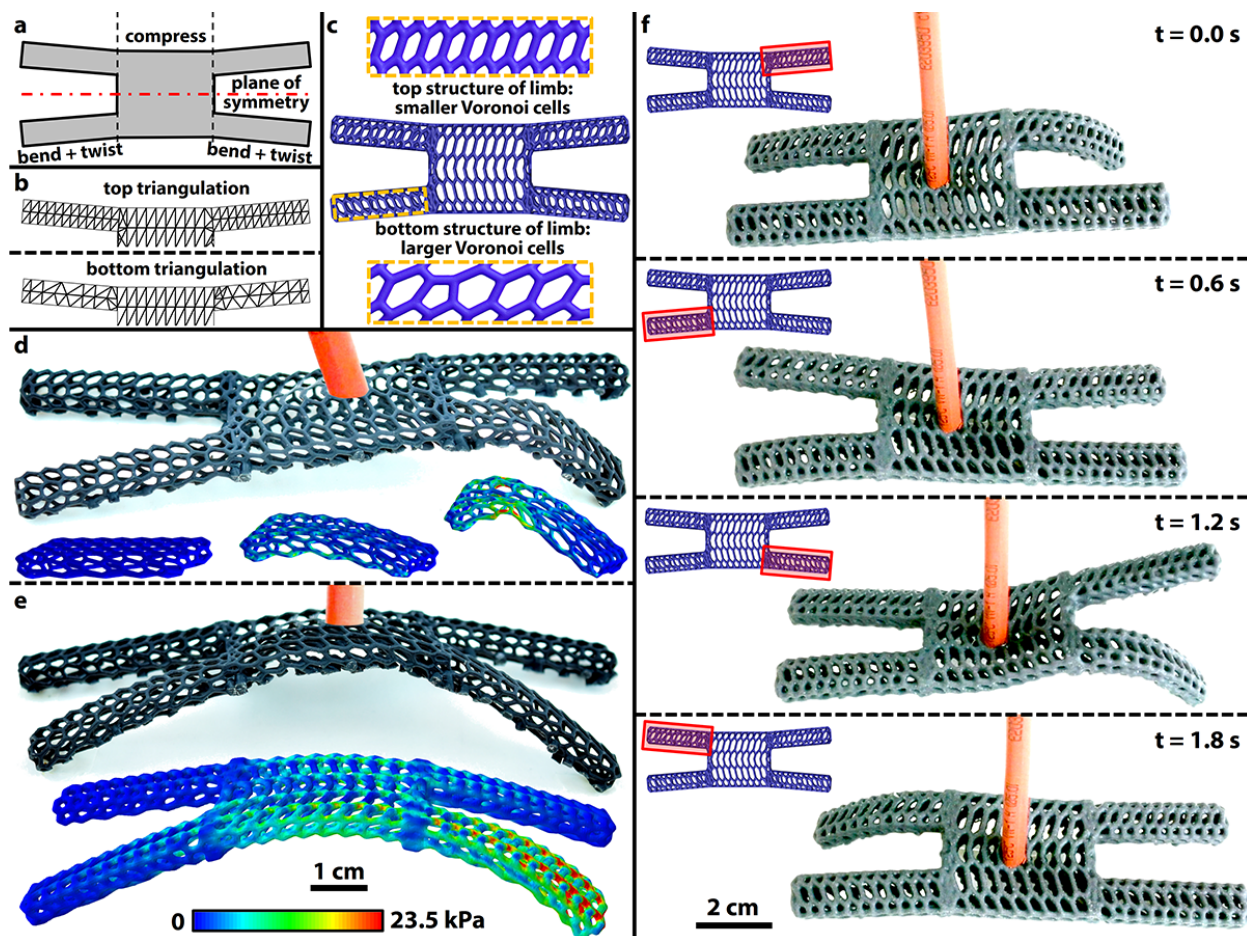


Figure 4.13. Modular design of ASMs—example of a quadruped. (a) Schematics showing the different modules comprising an ASM quadruped: the central body is made of two compression ASMs, while each of the four legs is a module that combines bending and twisting actuation. (b) Delaunay triangulations of the top and bottom surfaces of the ASM quadruped. While the central body has identical triangulations on the top and bottom, the bottom surface of the legs is designed with a sparser triangulation (also see Figure 4.14). (c) ASM quadruped, with insets showing the cell size differences between the top and bottom surfaces of each leg. (d) 3D printed ASM quadruped and FEM simulation showing the tendon-based actuation of one leg. Actuation is achieved by the localized deformation and buckling of beams. (e) The central body of the quadruped is lifted during the transition between the sequential actuation of two different legs. FEM simulation shows the stress distribution during this transition phase. (f) Snapshots showing a basic crawling gait. Insets indicate the leg actuated in each frame.

4.3.6 Highly Compressible and Stretchable Elastomeric ASMs

The design method presented in this study is compatible with the fabrication of ASMs out of elastomeric materials, which might currently be difficult to 3D print, by injection molding

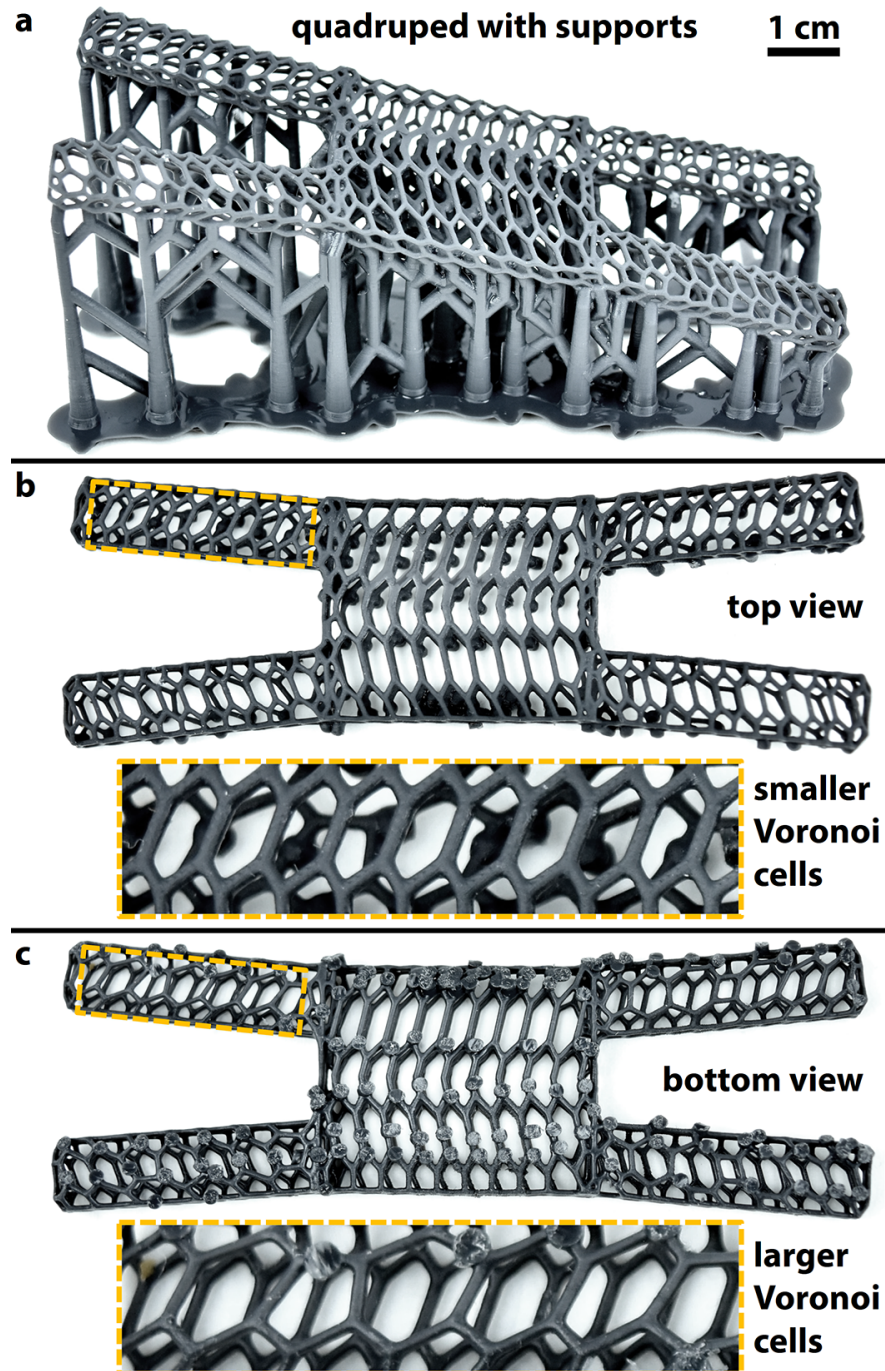


Figure 4.14. ASM quadruped fabricated by 3D printing. (a) Quadruped described in Figure 4.13, with support material. (b) Top view of the quadruped after the removal of its support material. Inset shows the smaller Voronoi cells on the top surface of each leg of the quadruped. (c) Bottom view of the quadruped. Inset shows the larger Voronoi cells on the bottom surface of each leg of the quadruped. The remnants of the support material on the bottom surface of the quadruped do not affect its motion.

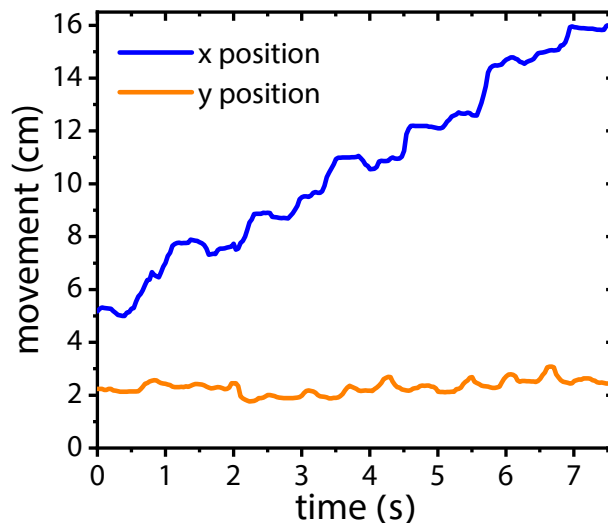


Figure 4.15. Kinematic analysis of a crawling ASM quadruped. We used MATLAB 2016a (Mathworks Inc.) Image Processing ToolboxTM to track the position of the center of mass (centroid) of the ASM quadruped. The x and y coordinates of the centroid of the ASM are plotted as a function of time.

using dissolvable molds. Figure 4.16a shows a hollow 3D printed acrylonitrile butadiene styrene (ABS) mold with two inlets used to inject the elastomeric premixture (Ecoflex00–30). After the elastomer cures inside the mold, we retrieved the fully elastomeric ASM by dissolving the mold in acetone.

Electrical components can be integrated into elastomeric ASMs to extend their functionality. We passed flexible conductive threads along the structure of the ASM and coated over them with a thin ($\sim 100 \mu\text{m}$) layer of elastomer to prevent delamination. Figure 4.16b shows an elastomeric Voronoi sphere with an integrated LED, conducting threads, and a battery (LED and battery are placed at opposite poles of the ASM). The topological architecture of this elastomeric structure enhances its stiffness and prevents its collapse due to its own weight, in contrast to the behavior of an unarchitected hollow sphere of the same dimensions. The low density of the ASM and the stretchability of the elastomer used in its fabrication facilitates ultrahigh reversible compression (up to 400%; Figure 4.16c) and extension (up to 500%; Figure 4.16d) without affecting the functioning of the integrated electronics. The embedded conductors are able to accommodate the ultrahigh stretching due to their low helix angle ($< 45^\circ$) spiral trajectory.¹⁵¹ These versatile design and fabrication strategies have the

potential to be useful in the development of stretchable electronic devices toward emerging applications.

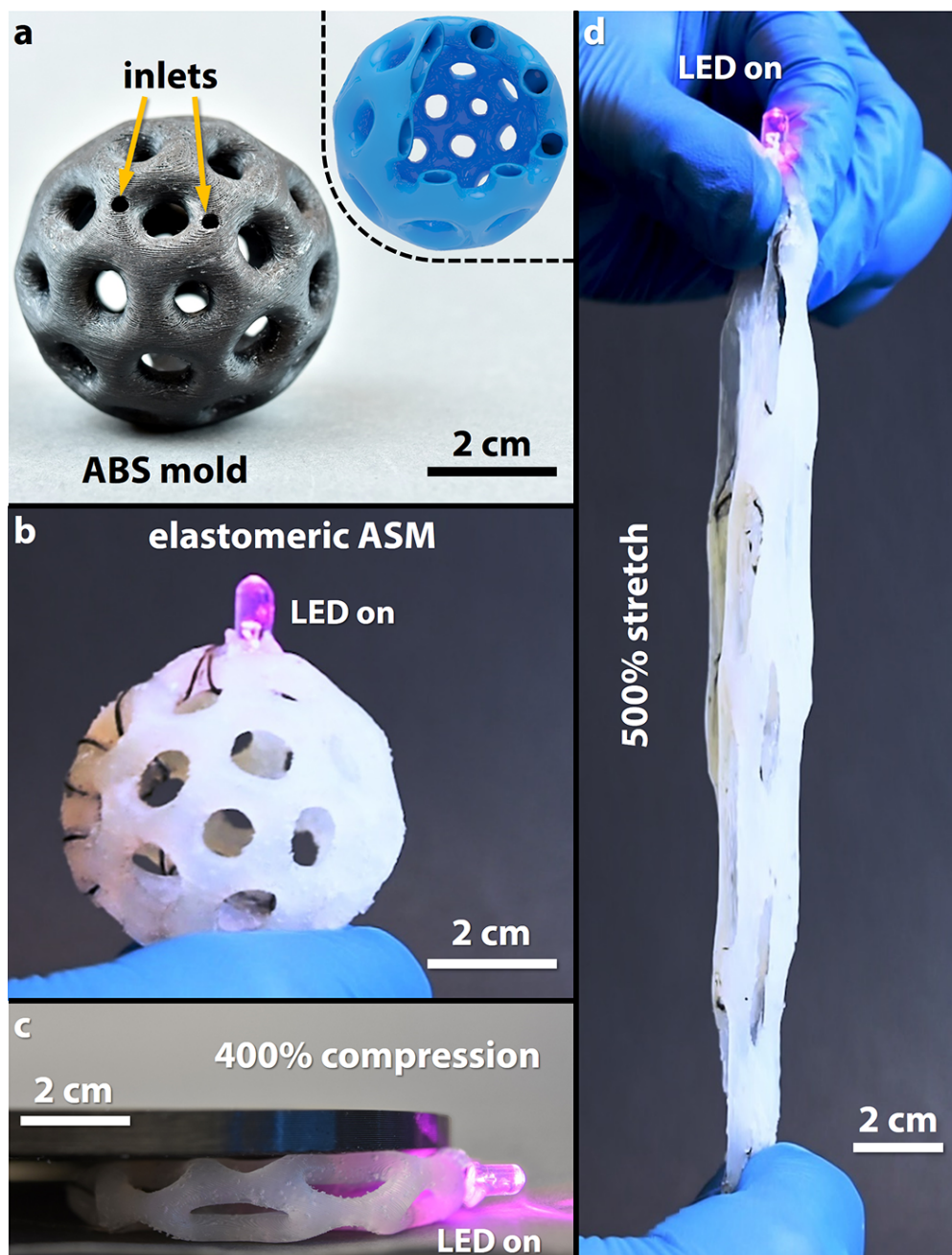


Figure 4.16. Highly deformable elastomeric ASMs with embedded electronics. (a) 3D printed ABS mold used to fabricate an elastomeric ASM by injection molding. Inset shows a quarter-section cut-away view with hollow internal channels. (b) Elastomeric ASM fabricated in Ecoflex 00-30. Two conductive threads (braided as a helical wire) and a small battery are embedded to power an LED. (c) Fabricated elastomeric ASM showing a reversible compressibility up to 400%. (d) Demonstration of reversible stretching as high as 500%.

4.4 Conclusion

In this chapter, we introduced ASMs: a new class of soft machines that benefit from their 3D-architected structure to expand the range of mechanical properties and behaviors achievable by 3D printed soft robots. We demonstrate that ASMs are simple to design, rapid to prototype, and can be actuated by integrating nylon threads serving as tendons. ASMs also have several significant advantages over other soft robotic systems. First, their architected structure confers them with effective densities as low as 8.1% of the bulk polymer, facilitating their use in lightweight robotic applications. Second, the resulting motion of the soft machine can be encoded in its topology either by applying thickness gradients to its flexible beams or by selectively enlarging some of its Voronoi cells. Having Voronoi cells only over the topology (i.e. surface) of the object further reduces the density of these ASMs, facilitates their tendon-based actuation, and minimizes the energy required to actuate them. Moreover, the anisotropic elasticity programmed on the architected structure of the ASMs enables continuum or localized actuation, to mimic both continuously deformable bodies and multi-joint systems. In addition, complex soft robotic motion—such as multi-finger gripping (Figure 4.1c, 4.11c) and quadrupedal locomotion (Figure 4.13f)—can be achieved by combining topologies that generate different actuations *via* a modular approach. Although most of the ASMs presented in this work were directly 3D printed, we have also shown that ASMs can be fabricated out of materials incompatible with 3D printing: by injection molding using dissolvable molds. This approach to build elastomeric ASMs facilitates the embedding of functional electronic components in soft robotic systems that can withstand ultrahigh compression (400%) and stretching (500%). ASMs, at their present level of development, also have two limitations: (i) They are tethered to the motors providing tendon-based actuation through a Bowden cable. Untethered actuation will require the inclusion of small motors, a battery, and a controller into the structure of the ASM. The hollow architecture of ASMs, however, leaves the interior of these soft robots available for housing actuation mechanisms and minimizes the friction with the tendons. (ii) The minimum beam thickness of ASMs (500 μm in this work) is limited by the resolution of the 3D printer used. Nevertheless, the design and fabrication strategy proposed to generate ASMs from conventional CAD models

is versatile and can be easily adopted by high resolution two-photon polymerization systems to fabricate ASMs at the micro- and nanoscale.¹⁵²

Recent progress in the development of multi-material¹⁵³ and functionally graded⁵⁴ 3D printing has paved the way toward 3D printable soft robots.⁸⁸ Unfortunately, the palette of materials compatible with 3D printing is limited and insufficient to fabricate soft robots with spatially textured mechanical metamaterial properties and functionality. ASMs expand the gamut of mechanical properties accessible, using one single material, to 3D printed or molded objects, enabling the fabrication of soft robots, actuators, and auxetic mechanical metamaterials with engineered elasticity. The design methods proposed in this work give general guidelines for users with minimal CAD experience to spatially encode high-level motion toward the development of more advanced applications in soft robotics, prosthetics, wearable devices, and stretchable electronics. We envision that the simplicity, low-cost, and modularity of this new class of soft machines, which can be fabricated by anybody with access to a conventional 3D printer, will lower barriers to entry for soft robotics.

4.5 Experimental Section

4.5.1 Rapid design of ASMs using Voronoi tessellation

We used 3ds Max 2018 (Autodesk Inc.) to design 3D CAD primitives—simple geometric shapes such as cylinders, spheres, or cuboids—and other complex 3D designs. The topological vertices of these CAD designs define the initial lattice points for the application of the Delaunay and Voronoi algorithms. Exporting the CAD designs as stereolithography (*.STL) files automatically performs a Delaunay triangulation on the 3D models. We then used Meshmixer 3.4 (Autodesk Inc.) to transform the triangulated models into low-density, 3D-architected designs using the Voronoi tessellation algorithm included in this free software. The application of these algorithms is fast (~ 1 s) and the thickness, geometry, and density of the beams integrating the final 3D-architected designs can be conveniently tuned.

4.5.2 3D printing ASMs

We used a high-resolution stereolithography (SLA) 3D printer (Form 2, Formlabs Inc.) to build ASMs using flexible photocurable polymers (FLGR01 and FLGR02, bulk density = 1.15 g/cm³; Formlabs Inc.). The gripper (Figure 4.1) and the quadruped (Figure 4.13) were printed with supports (only on the non-gripping exterior surface for the gripper, and only on the bottom exterior surface for the quadruped) due to their non-self-supported geometries. After 3D printing, the support material was removed by hand using predetermined breaking points (see Figure 4.2, 4.14). The remnants of the support material did not significantly affect the motion of the gripper or the quadruped since these remnants are akin to thin flexible flakes rather than rigid dimples. All other ASMs were printed directly on the printer's build platform without supports. For ASMs with beams thicker than 1 mm, we post-cured the structures in UV light ($\lambda = 405$ nm) at 60 °C for 15 min to avoid self-adhesion of beams due to surface tackiness.

4.5.3 Fabrication of elastomeric ASMs by injection molding

To fabricate ASMs using elastomeric materials that would be difficult to 3D print due to their relatively long curing times, such as Ecoflex 00–30, we used dissolvable hollow polymeric molds (Figure 4.16a). These hollow molds were 3D printed by fused deposition modeling (FDM; F170, Stratasys Ltd.) using ABS, with a proprietary water-soluble support material (F123 QSR; Stratasys Ltd.). The supports in the hollow internal channels were dissolved by sonicating in water. After letting the molds dry overnight at ambient conditions, we injected Ecoflex 00–30 premixture (1:1 w/w; Smooth on Inc.) inside the hollow channels of the mold and removed any trapped air bubbles by degassing in a desiccator at 36 Torr for 3 min. After curing the elastomer by baking the ensemble at 60 °C for 45 min, we dissolved the ABS mold by sonicating in acetone for 30 min—generating the final freestanding elastomeric ASM.

4.5.4 Actuation and control

We used small, high torque DC motors (9 g weight, 2.5 Kg 6 V, 60 RPM; Uxcell Inc.) to actuate ASMs by pulling from tendons made of low friction nylon cables (diameter = 0.25 mm). The tendons were manually tied to the beams of the ASMs, crossing multiple Voronoi cells (Figure 4.1c) to distribute the pressure induced by the tendon over several flexible beams. The DC motors providing tendon-based actuation are controlled using a programmable open-source microcontroller (UNO; Arduino Inc.).

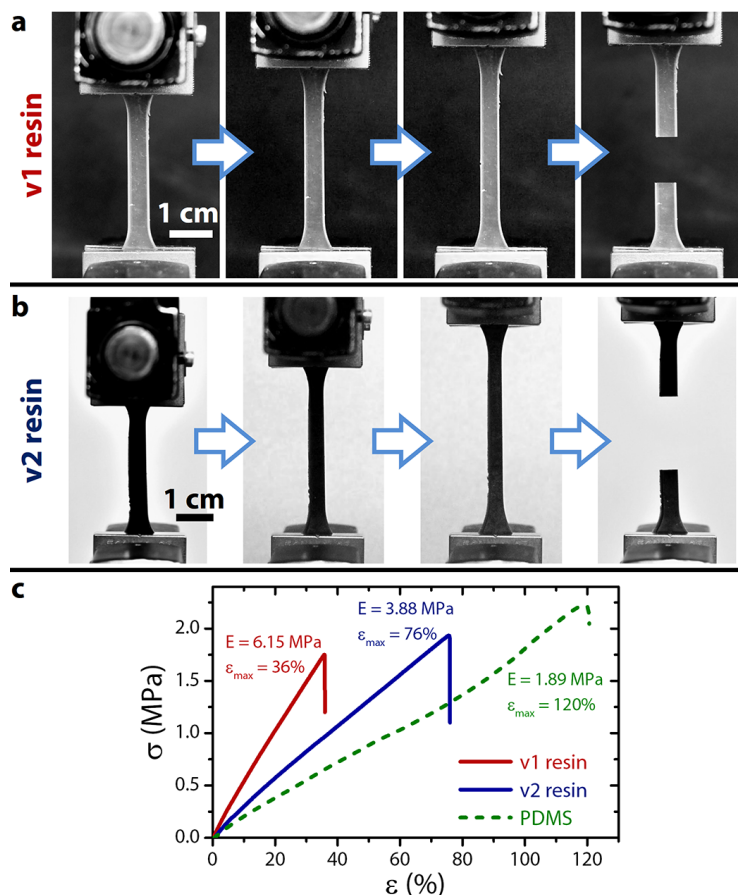


Figure 4.17. Mechanical characterization of flexible photopolymers used to 3D print ASMs. Tensile testing of ASTM D412-C dogbone specimens 3D printed from (a) Formlabs v1 flexible resin (FLGR01), and (b) Formlabs v2 flexible resin (FLGR02). (c) Representative engineering stress-strain curves for the specimens. v1 specimens have a Young's modulus $E = 6.15 \pm 0.046$ MPa and an ultimate tensile strain of $\sim 36\%$. v2 specimens have a Young's modulus $E = 3.88 \pm 0.06$ MPa and break at a strain of $\sim 76\%$. Both types of specimens have approximately the same ultimate tensile strength (~ 1.8 MPa). The stress-strain curve for polydimethylsiloxane (PDMS) is shown for comparison.

4.5.5 Mechanical characterization

We performed tensile testing of dogbone-shaped 3D printed specimens of the flexible photopolymers used to fabricate the ASMs to determine their bulk mechanical properties for subsequent use in finite element simulations. The samples were held in a universal testing machine (MTS Insight 10; MTS Systems Corp.) equipped with a 1 kN load cell (model 661.18.F01) and pulled at a loading rate of 0.083 mm/s (5 mm/min). This tensile test induces a strain rate of $2.77 \times 10^{-3} \text{ s}^{-1}$ (0.167 min^{-1}) for a gage length of 30 mm. All samples had a width of 4.5 mm and a thickness of 2.54 mm at the gage section, with a geometry consistent with ASTM D412–C specifications. These dimensions yield a surface-area-to-volume-ratio of $\sim 1.3 \text{ mm}^2/\text{mm}^3$. The load extension data recorded by the universal testing machine was converted to engineering stress-strain curves (Figure 4.17), which were used to determine Ogden model¹⁵⁴ parameters for finite element simulations.

We also performed uniaxial compression tests of a compression ASM (Figure 4.3a–c) and a solid cylinder (height = 25.4 mm, diameter = 12.7 mm), both 3D printed with FLGR02 resin, to quantitatively compare the nominal stress-strain characteristics of a representative ASM with that of the bulk photopolymer (Figure 4.5).

4.5.6 Finite element simulations

We performed finite element method (FEM) simulations to model the deformation of the ASMs upon tendon-based actuation and to evaluate the stress distribution along their structure. Voronoi tessellated models generated in Meshmixer were passed through a finite element pre-processor, HyperMesh 2017 (Altair Engineering Inc.), to optimize the meshing and reduce computing time. While several constitutive hyperelastic models exist for modeling the behavior of elastomers,¹⁵⁵ we found that the bulk stress-strain behavior of the 3D printed photopolymers (obtained from the tensile tests described above) are accurately described by a 3-term Ogden model¹⁵⁴ with the following parameters: $\mu_1 = 0.024361 \text{ MPa}$, $\mu_2 = 6.6703 \times 10^{-5} \text{ MPa}$, $\mu_3 = 4.5381 \times 10^{-4} \text{ MPa}$, $\alpha_1 = 1.7138$, $\alpha_2 = 7.0679$, $\alpha_3 = -3.3659$, $D_1 = 3.2587 \text{ MPa}^{-1}$, $D_2 = D_3 = 0$.

CHAPTER 5. MECHANICAL METAMATERIALS WITH PROGRAMMABLE COMPRESSION–TWIST COUPLING

5.1 Introduction

This chapter presents a rational, algorithmic design strategy to create mechanical-frustration- and size-effect-free Twisting Mechanical Metamaterials (TMMs), a new class of soft machines whose compression-twist coupling is encoded in their topological architecture. Elaborating a catalog of ~ 800 TMMs, we demonstrate, through experiments and finite element analysis (FEA), that both the twisting response and the Poisson’s ratio of TMMs can be programmed by simply tuning two design parameters. TMMs exploit snap-through instabilities to provide the first demonstration of a non-reciprocal “bidirectional” twisting behavior—one in which the direction of rotation reverses midway through an actuation cycle without modifying the input. We expect the ease of design, material-independent twisting response, and the cellular and global scalability of TMMs to herald the next generation of programmable matter.

5.2 Results

5.2.1 Design, Fabrication, and Characterization of TMMs

TMMs can be rapidly designed using an automated, parametric generative algorithm which converts any 2D rectangular lattice of points into the final 3D metamaterial structure (Figure 5.1a–c). This algorithm performs the following sequence of operations: 1) applies diagrid and Voronoi tessellations¹⁴⁶ to the initial rectangular lattice (Figure 5.1a); 2) shears the Voronoi tessellation to a planar curve angle (α_{2D}) based on the specified curve distance (α_d ; Figure 5.1b); 3) selects an $n \times m$ array of Voronoi cells from the center of the sheared

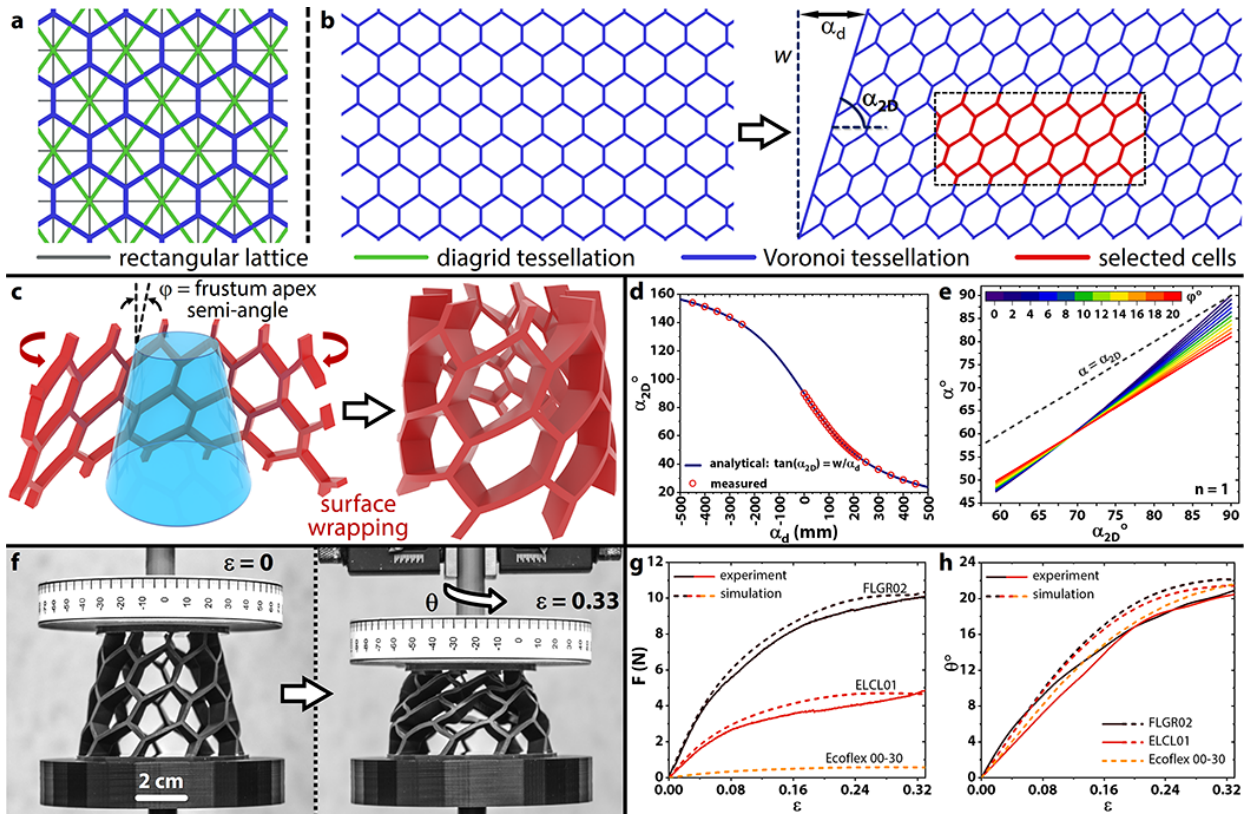


Figure 5.1. Design, fabrication, and characterization of TMMs. (a–c) Automated design algorithm used to create TMMs: (a) A 2D rectangular lattice (gray) is sequentially transformed into its diagrid (green) and Voronoi tessellation (blue). (b) The 2D Voronoi tessellation is sheared to a planar curve angle α_{2D} . An array of Voronoi cells from the center of this sheared tessellation is selected (red) according to the final desired structure of the TMM. (c) The selected sheared Voronoi cells are extruded normal to their plane and wrapped around the surface of a frustum with apex semi-angle φ , generating the final TMM. (d) Dependence of the planar curve angle α_{2D} on the curve distance α_d . (e) Dependence of the 3D curve angle α on the planar curve angle α_{2D} for φ ranging 0–20°. (f) Experimental characterization of the TMM shown in (c), 3D printed with FLGR02: a free-to-rotate protractor disk (graduated with angular measurements) applies a nominal compressive strain $\varepsilon = 0.33$ to the top surface of the TMM placed on a rigid platform. The TMM transforms the applied compressive load into a rotation (θ) of its top surface. (g) F – ε curves for the TMM design depicted in (c) and 3D printed with different materials, showing excellent agreement between finite element analysis (FEA) simulations and experimental characterization. (h) Dependence of the twisting angle θ on the nominal strain ε demonstrating that the compression-twist coupling is independent of the choice of material.

tessellation (Figure 5.2); 4) applies a finite thickness to the edges of the cells and extrudes them normal to their plane; and 5) wraps the extruded cells around the curved surface of a right-circular frustum with apex semi-angle φ , generating the final TMM (Figure 5.1c). The resulting TMM has n vertical levels of complete Voronoi cells and m Voronoi cells along the circumference on each level. By varying n (1–4), φ (0–20°), and α_d (0–500 mm), we generated a catalog of 781 TMMs (selected TMMs shown in Figures 5.3–5.6) to study their unconventional mechanical properties. Parametric choices outside these ranges cause mechanical frustration,^{70,156} leading to TMMs with intersecting or self-contacting beams. The planar curve angle (α_{2D}) depends on α_d as $\tan \alpha_{2D} = w/\alpha_d$, where w is the total width of the lattice plane (Figure 5.1b,d). Cell deformation due to wrapping around the curved surface of the frustum¹⁵⁷ causes the actual 3D curve angle (α) of a TMM cell (Figure 5.7) to deviate from α_{2D} (Figure 5.1e); this difference between α and α_{2D} becomes more pronounced as the cells get more sheared (lower α_{2D}), or as the number of levels (n) are increased (Figure 5.8).

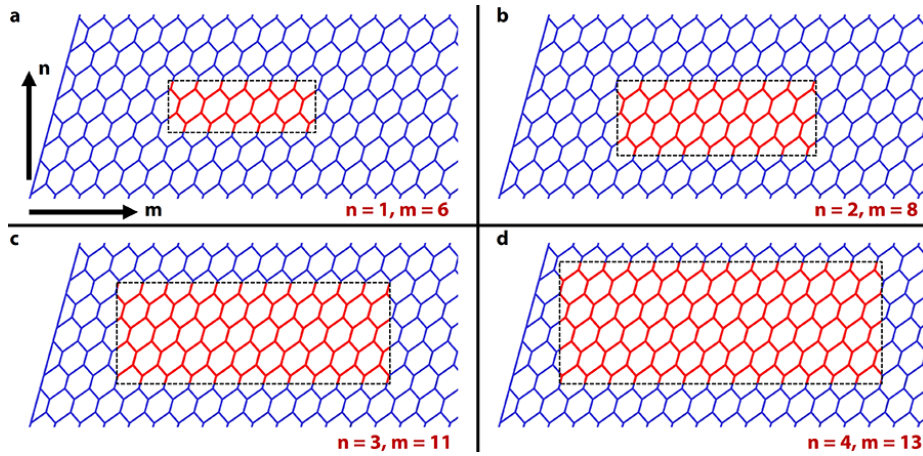


Figure 5.2. Illustration of TMM design parameters n (number of levels) and m (number of Voronoi cells on each level).

We built a customized experimental setup (Figure 5.9) to characterize the compression-twist coupling behavior of TMMs. Figure 5.1f shows a representative TMM ($n = 2$, $\varphi = 12.5^\circ$, $\alpha_d = 90$ mm) 3D printed with a flexible photopolymer being subjected to a normal compressive load. As the TMM is compressed, its top surface rotates by θ while its bottom surface is held fixed (Movie S1, see Appendix B). The rationally-designed architecture of

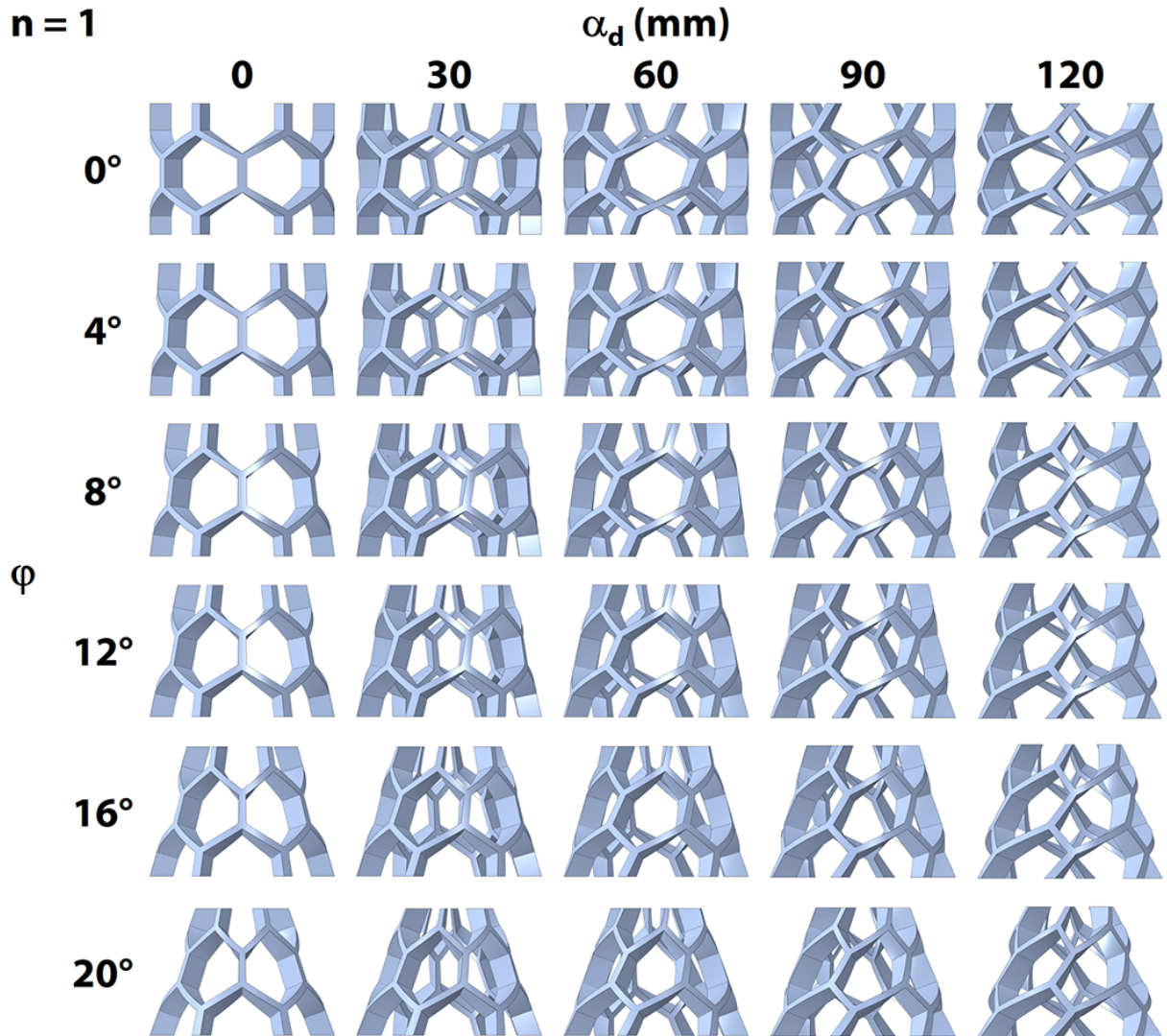


Figure 5.3. Selected TMM CAD models for $n = 1$: $\alpha_d \in \{0, 30, 60, 90, 120\}$ mm, $\varphi \in \{0, 4, 8, 12, 16, 20\}^\circ$.

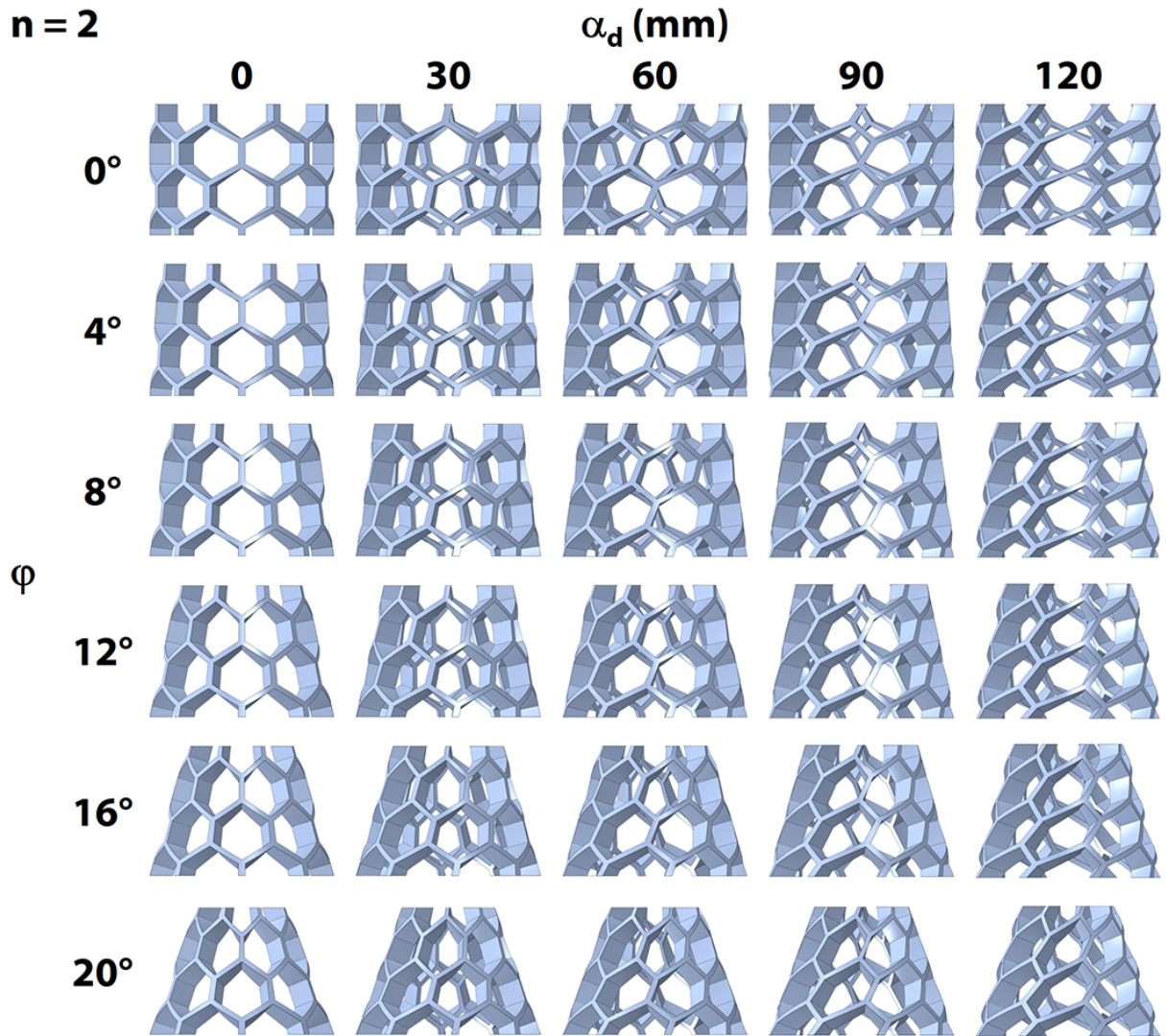


Figure 5.4. Selected TMM CAD models for $n = 2$: $\alpha_d \in \{0, 30, 60, 90, 120\}$ mm, $\varphi \in \{0, 4, 8, 12, 16, 20\}^\circ$.

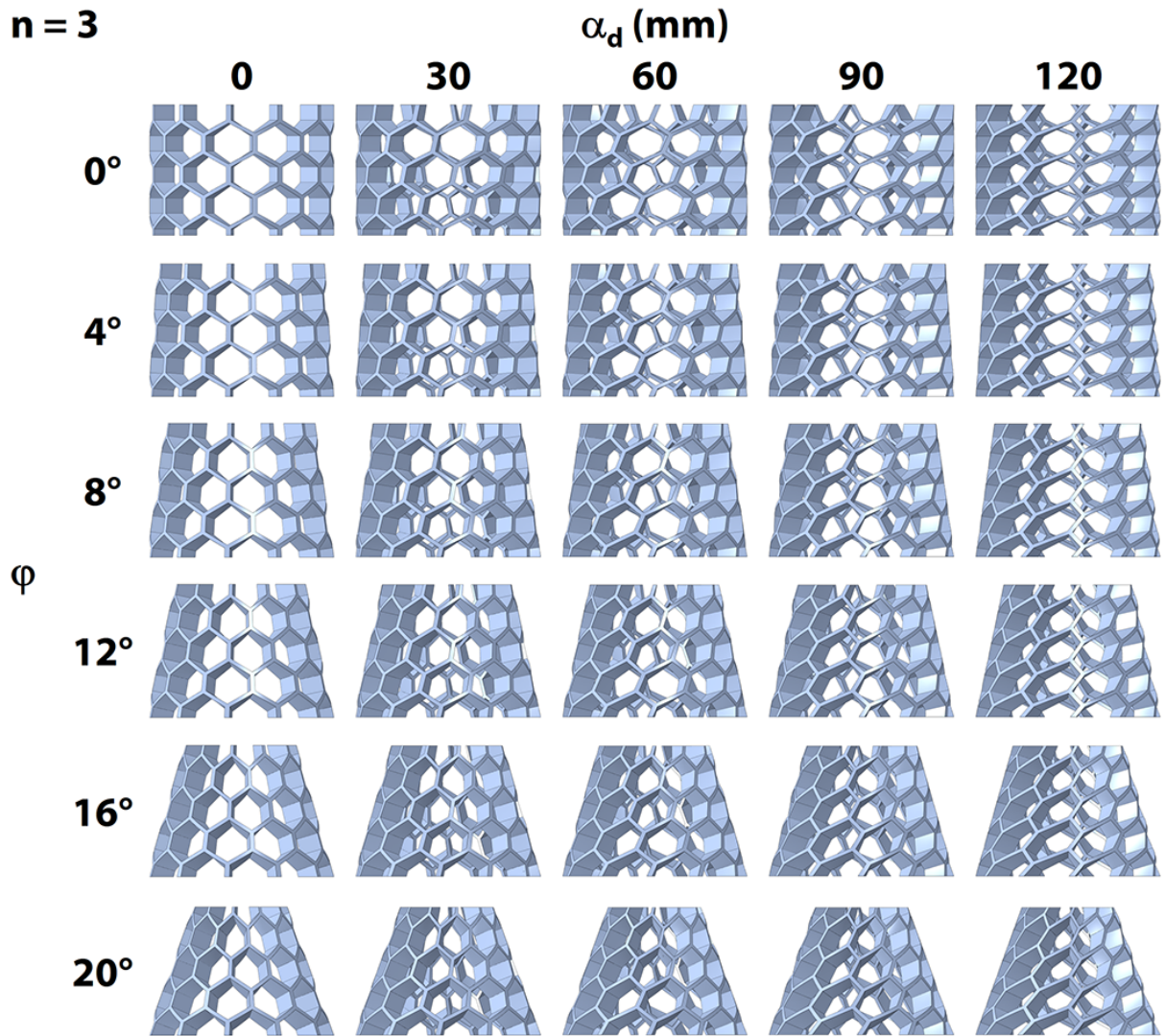


Figure 5.5. Selected TMM CAD models for $n = 3$: $\alpha_d \in \{0, 30, 60, 90, 120\}$ mm, $\varphi \in \{0, 4, 8, 12, 16, 20\}^\circ$.

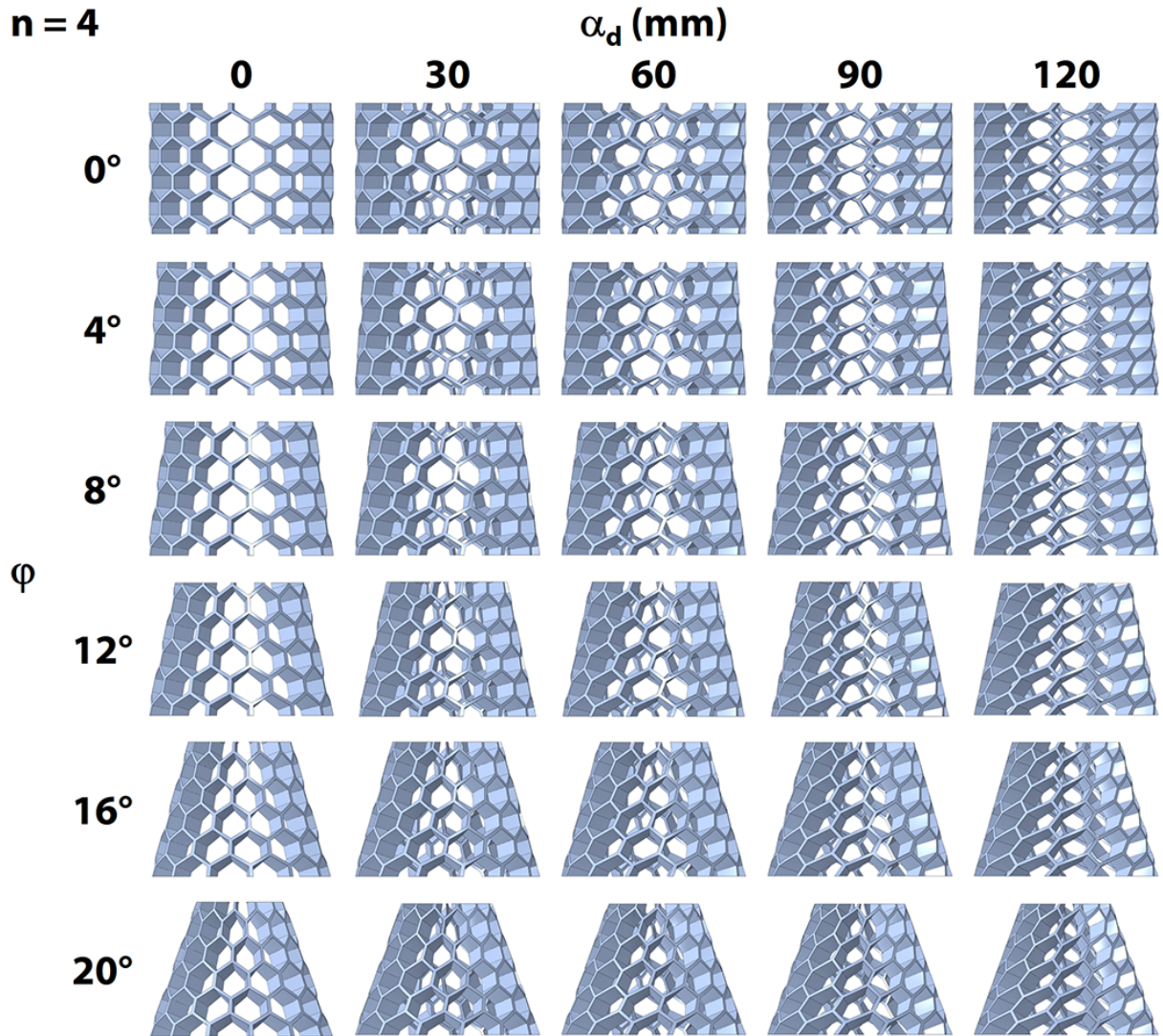


Figure 5.6. Selected TMM CAD models for $n = 4$: $\alpha_d \in \{0, 30, 60, 90, 120\}$ mm, $\varphi \in \{0, 4, 8, 12, 16, 20\}^\circ$.

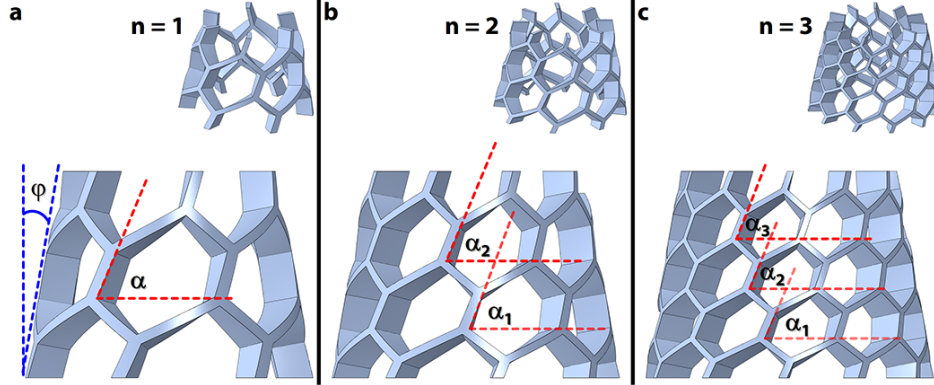


Figure 5.7. Illustration of the frustum apex semi-angle φ , and the 3D curve angle α . For multi-level TMMs ($n > 1$), α at each level is slightly different.

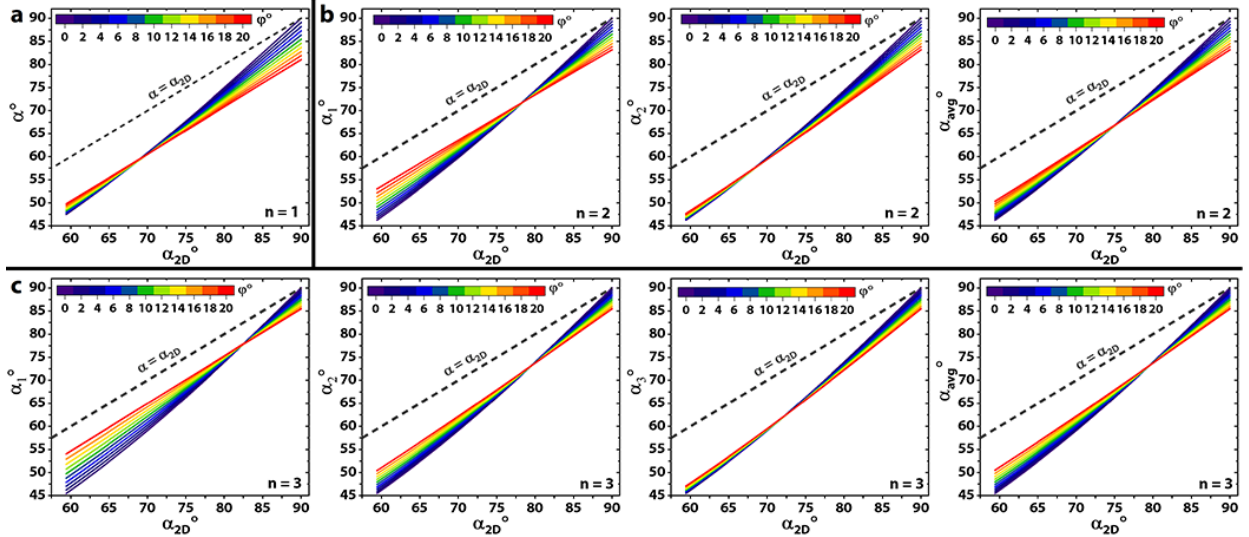


Figure 5.8. Dependence of the 3D curve angle α on the planar curve angle α_{2D} for φ ranging 0–20°. For multi-level TMMs ($n > 1$), $\alpha_{avg} = \frac{1}{n} \sum_{i=1}^n \alpha_i$.

TMMs endows them with compression-twist coupling, a property absent in isotropic materials.⁹³ This property manifests macroscopically ($\theta > 37^\circ$ with 33% compression) and is independent of the flexible material chosen to fabricate the TMM (Figure 5.1g,h; 5.10).

5.2.2 Rotation Regimes in TMMs

TMMs convert a compression applied to its top surface into a rotation of this surface, inducing a twist in their structure. The nature of this compression-twist coupling can be pro-

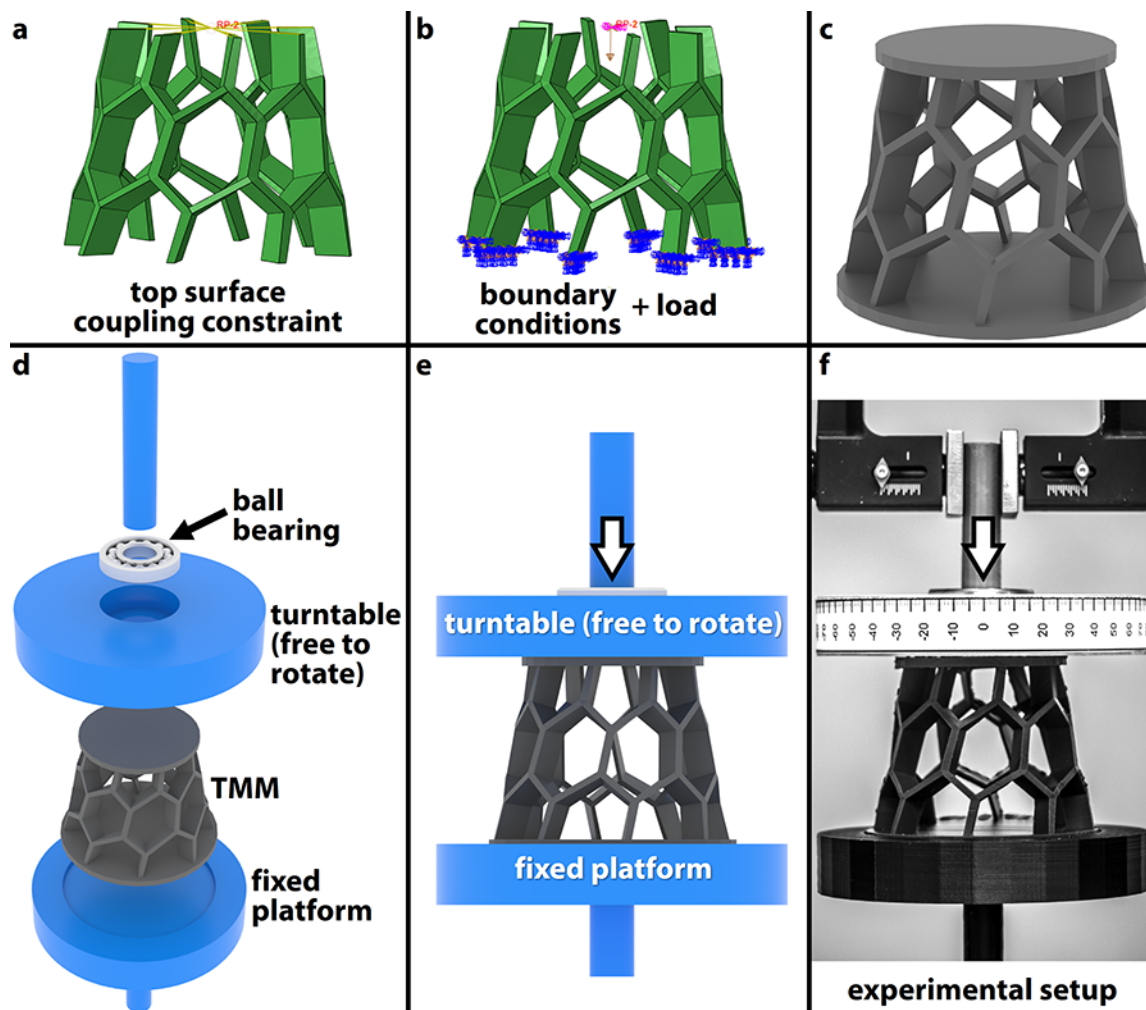


Figure 5.9. Setups for FEA simulation (a,b) and experimental characterization (c–f). (a) The terminal top surfaces of the beams of the TMM are coupled to a reference point. (b) All six degrees of freedom are constrained at the bottom surface of the TMM. The reference point is displaced vertically to compress (at 1 mm/s) the TMM by one-third its original height (up to $\varepsilon = 0.33$). (c) Two disks, 3D printed with the same photopolymer as the TMM, are bonded to the top and bottom surface of the TMM with cyanoacrylate adhesive (E-Z Bond; K&R International, Laguna Niguel, CA) to accurately realize the desired boundary conditions during mechanical characterization. (d–f) Custom-built fixture integrated in a universal testing machine setup to characterize the compression-twist coupling of the fabricated TMMs.

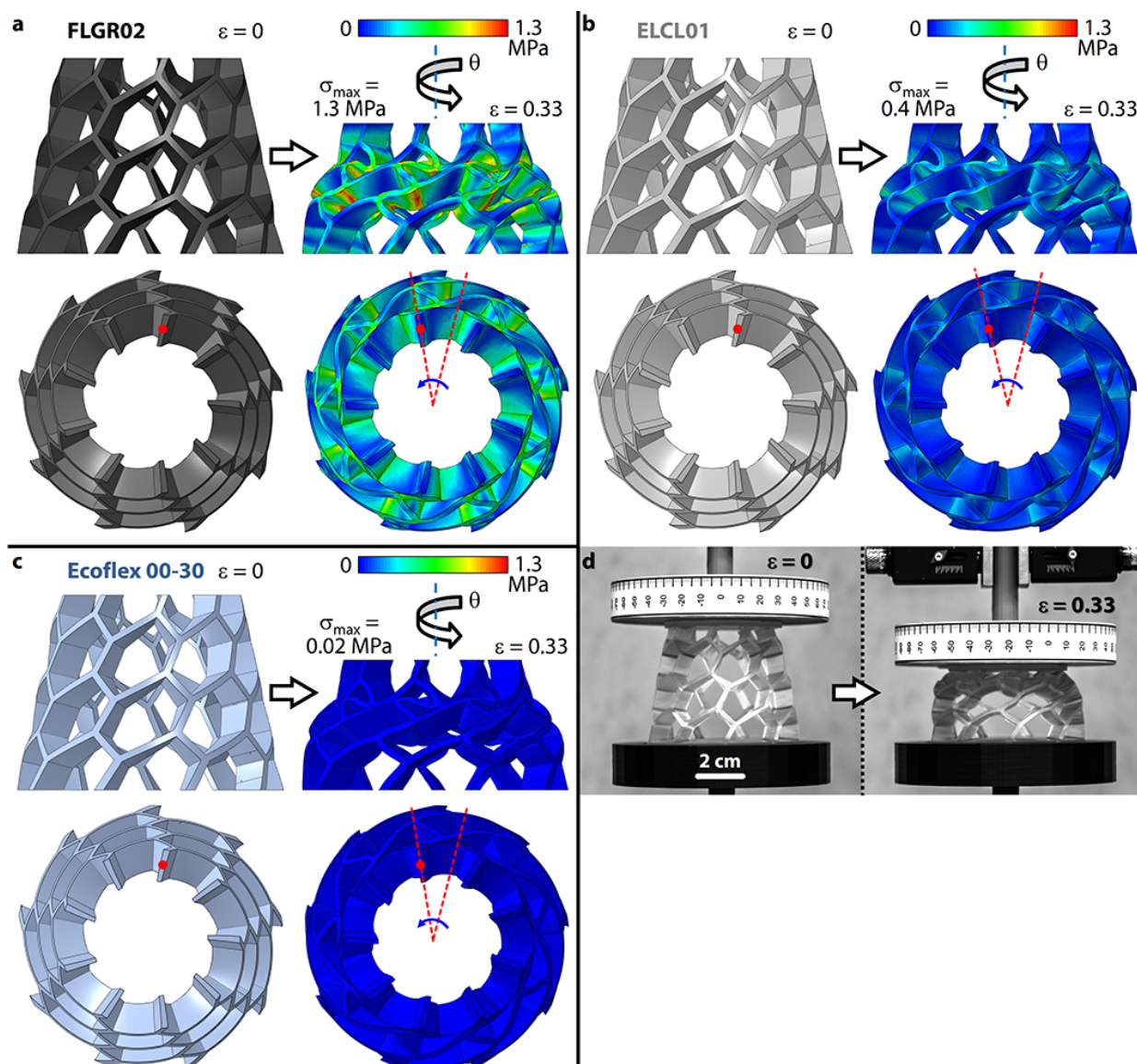


Figure 5.10. Comparison between TMMs fabricated out of different flexible materials. (a–c) FEA simulation snapshots showing the stress-distribution during compression in the same TMM structure fabricated out of three different materials—FLGR02 (a), ELCL01 (b), and Ecoflex 00-30 (c). While the stresses induced in the TMM are proportional to the stiffness of the bulk materials, the rotation angle is essentially independent of the material (also see Figure 5.1g,h). (d) Experimental characterization of the TMM shown in Figure 5.1c, 3D printed with ELCL01.

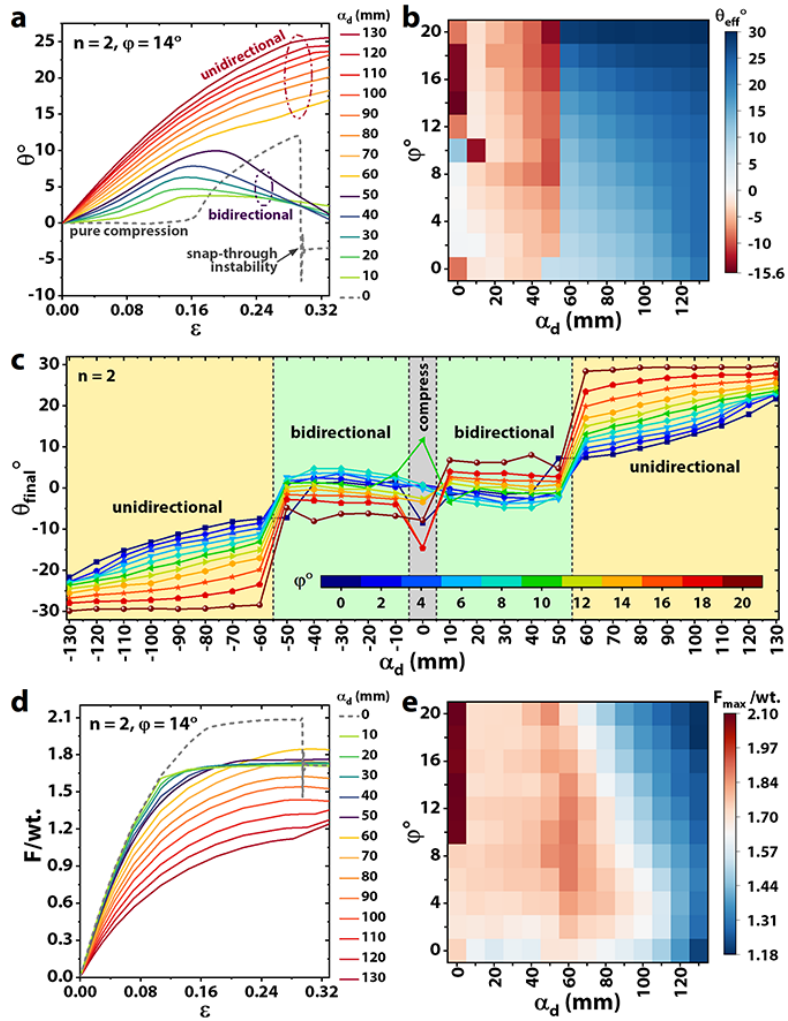


Figure 5.11. Rotation regimes in TMMs. (a) Dependence of the twisting angle θ on the nominal strain ϵ for $n = 2$, $\varphi = 14^\circ$, and α_d ranging 0–130 mm. The red/orange/yellow lines ($\alpha_d = 60$ –130 mm) denote the family of unidirectional TMMs; the blue/green lines ($\alpha_d = 10$ –50 mm) denote the family of bidirectional TMMs which reverse their direction of rotation at a critical strain $\epsilon = \epsilon_{\theta_{max}}(n, \varphi, \alpha_d)$; the gray dashed line ($\alpha_d = 0$) denotes a TMM which undergoes pure compression until its rapid buckling at $\epsilon = \epsilon_b(n, \varphi, 0)$, triggering a snap-through instability. (b) Heatmap of the effective twisting angle θ_{eff} for $n = 2$, φ ranging 0–20°, and α_d ranging 0–130 mm. Shades of blue ($\theta_{eff} > 0$) indicate unidirectional twisting, while shades of red ($\theta_{eff} < 0$) denote bidirectional twisting. (c) Twisting regimes for the family of TMMs with $n = 2$ obtained by varying α_d . (d) Weight-normalized F – ϵ curves for the family of TMMs in (a). (e) Heatmap of the weight-normalized maximum reaction force ($F_{max}/wt.$) for $n = 2$, φ ranging 0–20°, and α_d ranging 0–130 mm. The color scale varies uniformly from blue (low $F_{max}/wt.$) to red (high $F_{max}/wt.$).

grammed by simply tuning two design parameters, φ and α_d , giving access to three distinct regimes: unidirectional rotation, bidirectional rotation, and pure compression (Figure 5.11a–c). For a given φ , the family of “unidirectional TMMs” ($\alpha_d = 60\text{--}130\text{ mm}$) exhibit a rotation angle (θ) increasing monotonically with compressive strain ε (Movie S1, see Appendix B). In “bidirectional TMMs” ($0 < \alpha_d < 60\text{ mm}$), the direction of rotation α reverses at a critical strain ($\varepsilon = \varepsilon_{\theta_{max}}$; Figure 5.12), which depends on φ and α_d (Movie S2, see Appendix B). Finally, all TMMs with $\alpha_d = 0$ exhibit pure compression (i.e. no rotation) upon vertical deformation; however, for certain φ values “pure compression TMMs” exhibit a snap-through instability—a metastable segment in the force-strain curve in which large changes in strain require essentially no additional force⁵⁰—inducing the rotation of the TMM beyond $\varepsilon > \varepsilon_b$ (Figure 5.11d; 5.13). Improved stability of the pure compression behavior can be achieved by reducing the aspect ratio of the Voronoi cells during the design of the TMM.^{146,158}

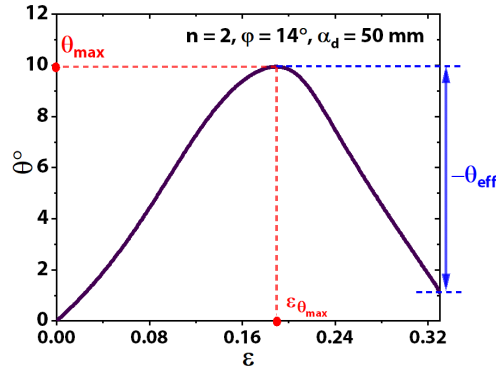


Figure 5.12. Illustration of the critical strain $\varepsilon_{\theta_{max}}$ at which the direction of rotation reverses for bidirectional TMMs, and the effective rotation angle (θ_{eff}) used to quantify the uni- or bidirectionality of TMMs.

To quantify the uni- or bidirectionality of a TMM, we define its effective rotation angle (θ_{eff}) as follows (Figure 5.12):

$$\theta_{eff} \equiv \begin{cases} \theta_{max} = \theta_{\varepsilon_{max}} & \text{for unidirectional TMMs} \\ \theta_{\varepsilon_{max}} - \theta_{max} & \text{for bidirectional TMMs} \end{cases},$$

We observe a sharp transition from unidirectional to bidirectional behavior near $\alpha_d = 60\text{ mm}$, irrespective of φ (Figure 5.11b,c). In their respective regimes, the magnitude of the

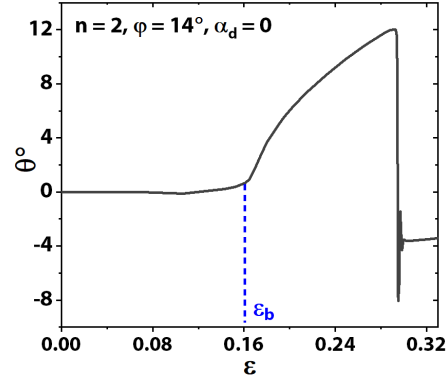


Figure 5.13. Illustration of the critical buckling strain ε_b , beyond which a snap-through instability is triggered.

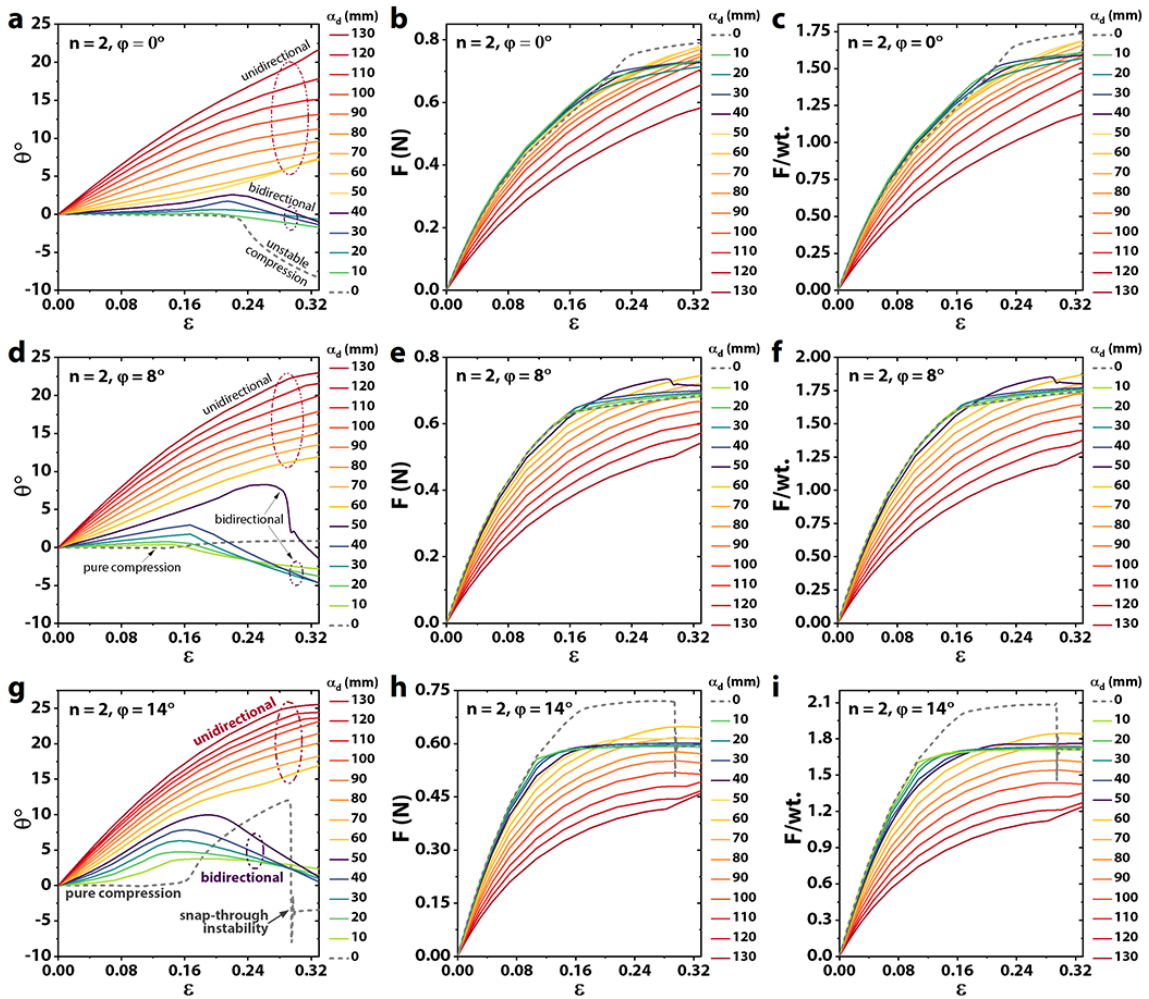


Figure 5.14. θ - ε , F - ε , and weight-normalized F - ε curves for families of TMMs with $n = 2$, $\alpha_d = 0$ -130 mm, and $\varphi = 0^\circ$ (a-c); $\varphi = 8^\circ$ (d-f); and $\varphi = 14^\circ$ (g-i).

uni- or bidirectionality increases with both α_d and φ (Figure 5.14). Note that all TMMs described in this study are chiral: if α_d is switched in sign while preserving its magnitude, the direction of induced rotation also switches while preserving its magnitude ($\theta_{-\alpha} = -\theta_{\alpha}$; Figure 5.11c; 5.15). TMMs with positive values of α_d initiate counterclockwise rotation (left-handed chirality), while TMMs with negative values of α_d initiate clockwise rotation (right-handed chirality). The force characteristics of two chiral counterparts are, however, indistinguishable ($F_{-\alpha} = F_{\alpha}$; Figure 5.15). Reaction forces produced by unidirectional TMMs monotonically increase with ε and decreasing α_d , while the reaction forces produced by bidirectional TMMs increase only until $\varepsilon_{\theta_{max}}$, where the onset of the snap-through instability switches the direction of rotation (Figure 5.11d; 5.14). Neglecting the mechanically unstable pure compression TMMs, the highest reaction forces (normalized by TMM weight; Figure 5.16) occur for TMMs with α_d at the transition between unidirectional and bidirectional behavior (Figure 5.11e; 5.17).

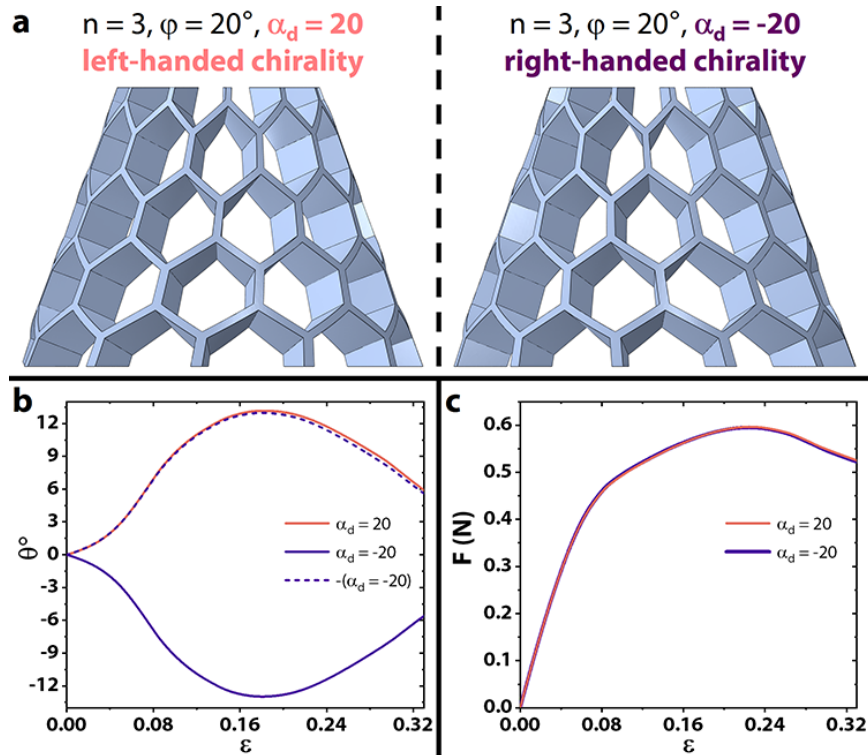


Figure 5.15. Chirality in TMMs. (a) CAD models showing the two chiral counterparts of a TMM with $n = 3$, $\varphi = 20^\circ$, and $\alpha_d = 20$ mm (left handed) or -20 mm (right handed). (b) Compression-twist coupling response of the TMMs shown in (a); $\theta_{\alpha_d=-20} = -\theta_{\alpha_d=20}$ (c) Force characteristics of the two chiral counterparts; $F_{\alpha_d=-20} = F_{\alpha_d=20}$.

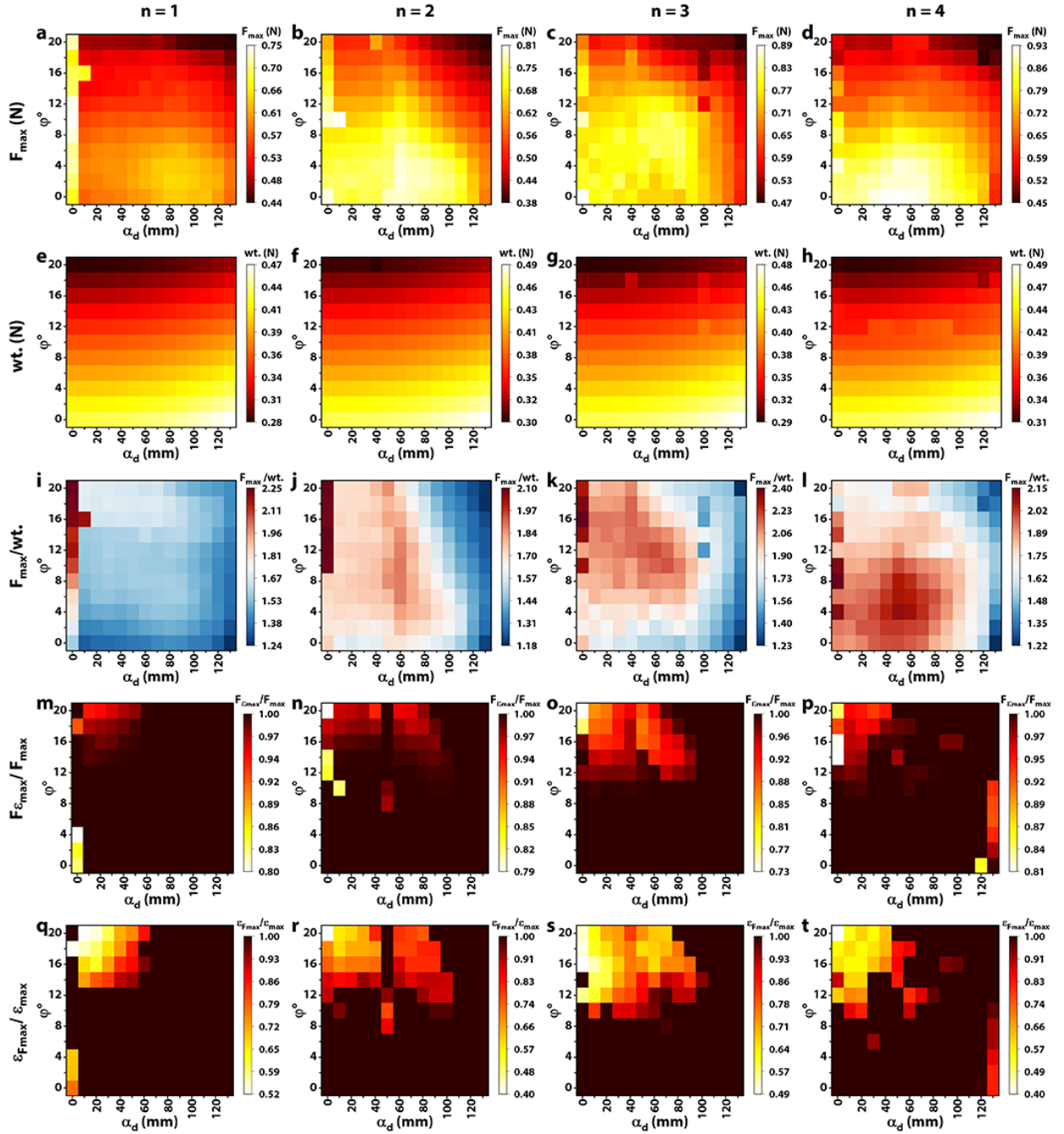


Figure 5.16. Heatmaps of (a–d) the maximum reaction force (F_{max}); (e–h) the weight of the TMMs; (i–l) the weight-normalized maximum reaction force ($F_{max}/wt.$); (m–p) reaction force at maximum compression ($F_{\epsilon_{max}}$; $\epsilon_{max} = 0.33$) expressed as a fraction of F_{max} ; (q–t) strain at which the reaction force is maximum, expressed as a fraction $\epsilon_{F_{max}}$, for $n = 1$ –4, ϕ ranging 0–20°, and α_d ranging 0–500 mm.

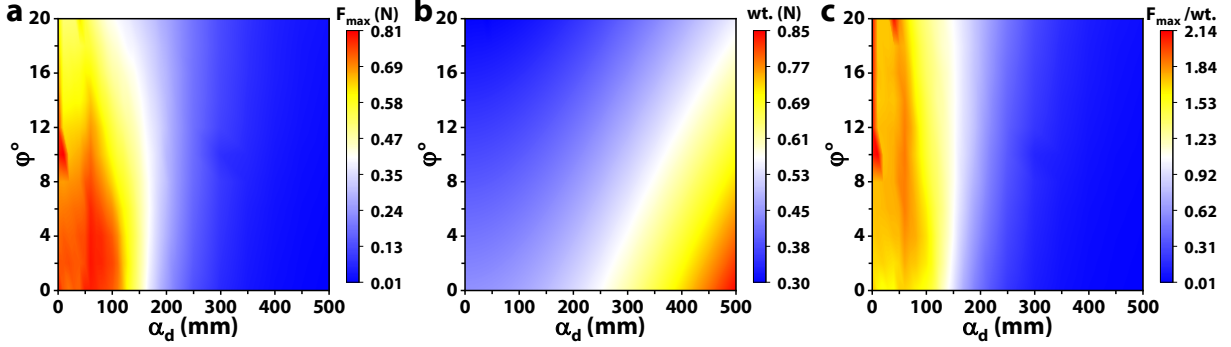


Figure 5.17. Contour plots of (a) the maximum reaction force (F_{max}); (b) the weight of the TMM; and (c) the weight-normalized maximum reaction force ($F_{max}/wt.$), for $n = 2$, φ ranging 0–20°, and α_d ranging 0–500 mm.

5.2.3 Compression–Twist Coupling Optimization

Having established the general dependence of the twisting behavior of TMMs on the design parameters α_d and φ , we now investigate what combination of (α_d, φ) maximizes the twisting response. Figure 5.18a shows a contour plot of θ_{final} (θ at $\varepsilon = 0.33$) varying as a function of φ and α_d . For unidirectional TMMs of a given φ , θ is maximized in the vicinity of $\alpha_d \approx 180$ mm (exact locus of $\theta_{max}|\varphi$ in Figure 5.19). Although θ increases monotonically with φ , TMMs with $\varphi > 20^\circ$ cannot be practically realized due to mechanical frustration. $\alpha_d = 180$ mm corresponds to $\alpha_{2D} = 50.7^\circ$, which, for $n = 2$, designates an α in the range $\sim 36\text{--}44^\circ$ (for $\varphi = 0\text{--}20^\circ$). Theoretically, $\alpha = 45^\circ$ is expected to maximize the unidirectional twisting response; however, the deformation of the Voronoi cells inflicted during the design step of wrapping the planar tessellation around the curved surface of a frustum (Figure 5.1c) causes the experimental results to deviate slightly.

The single most representative figure of merit to quantify the compression-twist coupling of TMMs is their twist per unit strain.⁹³ We calculated the maximum instantaneous unidirectional twist per unit strain ($d\theta/d\varepsilon$) to be $\sim 162^\circ$ ($1.62^\circ/\%$; see Figure 5.18b,c; 5.20). For $\varepsilon > 0.25$, the friction between the self-contacting beams of the TMM leads to a sudden angular retardation and a sharp drop in $d\theta/d\varepsilon$ (Figure 5.18c,d). The second derivative of the $\theta\text{--}\varepsilon$ curves (Figure 5.18d) is proportional to the angular acceleration and, consequently, to the torque produced in the TMMs. For unidirectional TMMs in the steady state (Figure 5.18d,

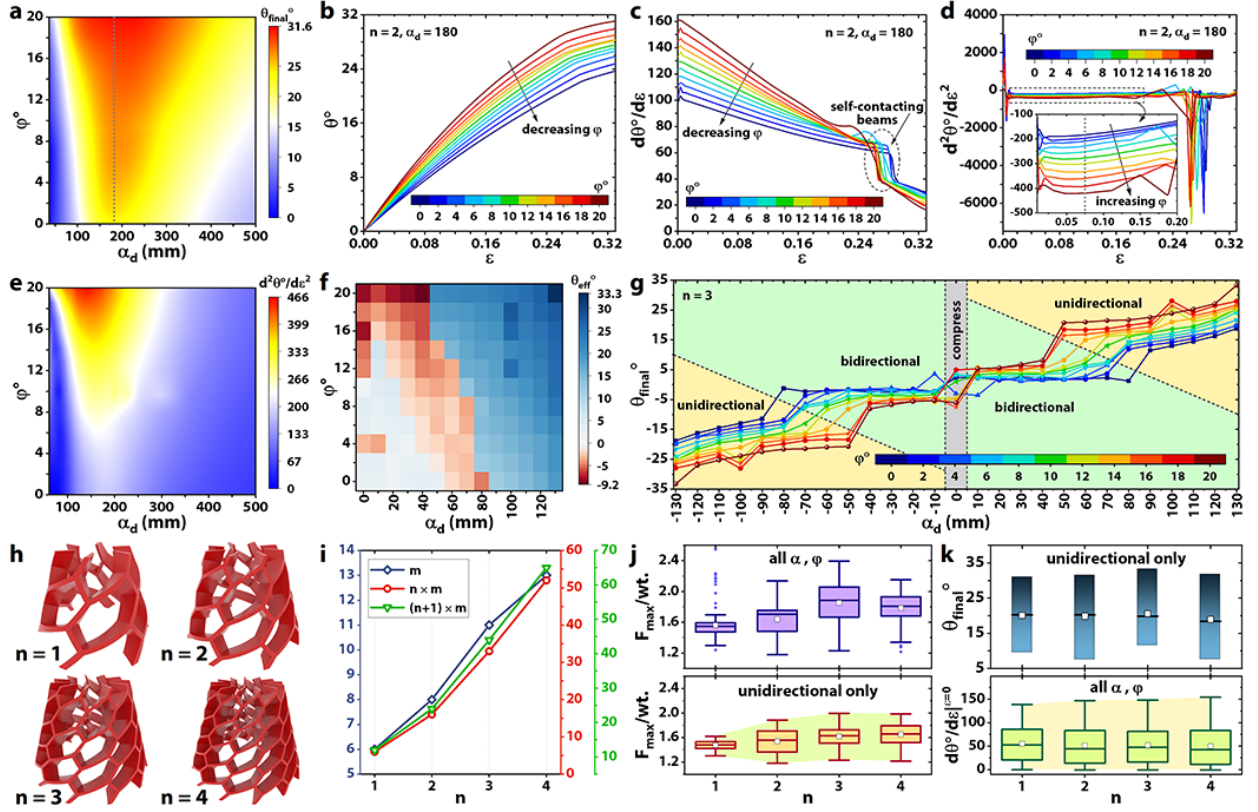


Figure 5.18. (a) Contour plot of θ_{final} ($\varepsilon_{max} = 0.33$) for $n = 2$, φ ranging 0–20°, and α_d ranging 40–500 mm. (b) Dependence of the twisting angle θ on the nominal strain ε for $n = 2$, $\alpha_d = 180$ mm, and φ ranging 0–20°. (c) Dependence of the instantaneous twist per unit strain $d\theta/d\varepsilon$ on the nominal strain ε for $n = 2$, $\alpha_d = 180$ mm, and φ ranging 0–20°. (d) Dependence of the normalized instantaneous angular acceleration $d^2\theta/d\varepsilon^2$ on the nominal strain ε for $n = 2$, $\alpha_d = 180$ mm, and φ ranging 0–20°. (e) Contour plot of the normalized instantaneous angular acceleration $d^2\theta/d\varepsilon^2$ for $n = 2$, φ ranging 0–20° and α_d ranging 60–500 mm (only unidirectional TMMs). (f) Heatmap of the effective twisting angle θ_{eff} for $n = 3$, φ ranging 0–20° and α_d ranging 0–130 mm. Shades of blue ($\theta_{eff} > 0$) indicate unidirectional twisting, while shades of red ($\theta_{eff} < 0$) denote bidirectional twisting. (g) Twisting regimes for the family of TMMs with $n = 3$. (h) 3D CAD models of representative TMMs ($\varphi = 18^\circ$, $\alpha_d = 130$ mm) with different levels ($n = 1, 2, 3, 4$). (i) Variation of m , $n \times m$, and $(n + 1) \times m$ as a function of the number of levels in the TMM (n), where m is the number of Voronoi cells in a single level along the perimeter, $n \times m$ is the number of complete Voronoi cells, and $(n + 1) \times m$ is the total number of Voronoi cells in the TMM. (j) Box-and-whiskers plot of the distributions of the normalized maximum reaction force ($F_{max}/wt.$) for $n = 1, 2, 3, 4$. Top: considering all α_d and φ for each n . Bottom: considering only unidirectional TMMs. (k) Top: Range of values of θ_{final} for each n , considering only unidirectional TMMs. Bottom: Box-and-whiskers plot of the distributions of the initial instantaneous twist per unit strain ($d\theta/d\varepsilon|_{\varepsilon=0}$), considering all α and φ for each n .

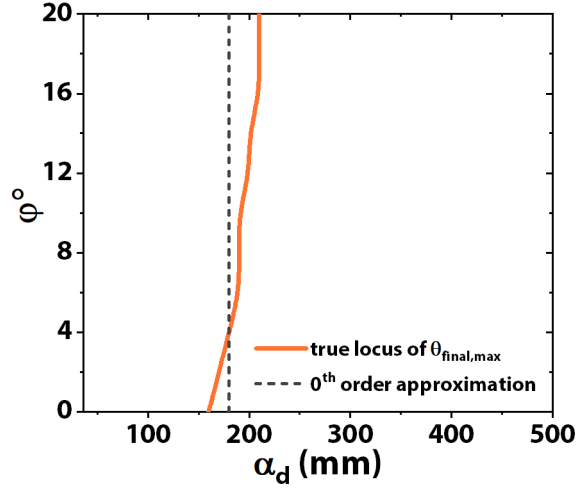


Figure 5.19. Exact locus (orange solid line) and its zeroth order approximation (gray dotted line) of $\theta_{final,max}|\varphi$ from Figure 5.18

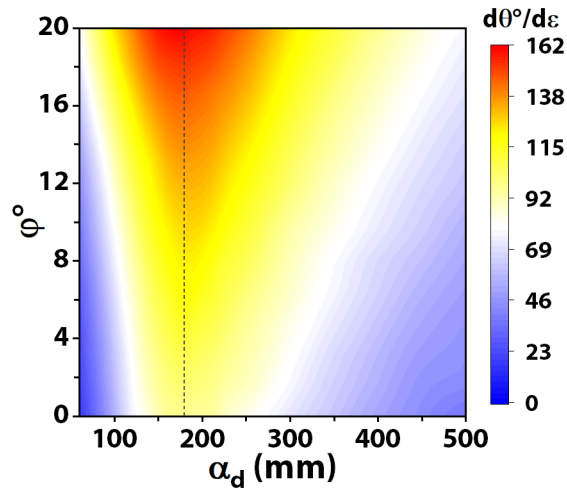


Figure 5.20. Contour plot of $d\theta/d\varepsilon$ as $\varepsilon \rightarrow 0$ for $n = 2$, φ ranging 0–20°, and α_d ranging 40–500 mm. $\alpha_d = 180$ mm (gray dotted vertical line) is a zeroth-order approximation of the locus of $d\theta/d\varepsilon_{max}|\varphi$.

inset), $d^2\theta/d\varepsilon^2$ is maximized near $\alpha_d \approx 150$ mm (at a lower α_d than that maximizing θ and $d\theta/d\varepsilon$; Figures 5.18e, 5.21). For bidirectional TMMs, both the twist per unit strain and the torque reach a maximum before passing through zero to negative as their direction of rotation switches (Figure 5.22).

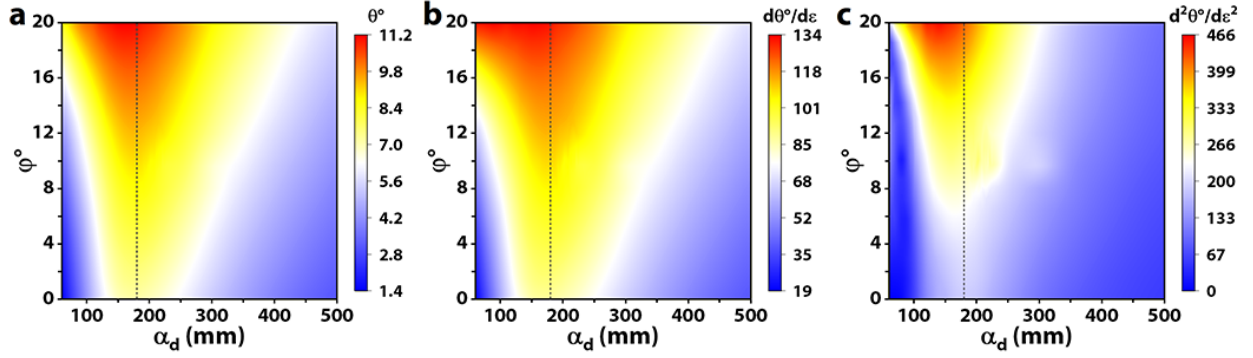


Figure 5.21. Contour plots of (a) θ , (b) $d\theta/d\varepsilon$, and (c) $d^2\theta/d\varepsilon^2$ at $\varepsilon = 0.075$ for $n = 2$, φ ranging 0–20°, and α_d ranging 40–500 mm. $\alpha_d = 180$ mm (gray dotted vertical line) is a zeroth-order approximation of the locus of $\theta_{max}|\varphi$.

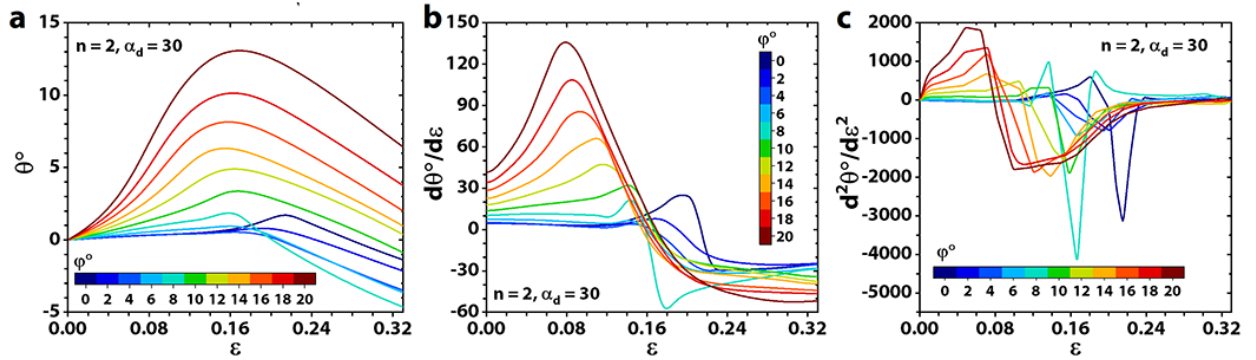


Figure 5.22. Dependence of the (a) twisting angle θ , (b) instantaneous twist per unit strain $d\theta/d\varepsilon$, and (c) normalized instantaneous angular acceleration $d^2\theta/d\varepsilon^2$ on the nominal strain ε for bidirectional TMMs with $n = 2$, $\alpha_d = 30$ mm, and φ ranging 0–20°.

5.2.4 Size-effect Independence of the Compression–Twist Coupling in TMMs

TMMs described until now had two levels of Voronoi cells ($n = 2$). Adding another level to the TMM structure ($n = 3$) modifies the transition boundary between unidirectional and bidirectional TMMs (Figure 5.18f,g). For $n = 3$, the onset of bidirectional behavior occurs at larger α_d for more cylindrical TMMs (lower φ values) and at smaller α_d for more conical TMMs (higher φ values). The area on the α_d – φ landscape occupied by bidirectional TMMs gradually decreases with n for TMMs with $n > 3$ (Figure 5.23) since the design rules of the proposed generative algorithm dictate that the beam thickness at every cross-section is proportional to the frustum diameter at that cross-section (Figure 5.18h, 5.3–5.6). This

proportionality ensures that the weight of a TMM is independent of n (all other parameters being constant; Figure 5.16e–h).

Although n and m can be specified independently during the design process, their relationship for a given cell aspect ratio (λ) is fixed. Figure 5.18i shows this almost-linear relationship for $\lambda = 2$, consequently demonstrating the size-effect independence of the global twisting behavior of TMMs (Figure 5.18k). The size-effect-free scalability of TMMs is also evidenced by the independence between their force and rotation responses (Figure 5.18j,k).

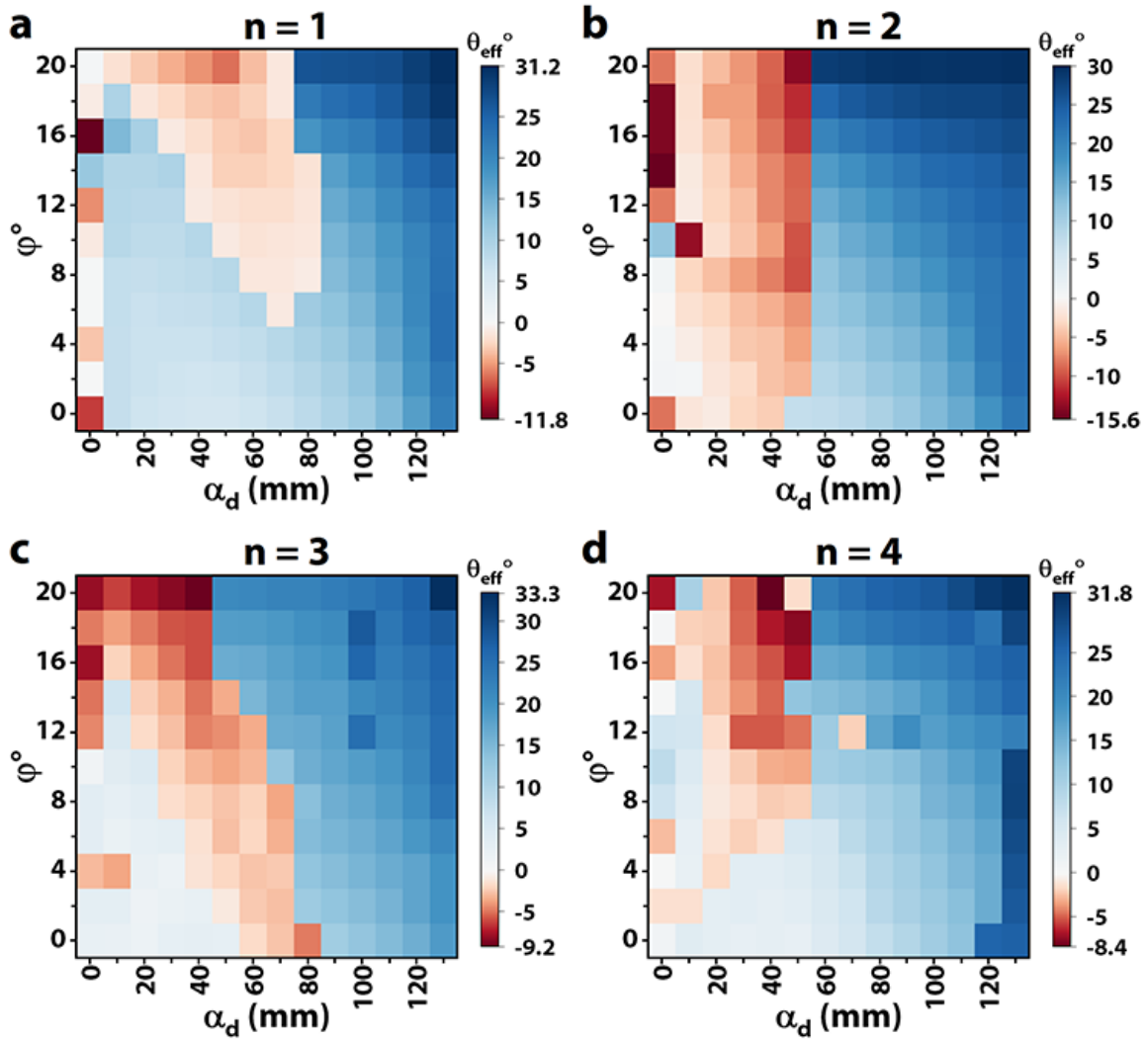


Figure 5.23. Heatmap of the effective twisting angle θ_{eff} for (a) $n = 1$, (b) $n = 2$, (c) $n = 3$, and (d) $n = 4$; φ ranging 0–20° and α_d ranging 0–130 mm. Shades of blue ($\theta_{eff} > 0$) indicate unidirectional twisting, while shades of red ($\theta_{eff} < 0$) denote bidirectional twisting.

5.2.5 Programmable Auxetic Behavior of TMMs

The Poisson’s ratio (ν) defines the ratio between the transverse strain and the axial strain. Conventional materials ($\nu > 0$) typically expand in the directions orthogonal to the applied compressive load. Auxetic materials ($\nu < 0$), on the other hand, contract in transverse directions when compressed.⁶⁵ We demonstrate that the Poisson’s ratio of TMMs can be programmed to acquire any value between +1.2 and -0.6 for compressive strains ranging $\varepsilon = 0$ –0.33, by tuning α_d and φ (Figures 5.24, 5.25, 5.26; also see Movie S3, Appendix B).

Due to the variable diameter of the tubular frusta-like geometries of TMMs, the traditional definition of ν given above is inadequate to fully capture the spatiotemporal evolution of the Poisson’s ratio in TMMs. We therefore define nine deformation-tracking sections (S_1 – S_9 ; Figure 5.24a) in each TMM and monitor their coordinates as a function of the applied axial strain (ε) to accurately calculate the instantaneous Poisson’s ratio of each section. As an example, Figure 5.24b,c shows the change in shape and orientation of section S_5 of a TMM ($n = 2$, $\varphi = 12^\circ$, $\alpha_d = 90$ mm) from $\varepsilon = 0$ to $\varepsilon = 0.33$. Although the sections S_1 to S_9 are equispaced at $\varepsilon = 0$, their relative separations do not remain constant as ε increases (Figure 5.27a); it is even possible that a section which starts higher than another ends at a lower height at $\varepsilon = 0.33$ due to beam buckling accumulation (Figure 5.24g, 5.28a).

By recording the local radius (r_{local}) at each section S_i ($i = 1, 2, \dots, 9$; Figure 5.27b), we calculated the radial strain ε_r (Figure 5.24d), which then allowed us to compute the Poisson’s ratios as $\nu = -\varepsilon_r/\varepsilon$ (Figure 5.24e). Our protocol to characterize the Poisson’s ratio of TMMs using the nine deformation-tracking sections reveals that it is possible for different sections in the same TMM to exhibit significantly different Poisson effects simultaneously. For example, in the TMM described in Figure 5.24a–e, section S_6 first expands in radius before sharply contracting below its initial value as the local ν at this section changes from +0.42 ($\varepsilon = 0$) to -0.17 ($\varepsilon = 0.33$), while the radius of section S_4 monotonically increases during compression, maintaining $\nu > 0$ for $0 < \varepsilon \leq 0.33$. It is also possible to find TMMs exhibiting Poisson effects at the two extremes: for example, ν is always positive (for all ε at every cross-section S_i) in a TMM with $n = 2$, $\varphi = 10^\circ$, and $\alpha_d = 0$; while ν is always negative (for all ε and S_i) in a TMM with $n = 2$, $\varphi = 6^\circ$, $\alpha_d = 200$ mm (Figure 5.28).

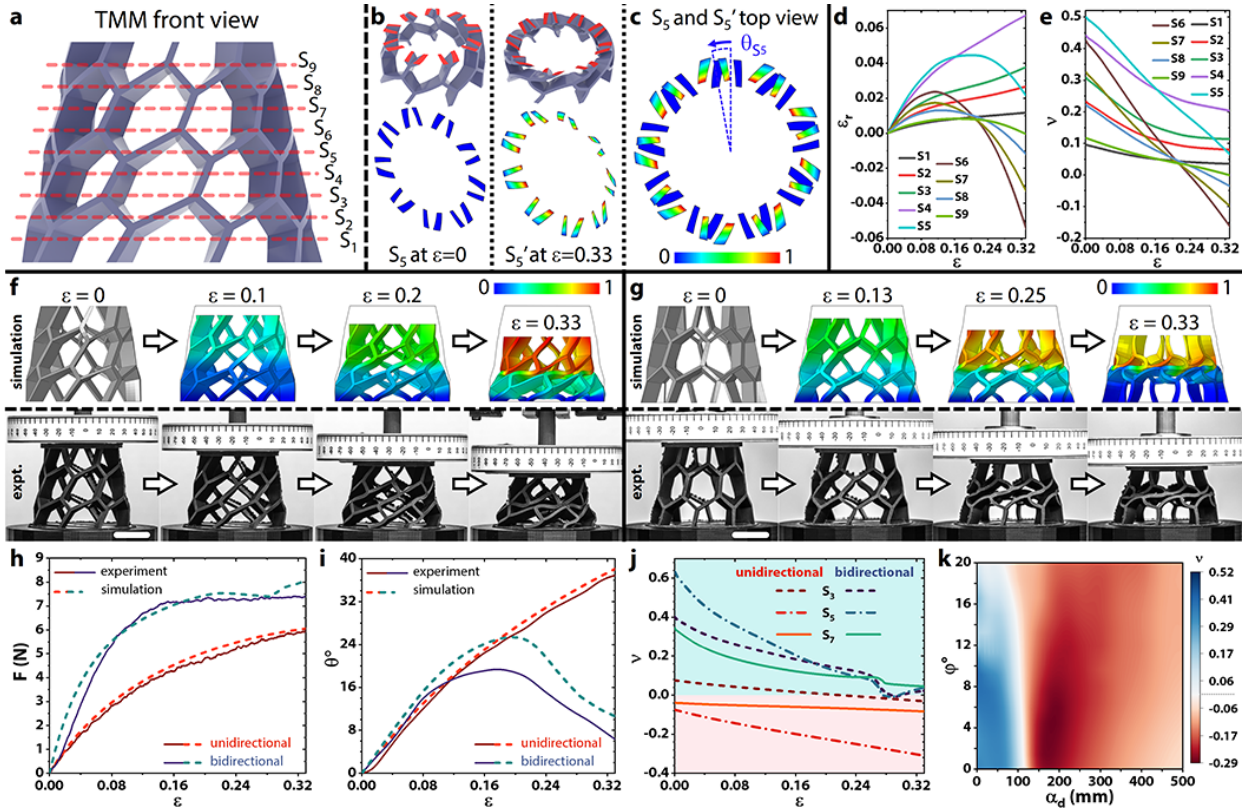


Figure 5.24. Programmable auxetic behavior of TMMs. (a) Schematic diagram of the front view of a representative TMM ($n = 2$, $\varphi = 12^\circ$, and $\alpha_d = 90$ mm) with red dotted lines indicating the initial positions of 9 deformation-tracking sections S_1 – S_9 (equispaced at $\varepsilon = 0$) used for Poisson’s ratio evaluation. (b) Geometry (top) and normalized displacement distribution (bottom) of section S_5 at $\varepsilon = 0$ (left) and $\varepsilon = 0.33$ (right). (c) Super-imposed normalized displacement distributions of section S_5 ($\varepsilon = 0$) and S_5' ($\varepsilon = 0.33$). (d) Variation of the induced radial strain ε_r as a function of the applied nominal strain ε , at the 9 sections of the TMM shown in (a). (e) Variation of Poisson’s ratio $\nu = -\varepsilon_r/\varepsilon$ as a function of the applied nominal strain ε , at the 9 sections. (f, g) FEA simulation (top) and experimental snapshots (bottom) showing the profile evolution due to compression-twist coupling of representative unidirectional (f; $\nu < 0$) and bidirectional (g; $\nu > 0$) TMMs. Color bars indicate normalized displacement distribution. Scale bars are 2 cm. (h) F – ε curves of the unidirectional and bidirectional TMMs shown in (f) and (g), respectively. (i) Compression-twist coupling of the unidirectional and bidirectional TMMs shown in (f) and (g), respectively. (j) Local variation of the Poisson’s ratio ν for the unidirectional and bidirectional TMMs shown in (f) and (g), respectively. The unidirectional TMM is auxetic ($\nu < 0$) at the middle section S_5 for all ε . (k) Heatmap of the Poisson’s ratio ν calculated at section S_5' ($\varepsilon = 0.33$), for $n = 2$, $\varphi = 0$ – 20° , and $\alpha_d = 0$ – 500 mm. Shades of red ($\nu < 0$) indicate auxetic behavior.

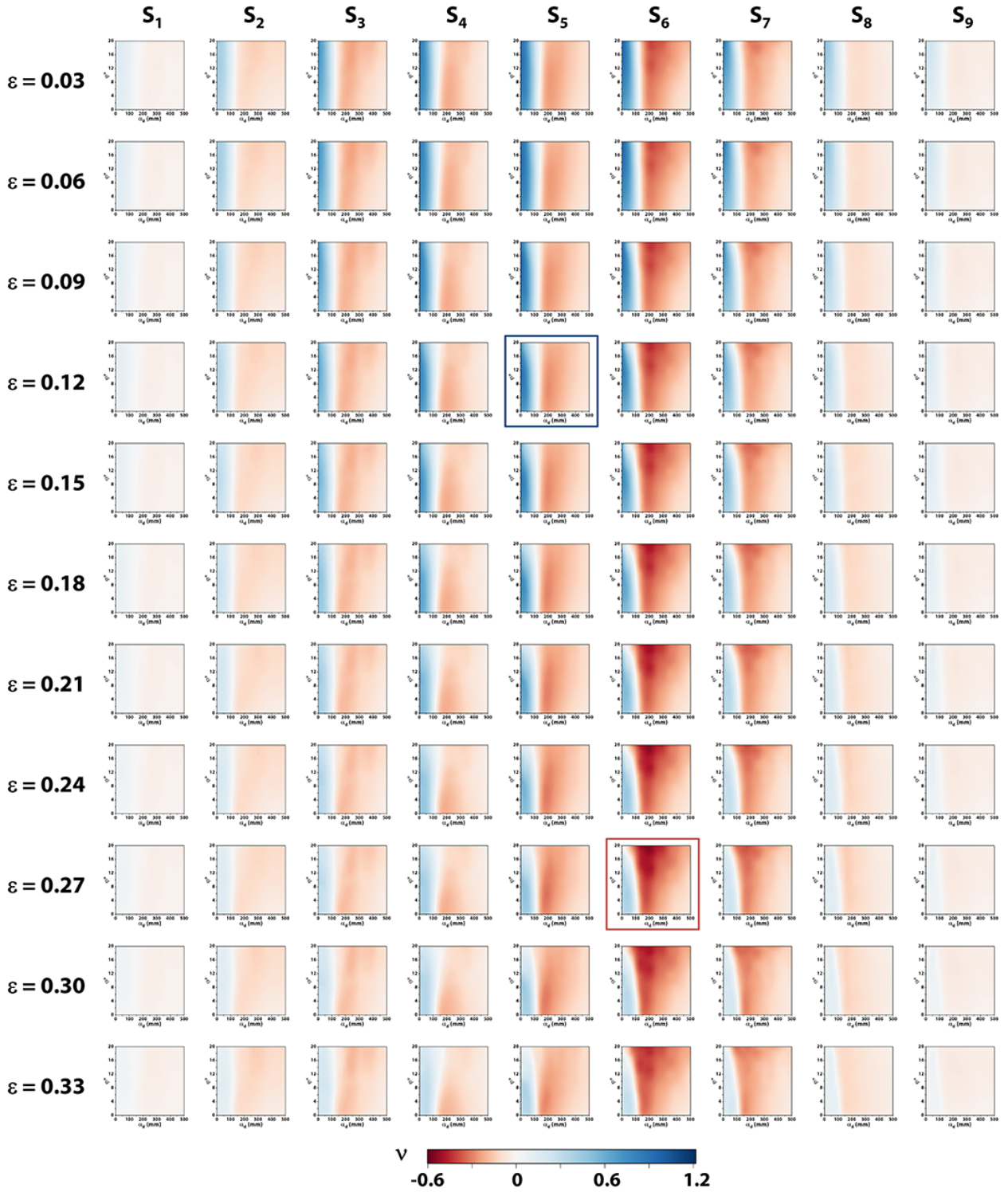


Figure 5.25. Spatiotemporal evolution of Poisson's ratio of TMMs with $n = 2$, as a function of α_d (horizontal axes; ranging 0–500 mm) and φ (vertical axes; ranging 0–20°). Panel with blue border indicates occurrence of $\nu_{max} = 1.22$; panel with red border indicates occurrence of $\nu_{min} = -0.6$.

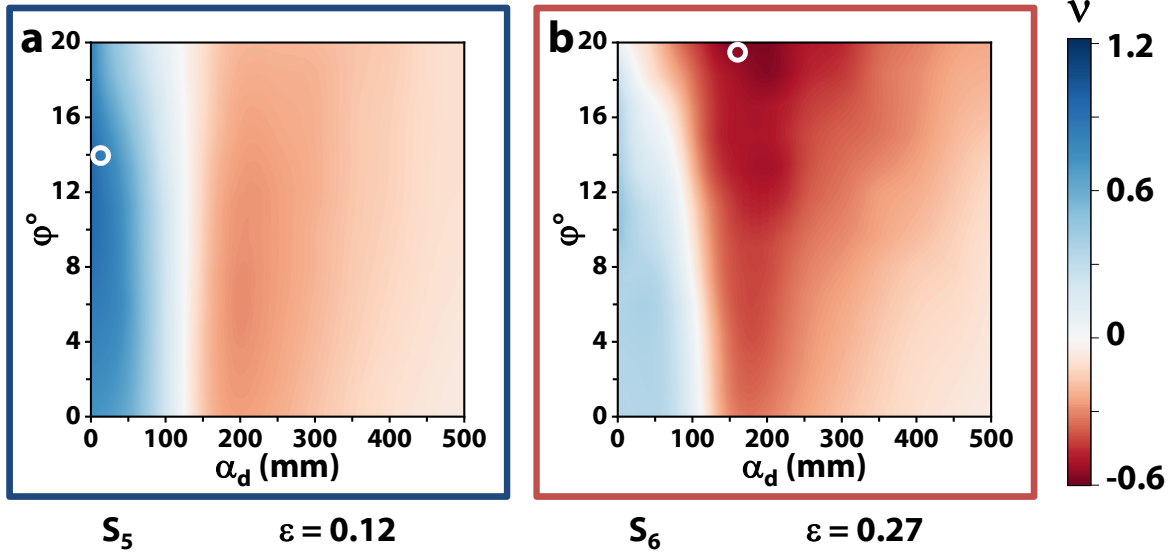


Figure 5.26. Snapshots from the spatiotemporal evolution of ν showing the occurrences of (a) $\nu_{max} = 1.22$, and b) $\nu_{min} = -0.6$.

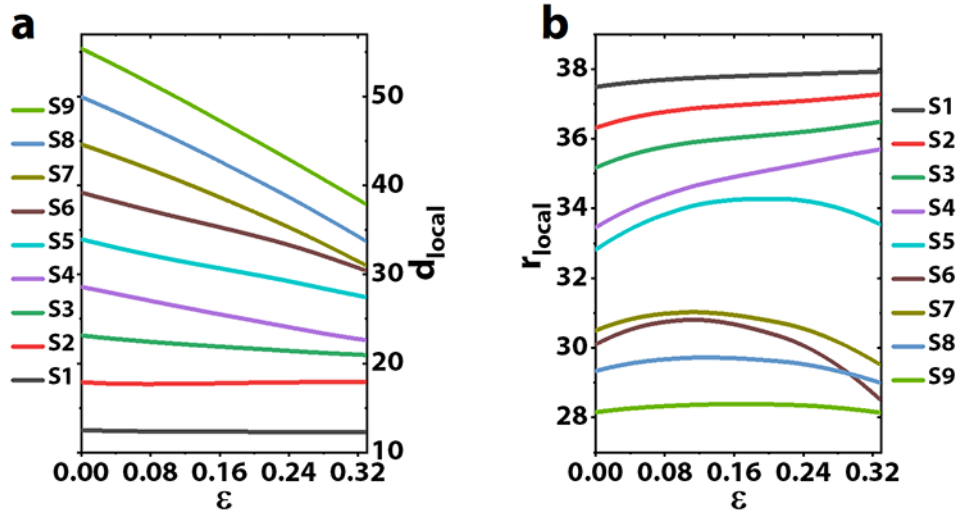


Figure 5.27. (a) Variation of the local displacement at the deformation-tracking sections S_1 – S_9 as a function of the applied strain. (b) Variation of the local radius at the deformation-tracking sections S_1 – S_9 as a function of the applied strain.

We compared the experimental and simulated deformation profiles of two TMMs, one unidirectional ($n = 1$, $\varphi = 12^\circ$, $\alpha_d = 160$ mm; Figure 5.24f; also see Movie S4, Appendix B) and one bidirectional ($n = 1$, $\varphi = 12^\circ$, $\alpha_d = 60$ mm; Figure 5.24g; also see Movie S5, Appendix B), to verify the validity of our Poisson’s ratio analysis. There is excellent agreement between

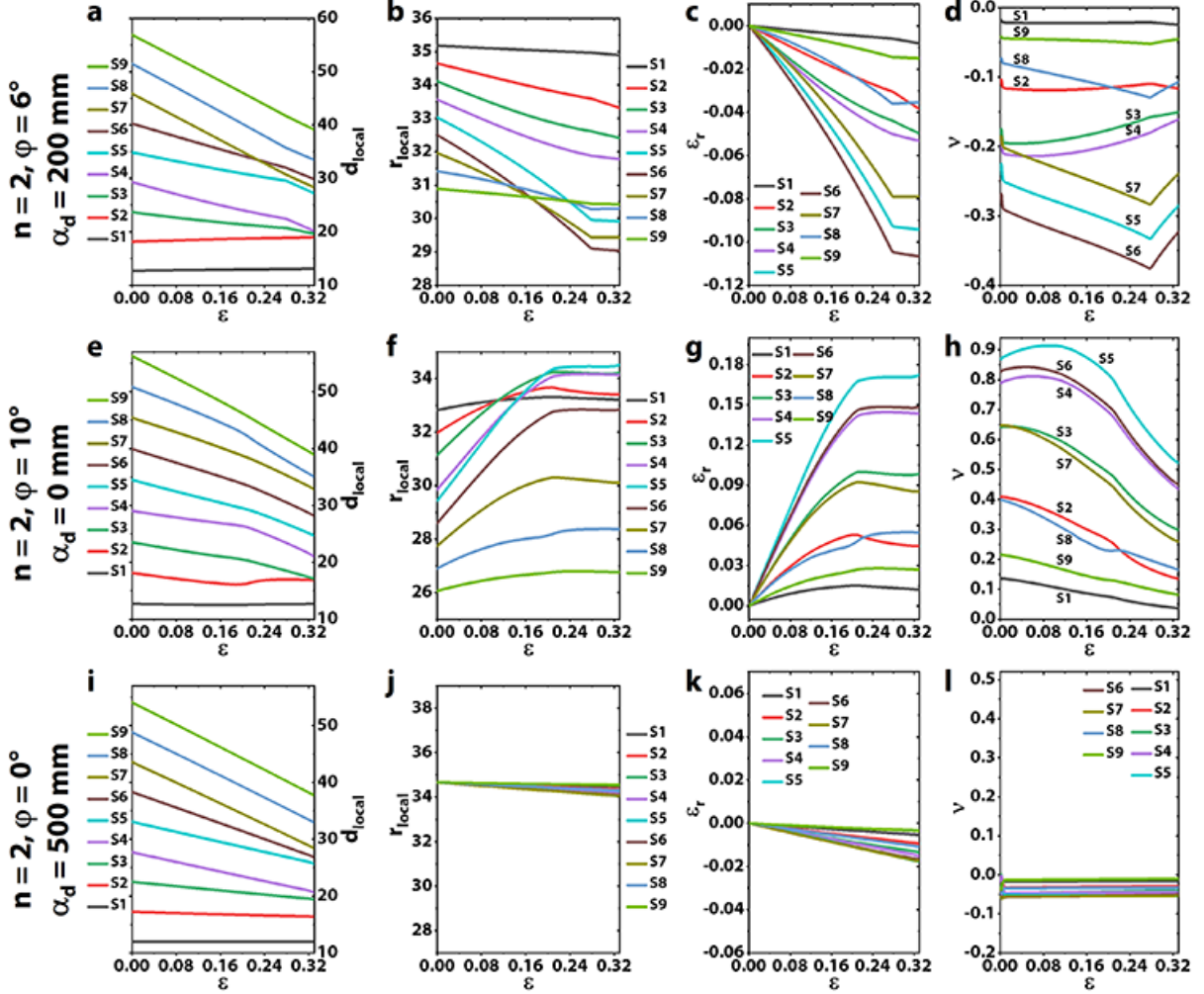


Figure 5.28. Evolution of the nominal Poisson's ratio as a function of the applied strain at the nine deformation-tracking sections for (a–d) a TMM with $\nu < 0$ at all S_i ($i = 1, 2, \dots, 9$) and ε ; (e–h) a TMM with $\nu > 0$ at all S_i ($i = 1, 2, \dots, 9$) and ε ; (i–l) a TMM with ν close to 0 at all S_i ($i = 1, 2, \dots, 9$) and ε .

experimental and simulation results for both reaction force (Figure 5.24h) and compression-twist coupling (Figure 5.24i). Moreover, the Poisson's ratio evolution predicted by FEA (Figure 5.24j) is qualitatively corroborated by the experimental snapshots (Figure 5.24f,g).

Finally, we depict on the $\alpha_d - \varphi$ landscape, all TMMs which exhibit auxetic behavior. The contour plot in Figure 5.24k provides general design guidelines for picking a desired ν . Note that this plot shows ν at S_5 for $\varepsilon = 0.33$; the complete spatiotemporal evolution is available in Movie S3 (Appendix B) and Figure 5.25. In general, it is possible to outline contiguous areas on the $\alpha_d - \varphi$ landscape which always (at all S_i , for any ε in 0–0.33) exhibit positive

or negative ν (Figure 5.29). 64.69% TMMs with $n = 2$ exhibit $\nu < 0$, 11.82% TMMs exhibit $\nu > 0$, and 23.49% TMMs exhibit simultaneously $\nu < 0$ and $\nu > 0$ at different cross-sections. An important correlation between unidirectional TMMs and auxeticity ($\nu < 0$) emerges: all globally auxetic TMMs are unidirectional, while all unidirectional TMMs are not necessarily globally auxetic.

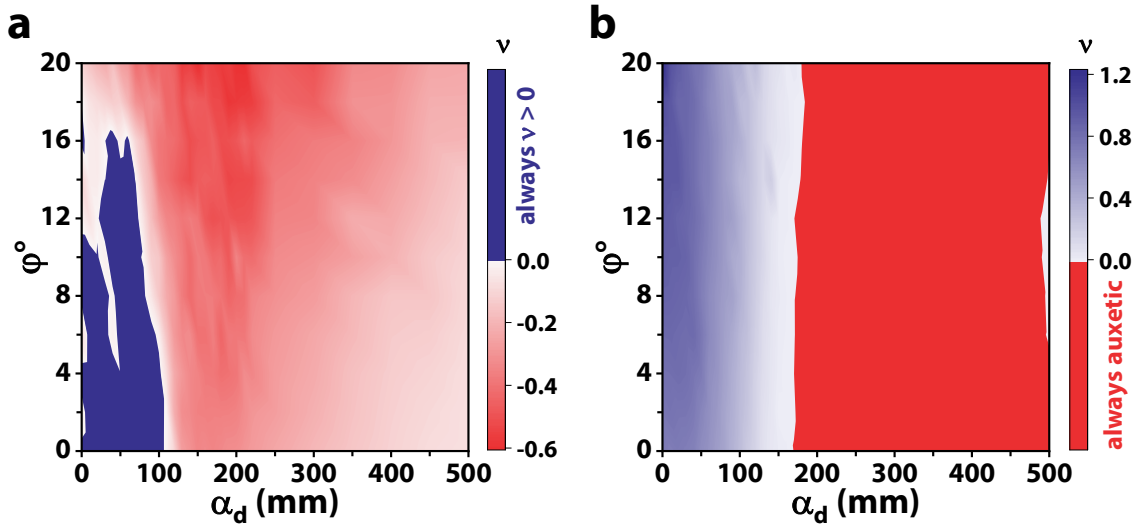


Figure 5.29. Contour plots showing the regions on the α_d - ϕ landscape where (a) ν always > 0 (colored solid blue) for all ε at every S_i ($i = 1, 2, \dots, 9$); (b) ν always < 0 (colored solid red) for all ε at every S_i ($i = 1, 2, \dots, 9$).

5.2.6 Non-reciprocity and Path-dependence in TMMs

Reciprocity is a constitutive property of physical systems which ensures that the transmission of signals, be it electromagnetic, acoustic, or mechanical, is symmetric between any two points in space.^{159,160} Traditional mechanical mechanisms which convert displacement to rotation (e.g. a slider-crank mechanism) are all reciprocal. Bidirectional TMMs, in contrast, exhibit intrinsic non-reciprocity since they autonomously switch their direction of rotation (see Movies S2 and S5, Appendix B) during uniform displacement-controlled compressive loading (Figure 5.30).

Figure 5.30a1 shows the transformation of a linear vertical displacement (at 1 mm/s) into bidirectional rotation in a TMM previously known to exhibit bidirectional behavior ($n = 2$,

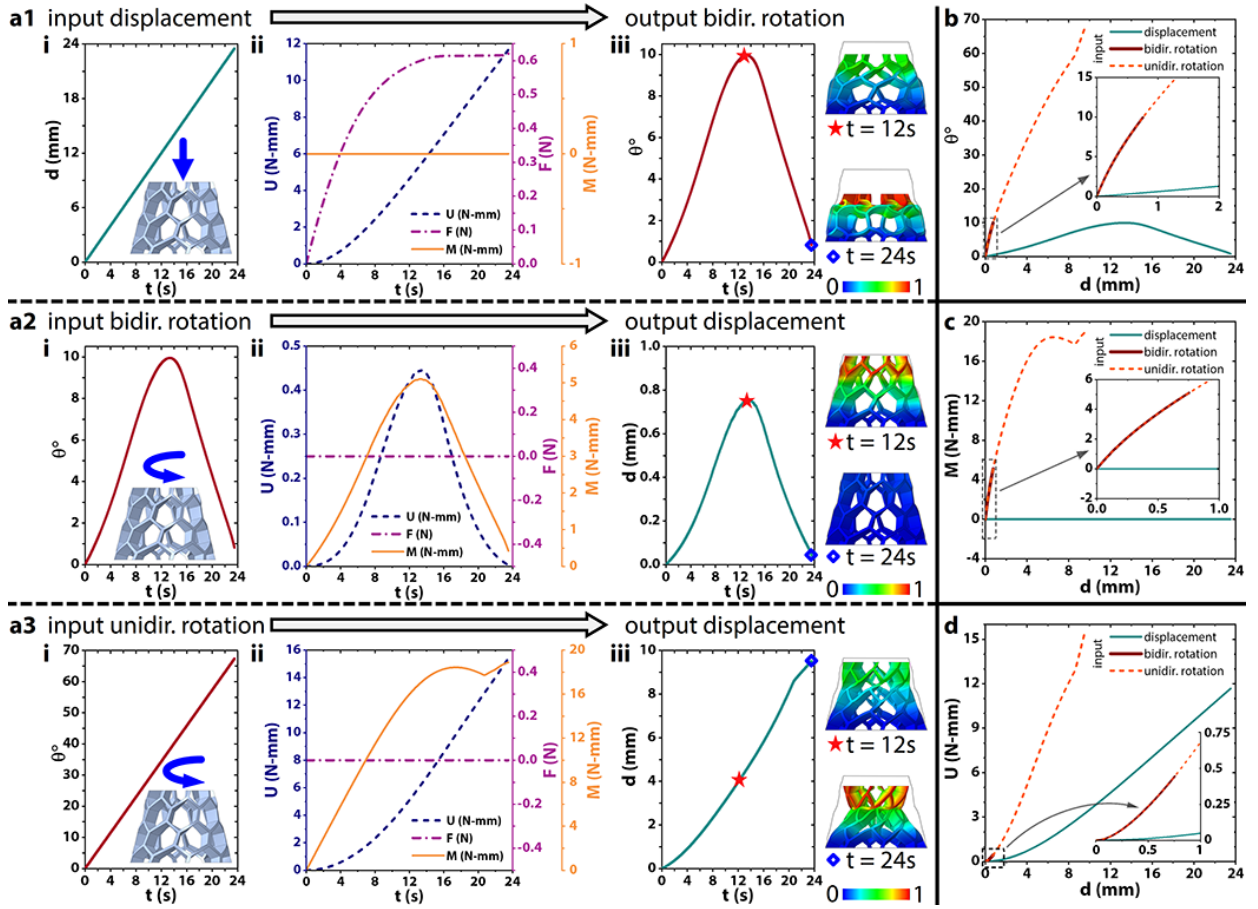


Figure 5.30. Non-reciprocity and path-dependence in bidirectional TMMs. (a) Different input loading conditions applied to the same representative bidirectional TMM ($n = 2$, $\varphi = 14^\circ$, $\alpha_d = 50$ mm) and corresponding responses as a function of time. (a1) linear displacement-controlled loading: (i) a uniform normal compression at 1 mm/s is applied, (ii) variation of the strain energy U , normal reaction force F , and reaction moment M as a function of time, (iii) resulting bidirectional rotation. (a2) nonlinear rotation-controlled loading: (i) the bidirectional rotation obtained in (a1iii) is applied as input, (ii) dependence of U , F , and M on time, (iii) resulting displacement as a function of time. (a3) linear rotation-controlled loading: (i) a uniform counterclockwise rotation of $2.86^\circ/\text{s}$ is applied, (ii) variation of U , F , and M with time, (iii) resulting displacement as a function of time. (b) Compression-twist coupling response for the three input loading conditions in (a). (c) Dependence of M as a function of the vertical displacement, for the three input loading conditions. (d) Dependence of the strain energy U stored in the TMM as a function of the vertical displacement, for the three input loading conditions.

$\varphi = 14^\circ$, $\alpha_d = 50$ mm; Figure 5.11a). Since the top surface of the TMM is free to rotate in this experimental condition, the recorded reaction moment (M) is zero (Figure 5.30a1ii). The resulting bidirectional rotation output (as a function of time) obtained during this experiment (Figure 5.30a1iii) is then applied as the input loading condition to the same TMM (Figure 5.30a2i). The output displacement response (Figure 5.30a2iii) does not reproduce the input displacement in Figure 5.30a1i, unveiling the non-reciprocal behavior of bidirectional TMMs. This behavior can be explained by the significantly different kinetic response of this TMM for the first (Figure 5.30a1ii) and second (Figure 5.30a2ii) loading conditions.

In (a1), the TMM experiences a snap-through instability which switches its direction of rotation, while in (a2) there is no snap-through since the small vertical displacement prevents beam buckling (see the output FEA simulations in Figure 5.30a1,2). For completeness, we also tested the case in which we impose a uniform linear (unidirectional) rotational input (Figure 5.30a3) to the top surface of this bidirectional TMM.

The compression-twist coupling responses for the three loading conditions described is plotted in Figure 5.30b, demonstrating the different outputs of the TMM for vertical displacement and bidirectional rotation inputs. It is interesting, and somewhat non-intuitive, to note that the output response to any unidirectional rotation input follows the exact same angle (θ), moment (M), and strain energy (U) paths as the output response to a bidirectional rotation input, albeit for much shorter vertical displacements (Figure 5.30b–d). Moreover, irrespective of the loading rate, there are only two possible deformation paths for bidirectional TMMs: one for displacement-controlled loading and one for rotation-controlled loading. Displacement control generates the path that minimizes the strain energy stored in the TMM (green line in Figure 5.30d). Unidirectional TMMs are reciprocal and their deformations lie on a single path, independent of the loading conditions.

5.3 Conclusion

In this chapter, we introduced TMMs—a new class of mechanical metamaterials whose rationally-designed architecture endows them with compression-twist coupling, a property absent in conventional materials. We demonstrated that this twisting response—unidirectional or bidirectional—manifests macroscopically ($> 38^\circ$), is mechanical-frustration-free up

to large deformations, is independent of the flexible bulk material chosen to fabricate the TMM, and can be programmed by simply tuning two design parameters. Moreover, the proposed TMM designs do not suffer from size effects which compromise their twist per unit strain, thus ensuring both cellular and global scalability. We also demonstrated that the twisting behavior determines the onset of auxeticity, with TMMs exhibiting Poisson’s ratios in the continuous range -0.6 to $+1.22$. Finally, we showed that the family of bidirectional TMMs is non-reciprocal since they autonomously switch their direction of rotation during uniform displacement-controlled compressive loading.

The capability to controllably convert translation to rotation using monolithic TMMs blurs the boundary between materials and machines,^{161–163} paving the way toward the creation of future programmable matter whose complex motion is directly encoded within the architecture of the mechanical metamaterial. We envision the non-reciprocity of bidirectional TMMs to be exploited in applications such as shock absorption^{159,160} and energy harvesting,^{164,165} as well as in the design of mechanical metamaterial diodes^{166–168} for soft robotics and prosthetics. Post-fabrication tuning of TMMs can be realized by modular stacking or fabrication using shape memory polymers.¹⁶⁹ Coupled with stimuli-responsive actuation¹⁷⁰ and inverse design techniques,¹⁷¹ we also envision TMMs to find potential applications in the biomedical field, such as in the design and manufacture of meta-implants,^{172–174} expandable coronary stents,^{175,176} and ventricular assist devices.^{177–179}

5.4 Experimental Section

5.4.1 Rational, automated design of TMMs

TMMs were designed using a generative algorithm developed in the visual programming language Grasshopper[®] (version 1.0) that runs within the CAD environment Rhinoceros 3D (version 6; Robert McNeel & Associates, Seattle, WA) and follows the steps outlined in Figure 5.1a–c. This algorithm takes the following parameters as inputs to design a TMM: frustum base radius (r_b), frustum height (h), number of levels (n), number of cells on each level (m), cell aspect ratio (λ), beam thickness (t_{beam} ; measured at the surface of the frustum), beam extrusion depth (ED_{beam}), curve distance (α_d), and frustum apex semi-angle (φ). Only

n , m , α_d , and φ were varied in this study; other parameters were kept constant at values that minimize mechanical frustration while still being easy to fabricate using regular 3D printers ($r_b = 37.5$ mm, $h = 60$ mm, $\lambda = 2$, $t_{beam} = 1.4$ mm, $ED_{beam} = 10$ mm). While the design space may be broadened by varying these parameters, the general trends in mechanical responses are expected to follow similar paths as described.

The design problem has been solved using a forward approach in this study. If specific mechanical properties or deformation trajectories are desired at particular locations of a TMM, an inverse problem needs to be solved. While this is still an evolving, and largely uncharted, domain in mechanical metamaterial design, gradient-free optimization algorithms present a viable approach for systematic future investigations.¹⁷¹

For the current study, both the Grasshopper generative algorithm and the entire gamut of 781 TMM designs analyzed are available from the author upon reasonable request.

5.4.2 Finite element simulations

FEA simulations were performed using the commercial package Abaqus/CAE (version 2017; Dassault Systèmes Simulia Corp., Providence, RI) to evaluate the mechanical deformation upon compression of 781 TMMs. Each TMM was simulated for different fabrication materials: FLGR02, ELCL01, and Ecoflex 00–30, all modeled as hyperelastic and described by a third-order Ogden model.^{146,154} Ogden model parameters used for FLGR02 are: $\mu_1 = -19.892$ MPa, $\mu_2 = 10.520$ MPa, $\mu_3 = 10.834$ MPa, $\alpha_1 = -2.370$, $\alpha_2 = -0.940$, $\alpha_3 = -3.915$, $D_1 = D_2 = D_3 = 0$. Ogden model parameters used for ELCL01 are: $\mu_1 = 0.499$ MPa, $\mu_2 = 1.336 \times 10^{-2}$ MPa, $\mu_3 = -1.260 \times 10^{-2}$ MPa, $\alpha_1 = 1.999$, $\alpha_2 = 4.007$, $\alpha_3 = -1.998$, $D_1 = D_2 = D_3 = 0$. These parameters were determined by fitting the model to stress–strain data obtained by uniaxial tensile testing of dogbone samples 3D printed using the respective photopolymers (Figure 5.31). Ogden model parameters used for Ecoflex 00–30 are: $\mu_1 = 0.0244$ MPa, $\mu_2 = 6.67 \times 10^{-5}$ MPa, $\mu_3 = 4.538 \times 10^{-4}$ MPa, $\alpha_1 = 1.7138$, $\alpha_2 = 7.0679$, $\alpha_3 = -3.3659$, $D_1 = 3.258$ MPa⁻¹, $D_2 = D_3 = 0$. These parameters were previously determined and reported by our group.¹⁸⁰

TMM models were meshed using second-order tetrahedral elements of type C3D10H (for FLGR02 and ELCL01) or C3D10 (for Ecoflex 00–30) with maximum allowed mesh size

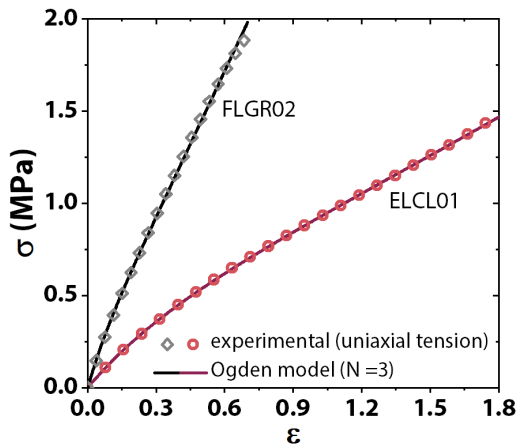


Figure 5.31. Experimental stress-strain curves from uniaxial tensile testing of dogbone samples (solid lines) and Ogden model fit (symbols) of the two photopolymers, FLGR02 and ELCL01, used to 3D print TMMs.

of $500\ \mu\text{m}$. All six degrees of freedom were constrained at the bottom surface of the TMM, while the terminal top surfaces of the beams were coupled to a reference point (Figure 5.9a,b) and free to rotate about the vertical axis. This reference point was displaced vertically to compress (at $1\ \text{mm/s}$) the TMM by one-third its original height (up to $\varepsilon = 0.33$).

5.4.3 Fabrication of TMMs

Experimental TMMs were 3D printed with a high-resolution ($50\ \mu\text{m}$) stereolithography printer (Form 2; Formlabs, Somerville, MA) using two different flexible photopolymers, FLGR02 (tensile strength $\sim 8.5\ \text{MPa}$, maximum elongation at break $\sim 70\%$, Shore hardness 80A) and ELCL01 (tensile strength $\sim 3.23\ \text{MPa}$, maximum elongation at break $\sim 180\%$, Shore hardness 50A). After printing, the models were sonicated in isopropanol for 10 min to dissolve any uncured photopolymer. The ELCL01 models required post-curing in UV light ($405\ \text{nm}$) at 60°C for 15 min to eliminate surface tackiness.

5.4.4 Mechanical characterization of TMMs

A custom-built fixture, immobilizing the bottom surface of the TMM and allowing its top surface to rotate freely while being compressed, was integrated in a universal testing machine

setup (Insight 10; MTS Systems Corp., Eden Prairie, MN) to characterize the compression-twist coupling of the fabricated TMMs (Figure 5.9d–f). TMMs were compressed at a rate of 1 mm/min up to a nominal strain of $\varepsilon = 0.33$, while the reaction force was recorded using a 100 N load cell.

CHAPTER 6. OUTLOOK

This dissertation provided accessible strategies for the design and fabrication of both optical and mechanical metamaterials. In Chapters 2 and 3, I demonstrated scalable nanomanufacturing methods to create flexible optical metamaterials, while in Chapters 4 and 5, I provided algorithmic design tools to create mechanical metamaterials for soft robotic applications.

Although at first glance, the domains of optical and mechanical metamaterials may appear to be detached, analogous underlying principles govern their properties.¹⁸¹ A continuum description of optics, in the Einstein summation notation, is provided by Equations 6.1 and 6.2.

$$D_i = \varepsilon_0 \varepsilon_{ij} E_j + i c_0^{-1} \xi_{ij} H_j \quad (6.1)$$

$$B_i = i c_0^{-1} \zeta_{ij} E_j + \mu_0 \mu_{ij} H_j \quad (6.2)$$

Here, ε_{ij} is the rank-two electric permittivity tensor, with $i, j = 1, 2, 3$; D_i is the dielectric displacement vector field; E_i is the electric vector field; μ_{ij} is the magnetic permeability tensor; B_i is the magnetic induction vector; H_i is the magnetic field vector; $\varepsilon_0 = 8.854 \times 10^{-12} \text{ A s V}^{-1} \text{ m}^{-1}$ and $\mu_0 = 4\pi \times 10^{-7} \text{ V s A}^{-1} \text{ m}^{-1}$ are the vacuum permittivity and permeability, respectively; and $c_0 = 1/\sqrt{\varepsilon_0 \mu_0}$ is the speed of light in vacuum. ξ_{ij} is the chirality tensor, all elements of which are strictly zero in the presence of centrosymmetry. Further, due to reciprocity, $\zeta_{ij} = -\xi_{ji}$.

The mechanical counterparts of Equations 6.1 and 6.2 are given by Equations 6.3 and 6.4.

$$\sigma_{ij} = C_{ijkl} \varepsilon_{kl} + D_{ijkl} \varphi_{kl} \quad (6.3)$$

$$m_{ij} = B_{ijkl} \varepsilon_{kl} + A_{ijkl} \varphi_{kl} \quad (6.4)$$

Here, all material tensors are of rank four rather than rank two; they have four indices $i, j, k, l = 1, 2, 3$. The counterpart of the rank-two electric permittivity tensor is the rank-four elasticity tensor with components C_{ijkl} . σ_{ij} is the stress tensor and ε_{ij} is the generalized strain tensor.[†] Due to reciprocity, $D_{ijkl} = B_{lkij}$.[§] m_{ij} and φ_{ij} are pseudo-tensors for the torque field and the rotational fields, respectively, connected by the tensor A_{ijkl} .

Comparing the optical and mechanical equation systems above, we note that electrical degrees of freedom in electromagnetism are analogous to translational degrees of freedom in continuum mechanics. Similarly, the magnetic degrees of freedom are analogous to rotational degrees of freedom. In the mechanics equations, the tensor components B_{ijkl} and D_{ijkl} describe the coupling of translational degrees of freedom to rotational degrees of freedom, and vice versa. Just as $\xi_{ij} = 0$ in the optical equations when there is centrosymmetry, analogously centrosymmetry in continuum mechanics mandates $B_{ijkl} = D_{ijkl} = 0$. Therefore, to obtain a coupling between translational and rotational degrees of freedom, it is essential to break centrosymmetry.¹⁸¹

The above principles were at the core of the twisting mechanical metamaterials (TMMs) presented in Chapter 5. The capability of TMMs to controllably convert translation to rotation blurs the boundary between materials and machines, expanding the range of mechanical properties currently accessible to 3D printed materials and paving the way toward the creation of future programmable matter. Moreover, due to the close mathematical analogies described above, it is not unreasonable to envision that integration of optical and mechanical metamaterials in the same system will lead to the emergence of unprecedented and exotic functionalities.

[†]Note that the symbol ε is used for both, the electric permittivity in optics and the strain in mechanics, and should not be confused.

[§]Observe that the first and second pairs of indices are interchanged and l and k are swapped.

APPENDIX A. MATLAB CODES

MATLAB code for Delaunay triangulation

```

## FlexiLab, School of Industrial Engineering, Purdue University
## @deftypefn {Loadable Function} {@var{tri}=} delaunay (@var{x}, @var{y})
## @deftypefnx {Loadable Function} {@var{tri}=} delaunay (@var{x},
## @var{y}, @var{opt})
## The return matrix of size [n, 3] contains a set of triangles which are
## described by the indices to the data point x and y vector.
## The triangulation satisfies the Delaunay circumcircle criterion.
## No other data point is in the circumcircle of the defining triangle.
##
## A third optional argument, which must be a string, contains extra
## options passed to the underlying qhull command. See the documentation
## for the Qhull library for details.
##
## @example
## x = rand(1,10);
## y = rand(size(x));
## T = delaunay(x,y);
## X = [ x(T(:,1)); x(T(:,2)); x(T(:,3)); x(T(:,1)) ];
## Y = [ y(T(:,1)); y(T(:,2)); y(T(:,3)); y(T(:,1)) ];
## axis([0,1,0,1]);
## plot(X,Y,'b;','x,y','r*;;');
## @end example
## @end deftypefn

```

```

## @seealso{voronoi, delaunay3, delaunayn}
function ret = delaunay (x,y,opt)
    if ((nargin != 2) && (nargin != 3))
        usage ("delaunay(x,y[,opt])");
    endif
    if (is_vector(x) && is_vector(y) && (length(x) == length(y)) )
        if (nargin == 2)
            tri = delaunayn([x(:), y(:)]);
        elseif isstr(opt)
            tri = delaunayn([x(:), y(:)], opt);
        else
            error("third argument must be a string");
        endif
    else
        error("first two input arguments must be vectors of same size");
    endif
    if nargin == 0
        x = x(:).'; y = y(:).';
        X = [ x(tri(:,1)); x(tri(:,2)); x(tri(:,3)); x(tri(:,1)) ];
        Y = [ y(tri(:,1)); y(tri(:,2)); y(tri(:,3)); y(tri(:,1)) ];
        plot(X,Y,'b;','x,y','r*;;');
    else
        ret = tri;
    endif
endfunction

```

MATLAB code for Voronoi tessellation

```

## FlexiLab, School of Industrial Engineering, Purdue University
## @deftypefn {Function File} {} voronoi (@var{X},@var{Y})
## @deftypefnx {Function File} {} voronoi (@var{X},@var{Y},"plotstyle")
## @deftypefnx {Function File} {} voronoi (@var{X},@var{Y},
## "plotstyle",@var{OPTIONS})
## @deftypefnx {Function File} {[@var{vx}, @var{vy}] =} voronoi (@var{X},
## @var{Y})
## plots voronoi diagram of points @var{X},@var{Y}.
## The voronoi facets with points at infinity are not drawn.
## [@var{vx}, @var{vy}] = voronoi(...) returns the vertices instead
## plotting the diagram. plot (@var{vx}, @var{vy})
## shows the voronoi diagram.
## A fourth optional argument, which must be a string, contains extra
## options passed to the underlying qhull command. See the documentation
## for the Qhull library for details.
##
## @example
## x = rand(10,1); y = rand(size(x));
## h = convhull(x,y);
## [vx,vy] = voronoi(x,y);
## plot(vx,vy,"-b;","x,y","o;points","x(h),y(h)","-g;hull;")
## @end example
##
## @end deftypefn
## @seealso{voronoin, delaunay, convhull}
## * limit the default graph to the input points rather than the
## whole diagram
## * provide example

```

```

## * use unique(x,"rows") rather than __unique_rows__
## Added optional fourth argument to pass options to the underlying
## qhull command
function [varargout] = voronoi (x, y, plt, opt)
if (nargin < 2 || nargin > 4)
usage ("voronoi (x, y[, plt[, opt]])")
endif
if (nargin < 3)
plt = "b;";
## if not specified plot blue solid lines
endif
    if (nargin == 4)
if (! isstr (opt))
error ("fourth argument must be a string");
endif
else
opt = "";
endif
lx = length (x);
ly = length (y);
if (lx != ly)
error ("voronoi: arguments must be vectors of same length");
endif
[p, lst, infi] = __voronoi__ ([x(:),y(:)], opt);
idx = find (!infi);
ll = length (idx);
k = 0;r = 1;
for i = 1:ll
k += length (nth (lst, idx(i)));
endfor

```

```

vx = zeros (2,k);
vy = zeros (2,k);
for i=1:ll
fac = nth (lst, idx(i));
lf = length(fac);
fac = [fac, fac(1)];
fst = fac(1:length(fac)-1);
sec = fac(2:length(fac));
vx(:,r:r+lf-1) = [p(fst,1),p(sec,1)]';
vy(:,r:r+lf-1) = [p(fst,2),p(sec,2)]';
r += lf;
endfor
[vx,idx] = unique(vx,"rows");
vy = vy(idx,:);
if (nargout == 0)
lim = [min(x(:)), max(x(:)), min(y(:)), max(y(:))];
    axis(lim+0.01*[[ -1,1]*(lim(2)-lim(1)), [-1,1]*(lim(4)-lim(3))]);
plot (vx, vy, plt, x, y, 'o;;');
elseif (nargout == 2)
vr_val_cnt = 1; varargout{vr_val_cnt++} = vx;
varargout{vr_val_cnt++} = vy;
else
error ("only two or zero output arguments supported")
endif
endfunction

```

APPENDIX B. SUPPLEMENTARY MOVIES

Description of supplementary movies on twisting mechanical metamaterials (TMMs) and unlisted YouTube links.

Movie S1. Compression-twist coupling in a unidirectional TMM with $n = 2$, $m = 8$, $\varphi = 12.5^\circ$, $\alpha_d = 90$ mm: experimental characterization (left) and FEA simulation (right). The experiment was performed at a compression rate of 1 mm/min, and is sped up 100 times in the movie. <https://youtu.be/PDNaZViLWEo>

Movie S2. Compression-twist coupling in a bidirectional TMM with $n = 2$, $m = 8$, $\varphi = 18^\circ$, $\alpha_d = 30$ mm: experimental characterization (left) and FEA simulation (right). The experiment was performed at a compression rate of 1 mm/min, and is sped up 150 times in the movie. https://youtu.be/C5ABeZm_xn4

Movie S3. Spatiotemporal evolution of Poisson's ratio of TMMs with $n = 2$, as a function of α_d and φ . <https://youtu.be/Ll9Lxs3yBe8>

Movie S4. Compression-twist coupling in a unidirectional TMM with $n = 1$, $m = 8$, $\varphi = 12^\circ$, $\alpha_d = 160$ mm: experimental characterization (left) and FEA simulation (right). The experiment was performed at a compression rate of 1 mm/min, and is sped up 200 times in the movie. <https://youtu.be/Y1fe2aXbzKM>

Movie S5. Compression-twist coupling in a bidirectional TMM with $n = 1$, $m = 8$, $\varphi = 12^\circ$, $\alpha_d = 60$ mm: experimental characterization (left) and FEA simulation (right). The experiment was performed at a compression rate of 1 mm/min, and is sped up 100 times in the movie. https://youtu.be/aCOzcE_5Ob0

REFERENCES

1. Costas M. Soukoulis and Martin Wegener. [Past achievements and future challenges in the development of three-dimensional photonic metamaterials](#). *Nature Photonics*, 5(9):523–530, 2011.
2. Johan Christensen, Muamer Kadic, Oliver Kraft, and Martin Wegener. [Vibrant times for mechanical metamaterials](#). *MRS Communications*, 5(3):453–462, 2015.
3. Steven A. Cummer, Johan Christensen, and Andrea Alù. [Controlling sound with acoustic metamaterials](#). *Nature Reviews Materials*, 1(3):16001, 2016.
4. Robert Schittny, Muamer Kadic, Sebastien Guenneau, and Martin Wegener. [Experiments on Transformation Thermodynamics: Molding the Flow of Heat](#). *Physical Review Letters*, 110(19):195901, 2013.
5. Shulin Sun, Kuang-Yu Yang, Chih-Ming Wang, Ta-Ko Juan, Wei Ting Chen, Chun Yen Liao, Qiong He, Shiyi Xiao, Wen-Ting Kung, Guang-Yu Guo, Lei Zhou, and Din Ping Tsai. [High-Efficiency Broadband Anomalous Reflection by Gradient Meta-Surfaces](#). *Nano Letters*, 12(12):6223–6229, 2012.
6. Nathaniel K. Grady, Jane E. Heyes, Dibakar Roy Chowdhury, Yong Zeng, Matthew T. Reiten, Abul K. Azad, Antoinette J. Taylor, D. A. R. Dalvit, and H.-T. Chen. [Terahertz Metamaterials for Linear Polarization Conversion and Anomalous Refraction](#). *Science*, 340(6138):1304–1307, 2013.
7. N. I. Landy, S. Sajuyigbe, J. J. Mock, D. R. Smith, and W. J. Padilla. [Perfect Metamaterial Absorber](#). *Physical Review Letters*, 100(20):207402, 2008.
8. Tapashree Roy, Edward T. F. Rogers, and Nikolay I. Zheludev. [Sub-wavelength focusing meta-lens](#). *Optics Express*, 21(6):7577, 2013.
9. Wenshan Cai and Vladimir Shalaev. *Optical Metamaterials*. Springer New York, New York, NY, 2010.
10. Katia Bertoldi, Vincenzo Vitelli, Johan Christensen, and Martin van Hecke. [Flexible mechanical metamaterials](#). *Nature Reviews Materials*, 2(11):17066, 2017.
11. Leilei Yin, Vitali K. Vlasko-Vlasov, John Pearson, Jon M. Hiller, Jiong Hua, Ulrich Welp, Dennis E. Brown, and Clyde W. Kimball. [Subwavelength Focusing and Guiding of Surface Plasmons](#). *Nano Letters*, 5(7):1399–1402, 2005.
12. Vincenzo Giannini, Antonio I. Fernandez-Dominguez, Susannah C. Heck, and Stefan A. Maier. [Plasmonic Nanoantennas: Fundamentals and Their Use in Controlling the Radiative Properties of Nanoemitters](#). *Chemical Reviews*, 111(6):3888–3912, 2011.

13. Justin S White, Edward S Barnard, Jon A Schuller, Wenshan Cai, Mark L Brongersma, and Young Chul Jun. [Plasmonics for extreme light concentration and manipulation](#). *Nature Materials*, 9(3):193–204, 2010.
14. Kuang-Yu Yang, Ruggero Verre, J  r  my Butet, Chen Yan, Tomasz J. Antosiewicz, Mikael K  ll, and Olivier J. F. Martin. [Wavevector-Selective Nonlinear Plasmonic Meta-surfaces](#). *Nano Letters*, 17(9):5258–5263, 2017.
15. Ekmel Ozbay. [Plasmonics: Merging Photonics and Electronics at Nanoscale Dimensions](#). *Science*, 311(5758):189–193, 2006.
16. Michele Dipalo, Hayder Amin, Laura Lovato, Fabio Moia, Valeria Caprettini, Gabriele C. Messina, Francesco Tantussi, Luca Berdondini, and Francesco De Angelis. [Intracellular and Extracellular Recording of Spontaneous Action Potentials in Mammalian Neurons and Cardiac Cells with 3D Plasmonic Nanoelectrodes](#). *Nano Letters*, 17(6):3932–3939, 2017.
17. Jeffrey N Anker, W Paige Hall, Olga Lyandres, Nilam C Shah, Jing Zhao, and Richard P Van Duyne. [Biosensing with plasmonic nanosensors](#). *Nature Materials*, 7(6):442–453, 2008.
18. Oren Lotan, Jonathan Bar-David, Cameron L.C. Smith, Sharon Yagur-Kroll, Shimshon Belkin, Anders Kristensen, and Uriel Levy. [Nanoscale Plasmonic V-Groove Waveguides for the Interrogation of Single Fluorescent Bacterial Cells](#). *Nano Letters*, 17(9):5481–5488, 2017.
19. Y Lei, W Cai, and G Wilde. [Highly ordered nanostructures with tunable size, shape and properties: A new way to surface nano-patterning using ultra-thin alumina masks](#). *Progress in Materials Science*, 52(4):465–539, 2007.
20. Keith J. Morton, Gregory Nieberg, Shufeng Bai, and Stephen Y. Chou. [Wafer-scale patterning of sub-40 nm diameter and high aspect ratio \(>50:1\) silicon pillar arrays by nanoimprint and etching](#). *Nanotechnology*, 19(34):345301, 2008.
21. Dong Qin, Younan Xia, and George M. Whitesides. [Soft lithography for micro- and nanoscale patterning](#). *Nature Protocols*, 5(3):491–502, 2010.
22. Estela Baquedano, Ramses Martinez, Jos   Llorens, and Pablo Postigo. [Fabrication of Silicon Nanobelts and Nanopillars by Soft Lithography for Hydrophobic and Hydrophilic Photonic Surfaces](#). *Nanomaterials*, 7(5):109, 2017.
23. Darren J Lipomi, Ramses V Martinez, Mikhail A Kats, Sung H Kang, Philseok Kim, Joanna Aizenberg, Federico Capasso, and George M Whitesides. [Patterning the Tips of Optical Fibers with Metallic Nanostructures Using Nanoskiving](#). *Nano Letters*, 11(2):632–636, 2011.
24. Markus Leitgeb, Dieter Nees, Stephan Ruttloff, Ursula Palfinger, Johannes G  tz, Robert Liska, Maria R. Beleggratis, and Barbara Stadlober. [Multilength Scale Patterning of Functional Layers by Roll-to-Roll Ultraviolet-Light-Assisted Nanoimprint Lithography](#). *ACS Nano*, 10(5):4926–4941, 2016.
25. Byron D. Gates, Qiaobing Xu, J. Christopher Love, Daniel B. Wolfe, and George M. Whitesides. [Unconventional Nanofabrication](#). *Annual Review of Materials Research*, 34(1):339–372, 2004.
26. Colin Stuart and Yong Chen. [Roll in and Roll out: A Path to High-Throughput Nanoimprint Lithography](#). *ACS Nano*, 3(8):2062–2064, 2009.

27. D.J. Lipomi, R.V. Martinez, L. Cademartiri, and G.M. Whitesides. [Soft Lithographic Approaches to Nanofabrication](#). In *Polymer Science: A Comprehensive Reference*, volume 7, pages 211–231. Elsevier, 2012.
28. Nazrin Kooy, Khairudin Mohamed, Lee Pin, and Ooi Guan. [A review of roll-to-roll nanoimprint lithography](#). *Nanoscale Research Letters*, 9(1):320, 2014.
29. Douglas J. Resnick, S.V. Sreenivasan, and C. Grant Willson. [Step & flash imprint lithography](#). *Materials Today*, 8(2):34–42, 2005.
30. Se Hyun Ahn and L. Jay Guo. [Large-Area Roll-to-Roll and Roll-to-Plate Nanoimprint Lithography: A Step toward High-Throughput Application of Continuous Nanoimprinting](#). *ACS Nano*, 3(8):2304–2310, 2009.
31. T.C. Chong, M.H. Hong, and L.P. Shi. [Laser precision engineering: from microfabrication to nanoprocessing](#). *Laser & Photonics Reviews*, 4(1):123–143, 2010.
32. M.J Jackson and W O'Neill. [Laser micro-drilling of tool steel using Nd:YAG lasers](#). *Journal of Materials Processing Technology*, 142(2):517–525, 2003.
33. R. Biswas, A.S. Kuar, S. Sarkar, and S. Mitra. [A parametric study of pulsed Nd:YAG laser micro-drilling of gamma-titanium aluminide](#). *Optics & Laser Technology*, 42(1):23–31, 2010.
34. A.S. Kuar, B. Doloi, and B. Bhattacharyya. [Modelling and analysis of pulsed Nd:YAG laser machining characteristics during micro-drilling of zirconia \(ZrO₂\)](#). *International Journal of Machine Tools and Manufacture*, 46(12-13):1301–1310, 2006.
35. Jose Mathew, G.L. Goswami, N. Ramakrishnan, and N.K. Naik. [Parametric studies on pulsed Nd:YAG laser cutting of carbon fibre reinforced plastic composites](#). *Journal of Materials Processing Technology*, 89-90:198–203, 1999.
36. K. Abdel Ghany and M. Newshy. [Cutting of 1.2mm thick austenitic stainless steel sheet using pulsed and CW Nd:YAG laser](#). *Journal of Materials Processing Technology*, 168(3):438–447, 2005.
37. X. Cao, M. Jahazi, J.P. Immarigeon, and W. Wallace. [A review of laser welding techniques for magnesium alloys](#). *Journal of Materials Processing Technology*, 171(2):188–204, 2006.
38. Bappa Acherjee, Dipten Misra, Dipankar Bose, and K. Venkadeshwaran. [Prediction of weld strength and seam width for laser transmission welding of thermoplastic using response surface methodology](#). *Optics & Laser Technology*, 41(8):956–967, 2009.
39. T. Sameshima, S. Usui, and M. Sekiya. [XeCl Excimer laser annealing used in the fabrication of poly-Si TFT's](#). *IEEE Electron Device Letters*, 7(5):276–278, 1986.
40. K Sera, F Okumura, H Uchida, S Itoh, S Kaneko, and K Hotta. [High-performance TFTs fabricated by XeCl excimer laser annealing of hydrogenated amorphous-silicon film](#). *IEEE transactions on electron devices*, 36(8931490):2868–2872, 1989.
41. M.T Khorasani, H. Mirzadeh, and P.G Sammes. [Laser surface modification of polymers to improve biocompatibility: HEMA grafted PDMS, in vitro assay—III](#). *Radiation Physics and Chemistry*, 55(5-6):685–689, 1999.
42. M.T. Khorasani, H. Mirzadeh, and P.G. Sammes. [Laser induced surface modification of polydimethylsiloxane as a super-hydrophobic material](#). *Radiation Physics and Chemistry*, 47(6):881–888, 1996.

43. Girish Chitnis, Zhenwen Ding, Chun-Li Chang, Cagri A. Savran, and Babak Ziaie. [Laser-treated Parchment Paper: An Inexpensive Microfluidic Platform](#). *MRS Proceedings*, 1346(6):mrss11–1346–aa05–03, 2011.
44. Kyoo-Chul Park, Hyungryul J. Choi, Chih-Hao Chang, Robert E. Cohen, Gareth H. McKinley, and George Barbastathis. [Nanotextured Silica Surfaces with Robust Superhydrophobicity and Omnidirectional Broadband Supertransmissivity](#). *ACS Nano*, 6(5):3789–3799, 2012.
45. L. Lu, M.O. Lai, Q. Xie, M.H. Hong, H.L. Tan, G.X. Chen, L.P. Shi, and T.C. Chong. [Fabrication of nanostructures with laser interference lithography](#). *Journal of Alloys and Compounds*, 449(1):261–264, 2008.
46. J.-H. Jang, C. K. Ullal, M. Maldovan, T. Gorishnyy, S. Kooi, C. Koh, and E. L. Thomas. [3D Micro- and Nanostructures via Interference Lithography](#). *Advanced Functional Materials*, 17(16):3027–3041, 2007.
47. Huang Gao, Yaowu Hu, Yi Xuan, J. Li, Yingling Yang, Ramses V. Martinez, Chunyu Li, Jian Luo, Minghao Qi, and Gary J. Cheng. [Large-scale nanoshaping of ultrasmooth 3D crystalline metallic structures](#). *Science*, 346(6215):1352–1356, 2014.
48. Yaowu Hu, Prashant Kumar, Rong Xu, Kejie Zhao, and Gary J. Cheng. [Ultrafast direct fabrication of flexible substrate-supported designer plasmonic nanoarrays](#). *Nanoscale*, 8(1):172–182, 2016.
49. Panagiotis Polygerinos, Nikolaus Correll, Stephen A. Morin, Bobak Mosadegh, Cagdas D. Onal, Kirstin Petersen, Matteo Cianchetti, Michael T. Tolley, and Robert F. Shepherd. [Soft Robotics: Review of Fluid-Driven Intrinsically Soft Devices; Manufacturing, Sensing, Control, and Applications in Human-Robot Interaction](#). *Advanced Engineering Materials*, 19(12):1700016, 2017.
50. Ramses V. Martinez, Jamie L. Branch, Carina R. Fish, Lihua Jin, Robert F. Shepherd, Rui M. D. Nunes, Zhigang Suo, and George M. Whitesides. [Robotic Tentacles with Three-Dimensional Mobility Based on Flexible Elastomers](#). *Advanced Materials*, 25(2):205–212, 2013.
51. Ramses Valentin Martinez, Ana C. Glavan, Christoph Keplinger, Alexis I. Oyetibo, and George M. Whitesides. [Soft Actuators and Robots that Are Resistant to Mechanical Damage](#). *Advanced Functional Materials*, 24(20):3003–3010, 2014.
52. R. F. Shepherd, F. Ilievski, W. Choi, S. A. Morin, A. A. Stokes, A. D. Mazzeo, X. Chen, M. Wang, and G. M. Whitesides. [Multigait soft robot](#). *Proceedings of the National Academy of Sciences*, 108(51):20400–20403, 2011.
53. Ming Luo, Ruibo Yan, Zhenyu Wan, Yun Qin, Junius Santoso, Erik H Skorina, and Cagdas D Onal. [OriSnake: Design, Fabrication, and Experimental Analysis of a 3-D Origami Snake Robot](#). *IEEE Robotics and Automation Letters*, 3(3):1993–1999, 2018.
54. Nicholas W. Bartlett, Michael T. Tolley, J. T. B. Overvelde, James C. Weaver, Bobak Mosadegh, Katia Bertoldi, George M. Whitesides, and Robert J. Wood. [A 3D-printed, functionally graded soft robot powered by combustion](#). *Science*, 349(6244):161–165, 2015.
55. Huai-Ti Lin, Gary G. Leisk, and Barry Trimmer. [GoQBot: a caterpillar-inspired soft-bodied rolling robot](#). *Bioinspiration & Biomimetics*, 6(2):026007, 2011.

56. Elliot W. Hawkes, Laura H. Blumenschein, Joseph D. Greer, and Allison M. Okamura. [A soft robot that navigates its environment through growth](#). *Science Robotics*, 2(8):eaan3028, 2017.
57. Jennifer C. Case, Edward L. White, and Rebecca K. Kramer. [Sensor enabled closed-loop bending control of soft beams](#). *Smart Materials and Structures*, 25(4):045018, 2016.
58. Daniela Rus and Michael T. Tolley. [Design, fabrication and control of soft robots](#). *Nature*, 521(7553):467–475, 2015.
59. Sen W. Kwok, Stephen A. Morin, Bobak Mosadegh, Ju-Hee So, Robert F. Shepherd, Ramses V. Martinez, Barbara Smith, Felice C. Simeone, Adam A. Stokes, and George M. Whitesides. [Magnetic Assembly of Soft Robots with Hard Components](#). *Advanced Functional Materials*, 24(15):2180–2187, 2014.
60. Christian Schumacher, Bernd Bickel, Jan Rys, Steve Marschner, Chiara Daraio, and Markus Gross. [Microstructures to control elasticity in 3D printing](#). *ACM Transactions on Graphics*, 34(4):136:1–136:13, 2015.
61. Jonàs Martínez, Samuel Hornus, Haichuan Song, and Sylvain Lefebvre. [Polyhedral voronoi diagrams for additive manufacturing](#). *ACM Transactions on Graphics*, 37(4):1–15, 2018.
62. Jonàs Martínez, Jérémie Dumas, and Sylvain Lefebvre. [Procedural voronoi foams for additive manufacturing](#). *ACM Transactions on Graphics*, 35(4):1–12, 2016.
63. Katia Bertoldi, Pedro M. Reis, Stephen Willshaw, and Tom Mullin. [Negative Poisson’s Ratio Behavior Induced by an Elastic Instability](#). *Advanced Materials*, 22(3):361–366, 2010.
64. Roderic S. Lakes. [Negative-Poisson’s-Ratio Materials: Auxetic Solids](#). *Annual Review of Materials Research*, 47(1):63–81, 2017.
65. Sahab Babae, Jongmin Shim, James C. Weaver, Elizabeth R. Chen, Nikita Patel, and Katia Bertoldi. [3D Soft Metamaterials with Negative Poisson’s Ratio](#). *Advanced Materials*, 25(36):5044–5049, 2013.
66. Sicong Shan, Sung H. Kang, Jordan R. Raney, Pai Wang, Lichen Fang, Francisco Candido, Jennifer A. Lewis, and Katia Bertoldi. [Multistable Architected Materials for Trapping Elastic Strain Energy](#). *Advanced Materials*, 27(29):4296–4301, 2015.
67. Kaikai Che, Chao Yuan, Jiangtao Wu, H. Jerry Qi, and Julien Meaud. [Three-Dimensional-Printed Multistable Mechanical Metamaterials With a Deterministic Deformation Sequence](#). *Journal of Applied Mechanics*, 84(1):011004, 2016.
68. Dian Yang, Lihua Jin, Ramses Valentin Martinez, Katia Bertoldi, George M. Whitesides, and Zhigang Suo. [Phase-transforming and switchable metamaterials](#). *Extreme Mechanics Letters*, 6:1–9, 2016.
69. Yoonho Kim, Hyunwoo Yuk, Ruike Zhao, Shawn A Chester, and Xuanhe Zhao. [Printing ferromagnetic domains for untethered fast-transforming soft materials](#). *Nature*, 558(7709):274–279, 2018.
70. Corentin Coulais, Eial Teomy, Koen de Reus, Yair Shokef, and Martin van Hecke. [Combinatorial design of textured mechanical metamaterials](#). *Nature*, 535(7613):529–532, 2016.

71. Christoph Keplinger, Tiefeng Li, Richard Baumgartner, Zhigang Suo, and Siegfried Bauer. [Harnessing snap-through instability in soft dielectrics to achieve giant voltage-triggered deformation](#). *Soft Matter*, 8(2):285–288, 2012.
72. Xuanhe Zhao and Qiming Wang. [Harnessing large deformation and instabilities of soft dielectrics: Theory, experiment, and application](#). *Applied Physics Reviews*, 1(2):021304, 2014.
73. Yihui Zhang, Sheng Xu, Haoran Fu, Juhwan Lee, Jessica Su, Keh-Chih Hwang, John A. Rogers, and Yonggang Huang. [Buckling in serpentine microstructures and applications in elastomer-supported ultra-stretchable electronics with high areal coverage](#). *Soft Matter*, 9(33):8062, 2013.
74. Stéphanie Périchon Lacour, Sigurd Wagner, Zhenyu Huang, and Z. Suo. [Stretchable gold conductors on elastomeric substrates](#). *Applied Physics Letters*, 82(15):2404–2406, 2003.
75. Dian Yang, Mohit S. Verma, Ju-Hee So, Bobak Mosadegh, Christoph Keplinger, Benjamin Lee, Fatemeh Khashai, Elton Lossner, Zhigang Suo, and George M. Whitesides. [Buckling Pneumatic Linear Actuators Inspired by Muscle](#). *Advanced Materials Technologies*, 1(3):1600055, 2016.
76. Dian Yang, Bobak Mosadegh, Alar Ainla, Benjamin Lee, Fatemeh Khashai, Zhigang Suo, Katia Bertoldi, and George M. Whitesides. [Buckling of Elastomeric Beams Enables Actuation of Soft Machines](#). *Advanced Materials*, 27(41):6323–6327, 2015.
77. Alar Ainla, Mohit S. Verma, Dian Yang, and George M. Whitesides. [Soft, Rotating Pneumatic Actuator](#). *Soft Robotics*, 4(3):297–304, 2017.
78. Nicholas Kellaris, Vidyacharan Gopaluni Venkata, Garrett M. Smith, Shane K. Mitchell, and Christoph Keplinger. [Peano-HASEL actuators: Muscle-mimetic, electrohydraulic transducers that linearly contract on activation](#). *Science Robotics*, 3(14):eaar3276, 2018.
79. Caleb Christianson, Nathaniel N. Goldberg, Dimitri D. Deheyn, Shengqiang Cai, and Michael T. Tolley. [Translucent soft robots driven by frameless fluid electrode dielectric elastomer actuators](#). *Science Robotics*, 3(17):eaat1893, 2018.
80. Yousef Bahramzadeh and Mohsen Shahinpoor. [A Review of Ionic Polymeric Soft Actuators and Sensors](#). *Soft Robotics*, 1(1):38–52, 2014.
81. Wenqi Hu, Guo Zhan Lum, Massimo Mastrangeli, and Metin Sitti. [Small-scale soft-bodied robot with multimodal locomotion](#). *Nature*, 554(7690):81–85, 2018.
82. Vishesh Vikas, Eliad Cohen, Rob Grassi, Canberk Sozer, and Barry Trimmer. [Design and Locomotion Control of a Soft Robot Using Friction Manipulation and Motor–Tendon Actuation](#). *IEEE Transactions on Robotics*, 32(4):949–959, 2016.
83. Cecilia Laschi and Matteo Cianchetti. [Soft Robotics: New Perspectives for Robot Bodyware and Control](#). *Frontiers in Bioengineering and Biotechnology*, 2, 2014.
84. Junyong Park, Shuodao Wang, Ming Li, Changui Ahn, Jerome K. Hyun, Dong Seok Kim, Do Kyung Kim, John A. Rogers, Yonggang Huang, and Seokwoo Jeon. [Three-dimensional nanonetworks for giant stretchability in dielectrics and conductors](#). *Nature Communications*, 3(1):916, 2012.

85. Robert K. Katzschmann, Joseph DelPreto, Robert MacCurdy, and Daniela Rus. [Exploration of underwater life with an acoustically controlled soft robotic fish](#). *Science Robotics*, 3(16):eaar3449, 2018.
86. Benjamin C. Mac Murray, Xintong An, Sanlin S. Robinson, Ilse M. van Meerbeek, Kevin W. O'Brien, Huichan Zhao, and Robert F. Shepherd. [Poroelastic Foams for Simple Fabrication of Complex Soft Robots](#). *Advanced Materials*, 27(41):6334–6340, 2015.
87. Eric B. Duoss, Todd H. Weisgraber, Keith Hearon, Cheng Zhu, Ward Small, Thomas R. Metz, John J. Vericella, Holly D. Barth, Joshua D. Kuntz, Robert S. Maxwell, Christopher M. Spadaccini, and Thomas S. Wilson. [Three-Dimensional Printing of Elastomeric, Cellular Architectures with Negative Stiffness](#). *Advanced Functional Materials*, 24(31):4905–4913, 2014.
88. T. J. Wallin, J. Pikul, and R. F. Shepherd. [3D printing of soft robotic systems](#). *Nature Reviews Materials*, 3(6):84–100, 2018.
89. Farhang Momeni, Seyed M. Mehdi Hassani, Xun Liu, and Jun Ni. [A review of 4D printing](#). *Materials & Design*, 122:42–79, 2017.
90. Dinesh K. Patel, Amir Hosein Sakhaei, Michael Layani, Biao Zhang, Qi Ge, and Shlomo Magdassi. [Highly Stretchable and UV Curable Elastomers for Digital Light Processing Based 3D Printing](#). *Advanced Materials*, 29(15):1606000, 2017.
91. Jiayu Liu, Ozan Erol, Aishwarya Pantula, Wangqu Liu, Zhuoran Jiang, Kunihiko Kobayashi, Devina Chatterjee, Narutoshi Hibino, Lewis H. Romer, Sung Hoon Kang, Thao D. Nguyen, and David H. Gracias. [Dual-Gel 4D Printing of Bioinspired Tubes](#). *ACS Applied Materials & Interfaces*, 11(8):8492–8498, 2019.
92. Arnold Sommerfeld. *Mechanics of Deformable Bodies: Lectures on Theoretical Physics, Volume II*. Academic Press, New York, 1950.
93. Tobias Frenzel, Muamer Kadic, and Martin Wegener. [Three-dimensional mechanical metamaterials with a twist](#). *Science*, 358(6366):1072–1074, 2017.
94. Wei Chen, Dong Ruan, and Xiaodong Huang. [Optimization for twist chirality of structural materials induced by axial strain](#). *Materials Today Communications*, 15:175–184, jun 2018.
95. Chao Ma, Hongshuai Lei, Jun Liang, Wenwang Wu, Tiejun Wang, and Daining Fang. [Macroscopic mechanical response of chiral-type cylindrical metastructures under axial compression loading](#). *Materials & Design*, 158:198–212, nov 2018.
96. Chao Ma, Hongshuai Lei, Jian Hua, Yingchun Bai, Jun Liang, and Daining Fang. [Experimental and simulation investigation of the reversible bi-directional twisting response of tetra-chiral cylindrical shells](#). *Composite Structures*, 203:142–152, nov 2018.
97. David T. Farrell, Conor McGinn, and Gareth J. Bennett. [Extension twist deformation response of an auxetic cylindrical structure inspired by deformed cell ligaments](#). *Composite Structures*, 238:111901, apr 2020.
98. Wenwang Wu, Luchao Geng, Yinghao Niu, Dexing Qi, Xinguang Cui, and Daining Fang. [Compression twist deformation of novel tetrachiral architected cylindrical tube inspired by towel gourd tendrils](#). *Extreme Mechanics Letters*, 20:104–111, apr 2018.

99. Bin-Bin Zheng, Rong-Chang Zhong, Xuan Chen, Ming-Hui Fu, and Ling-Ling Hu. [A novel metamaterial with tension-torsion coupling effect.](#) *Materials & Design*, 171:107700, jun 2019.
100. Rongchang Zhong, Minghui Fu, Xuan Chen, Binbin Zheng, and Lingling Hu. [A novel three-dimensional mechanical metamaterial with compression-torsion properties.](#) *Composite Structures*, 226:111232, oct 2019.
101. Rongchang Zhong, Minghui Fu, Qiuyun Yin, Outeng Xu, and Lingling Hu. [Special characteristics of tetrachiral honeycombs under large deformation.](#) *International Journal of Solids and Structures*, 169:166–176, sep 2019.
102. Debkalpa Goswami, Juan C. Munera, Aniket Pal, Behnam Sadri, Caio Lui P. G. Scarpetti, and Ramses V Martinez. [Roll-to-Roll Nanofforming of Metals Using Laser-Induced Superplasticity.](#) *Nano Letters*, 18(6):3616–3622, 2018.
103. William Steen and Jyotirmoy Mazumder. *Laser Material Processing*. Springer, London, 4 edition, 2010.
104. J. Wang. [An Experimental Analysis and Optimisation of the CO2 Laser Cutting Process for Metallic Coated Sheet Steels.](#) *The International Journal of Advanced Manufacturing Technology*, 16(5):334–340, 2000.
105. J. N. Gonsalves and W. W. Duley. [Cutting thin metal sheets with the cw CO2 laser.](#) *Journal of Applied Physics*, 43(11):4684–4687, 1972.
106. Bernard Lobel, Ophir Eyal, Noam Kariv, and Abraham Katzir. [Temperature controlled CO2 laser welding of soft tissues: Urinary bladder welding in different animal models \(rats, rabbits, and cats\).](#) *Lasers in Surgery and Medicine*, 26(1):4–12, 2000.
107. Naoki Seto, Seiji Katayama, and Akira Matsunawa. [High-speed simultaneous observation of plasma and keyhole behavior during high power CO2 laser welding: Effect of shielding gas on porosity formation.](#) *Journal of Laser Applications*, 12(6):245–250, 2000.
108. C. W. Kan, C W M Yuen, and C. W. Cheng. [Technical study of the effect of CO2 laser surface engraving on the colour properties of denim fabric.](#) *Coloration Technology*, 126(6):365–371, 2010.
109. Hao-Bing Liu and Hai-Qing Gong. [Templateless prototyping of polydimethylsiloxane microfluidic structures using a pulsed CO2 laser.](#) *Journal of Micromechanics and Microengineering*, 19(3):037002, 2009.
110. C. K. Chung, Y. C. Lin, and G. R. Huang. [Bulge formation and improvement of the polymer in CO 2 laser micromachining.](#) *Journal of Micromechanics and Microengineering*, 15(10):1878–1884, 2005.
111. Detlef Snakenborg, Henning Klank, and Jörg P Kutter. [Microstructure fabrication with a CO2 laser system.](#) *Journal of Micromechanics and Microengineering*, 14(2):182–189, 2004.
112. Manabu Kato. [Preparation of Ultrafine Particles of Refractory Oxides by Gas-Evaporation Method.](#) *Japanese Journal of Applied Physics*, 15(5):757–760, 1976.
113. J C M Marijnissen and Sotiris M Pratsinis. *Synthesis and Measurement of Ultrafine Particles*. Delft University Press, Delft, Netherlands, 1 edition, 1993.

114. R. Fabbro, J. Fournier, P. Ballard, D. Devaux, and J. Virmont. [Physical study of laser-produced plasma in confined geometry](#). *Journal of Applied Physics*, 68(2):775–784, 1990.
115. Yaowu Hu, Yi Xuan, Xiaolei Wang, Biwei Deng, Mojib Saei, Shengyu Jin, Joseph Irudayaraj, and Gary J. Cheng. [Superplastic Formation of Metal Nanostructure Arrays with Ultrafine Gaps](#). *Advanced Materials*, 28(41):9152–9162, 2016.
116. Huang Gao and Gary J. Cheng. [Laser-Induced High-Strain-Rate Superplastic 3-D Microforming of Metallic Thin Films](#). *Journal of Microelectromechanical Systems*, 19(2):273–281, 2010.
117. C. Y. Hui, A. Jagota, Y. Y. Lin, and E. J. Kramer. [Constraints on Microcontact Printing Imposed by Stamp Deformation](#). *Langmuir*, 18(4):1394–1407, 2002.
118. Y. Li, H. W. Ng, B. D. Gates, and C. Menon. [Material versatility using replica molding for large-scale fabrication of high aspect-ratio, high density arrays of nano-pillars](#). *Nanotechnology*, 25(28):285303, 2014.
119. Sergey I. Bozhevolnyi, Valentyn S. Volkov, Eloïse Devaux, and Thomas W. Ebbesen. [Channel Plasmon-Polariton Guiding by Subwavelength Metal Grooves](#). *Physical Review Letters*, 95(4):046802, 2005.
120. Sergey S. Kruk, Zi Jing Wong, Ekaterina Pshenay-Severin, Kevin O’Brien, Dragomir N. Neshev, Yuri S. Kivshar, and Xiang Zhang. [Magnetic hyperbolic optical metamaterials](#). *Nature Communications*, 7(1):11329, 2016.
121. Niels Hansen. [Hall–Petch relation and boundary strengthening](#). *Scripta Materialia*, 51(8):801–806, 2004.
122. Jakob Schiøtz, Francesco D. Di Tolla, and Karsten W. Jacobsen. [Softening of nanocrystalline metals at very small grain sizes](#). *Nature*, 391(6667):561–563, 1998.
123. Anastasiya Derkachova, Krystyna Kolwas, and Iraida Demchenko. [Dielectric Function for Gold in Plasmonics Applications: Size Dependence of Plasmon Resonance Frequencies and Damping Rates for Nanospheres](#). *Plasmonics*, 11(3):941–951, 2016.
124. Chris B Schaffer, André Brodeur, and Eric Mazur. [Laser-induced breakdown and damage in bulk transparent materials induced by tightly focused femtosecond laser pulses](#). *Measurement Science and Technology*, 12(11):1784–1794, 2001.
125. Dongkyun Kang, Ramses V. Martinez, George M. Whitesides, and Guillermo J. Tearney. [Miniature grating for spectrally-encoded endoscopy](#). *Lab on a Chip*, 13(9):1810, 2013.
126. Douglas C Watson, Ramses V Martinez, Yannik Fontana, Eleonora Russo-Averchi, Martin Heiss, Anna Fontcuberta i Morral, George M Whitesides, and Marko Lončar. [Nanoskiving Core–Shell Nanowires: A New Fabrication Method for Nano-optics](#). *Nano Letters*, 14(2):524–531, 2014.
127. John E. Sader, Julian A. Sanelli, Brian D. Adamson, Jason P. Monty, Xingzhan Wei, Simon A. Crawford, James R. Friend, Ivan Marusic, Paul Mulvaney, and Evan J. Bieske. [Spring constant calibration of atomic force microscope cantilevers of arbitrary shape](#). *Review of Scientific Instruments*, 83(10):103705, 2012.
128. John E Sader, James W M Chon, and Paul Mulvaney. [Calibration of rectangular atomic force microscope cantilevers](#). *Review of Scientific Instruments*, 70(10):3967–3969, 1999.

129. Hans-Jürgen Butt, Brunero Cappella, and Michael Kappl. [Force measurements with the atomic force microscope: Technique, interpretation and applications.](#) *Surface Science Reports*, 59(1):1–152, 2005.
130. Yuri M. Efremov, Wen-Horng Wang, Shana D. Hardy, Robert L. Geahlen, and Arvind Raman. [Measuring nanoscale viscoelastic parameters of cells directly from AFM force-displacement curves.](#) *Scientific Reports*, 7(1):1541, 2017.
131. K. L. Johnson. *Contact Mechanics*. Cambridge University Press, Cambridge, 1st edition, 1985.
132. Lucia Morales-Rivas, Alejandro González-Orive, Carlos Garcia-Mateo, Alberto Hernández-Creus, Francisca G. Caballero, and Luis Vázquez. [Nanomechanical characterization of nanostructured bainitic steel: Peak Force Microscopy and Nanoindentation with AFM.](#) *Scientific Reports*, 5(1):17164, 2015.
133. Steve Plimpton. [Fast Parallel Algorithms for Short-Range Molecular Dynamics.](#) *Journal of Computational Physics*, 117(1):1–19, 1995.
134. J. Tersoff. [New empirical approach for the structure and energy of covalent systems.](#) *Physical Review B*, 37(12):6991–7000, 1988.
135. S. M. Foiles, M. I. Baskes, and M. S. Daw. [Embedded-atom-method functions for the fcc metals Cu, Ag, Au, Ni, Pd, Pt, and their alloys.](#) *Physical Review B*, 33(12):7983–7991, 1986.
136. S M Foiles, M I Baskes, and M S Daw. [Erratum: Embedded-atom-method functions for the fcc metals Cu, Ag, Au, Ni, Pd, Pt, and their alloys.](#) *Physical Review B*, 37(17):10378–10378, 1988.
137. A. V. Raghunathan, J. H. Park, and N. R. Aluru. [Interatomic potential-based semiclassical theory for Lennard-Jones fluids.](#) *The Journal of Chemical Physics*, 127(17):174701, 2007.
138. Qing Pu, Yongsheng Leng, Xiongce Zhao, and Peter T. Cummings. [Molecular simulations of stretching gold nanowires in solvents.](#) *Nanotechnology*, 18(42):424007, 2007.
139. Daan Frenkel and Berend Smit. Molecular Dynamics Simulations. In *Understanding Molecular Simulation*, pages 63–107. Elsevier, New York, 2nd edition, 2002.
140. John David Anderson. *Fundamentals of Aerodynamics*. McGraw-Hill, Inc., New York, 2nd edition, 1984.
141. Alexander Stukowski. [Visualization and analysis of atomistic simulation data with OVITO—the Open Visualization Tool.](#) *Modelling and Simulation in Materials Science and Engineering*, 18(1):015012, 2010.
142. R D Griffin, B L Justus, A J Campillo, and L S Goldberg. [Interferometric studies of the pressure of a confined laser-heated plasma.](#) *Journal of Applied Physics*, 59(6):1968–1971, 1986.
143. Gordon R Johnson and William H Cook. [Fracture characteristics of three metals subjected to various strains, strain rates, temperatures and pressures.](#) *Engineering Fracture Mechanics*, 21(1):31–48, 1985.

144. Darren J. Lipomi, Mikhail A. Kats, Philseok Kim, Sung H. Kang, Joanna Aizenberg, Federico Capasso, and George M. Whitesides. [Fabrication and Replication of Arrays of Single- or Multicomponent Nanostructures by Replica Molding and Mechanical Sectioning](#). *ACS Nano*, 4(7):4017–4026, 2010.
145. Prashant Nagpal, Nathan C Lindquist, Sang-Hyun Oh, and David J Norris. [Ultra-smooth patterned metals for plasmonics and metamaterials](#). *Science (New York, N.Y.)*, 325(5940):594–7, 2009.
146. Debkalpa Goswami, Shuai Liu, Aniket Pal, Lucas G. Silva, and Ramses V. Martinez. [3D-Architected Soft Machines with Topologically Encoded Motion](#). *Advanced Functional Materials*, 29(24):1808713, jun 2019.
147. Lili Ju, Todd Ringler, and Max Gunzburger. [Voronoi Tessellations and Their Application to Climate and Global Modeling](#). In *Numerical Techniques for Global Atmospheric Models*, pages 313–342. Springer, Berlin, Heidelberg, 2011.
148. Atsuyuki Okabe, Barry Boots, Kokichi Sugihara, and Sung Nok Chiu. [Spatial Tessellations: Concepts and Applications of Voronoi Diagrams](#). John Wiley & Sons, Ltd., Chichester, England, 2nd edition, 2009.
149. S. Rebay. [Efficient Unstructured Mesh Generation by Means of Delaunay Triangulation and Bowyer-Watson Algorithm](#). *Journal of Computational Physics*, 106(1):125–138, 1993.
150. Xiangyu Gong, Ke Yang, Jingjin Xie, Yanjun Wang, Parth Kulkarni, Alexander S. Hobbs, and Aaron D. Mazzeo. [Rotary Actuators Based on Pneumatically Driven Elastomeric Structures](#). *Advanced Materials*, 28(34):7533–7538, 2016.
151. Yugang Sun and John A. Rogers. [Structural forms of single crystal semiconductor nanoribbons for high-performance stretchable electronics](#). *Journal of Materials Chemistry*, 17(9):832, 2007.
152. Xiaoyu Zheng, Howon Lee, Todd H. Weisgraber, Maxim Shusteff, Joshua DeOtte, Eric B. Duoss, Joshua D. Kuntz, Monika M. Biener, Qi Ge, Julie A. Jackson, Sergei O. Kucheyev, Nicholas X. Fang, and Christopher M. Spadaccini. [Ultralight, ultrastiff mechanical metamaterials](#). *Science*, 344(6190):1373–1377, 2014.
153. Michael Wehner, Ryan L. Truby, Daniel J. Fitzgerald, Bobak Mosadegh, George M. Whitesides, Jennifer A. Lewis, and Robert J. Wood. [An integrated design and fabrication strategy for entirely soft, autonomous robots](#). *Nature*, 536(7617):451–455, 2016.
154. R. W. Ogden. [Large Deformation Isotropic Elasticity: On the Correlation of Theory and Experiment for Compressible Rubberlike Solids](#). *Proceedings of the Royal Society A: Mathematical, Physical and Engineering Sciences*, 328(1575):567–583, 1972.
155. Gunjan Agarwal, Nicolas Besuchet, Basile Audergon, and Jamie Paik. [Stretchable Materials for Robust Soft Actuators towards Assistive Wearable Devices](#). *Scientific Reports*, 6(1):34224, 2016.
156. C. D. Modes, M. Warner, C. Sánchez-Somolinos, L. T. de Haan, and D. Broer. [Mechanical frustration and spontaneous polygonal folding in active nematic sheets](#). *Physical Review E*, 86(6):060701, dec 2012.

157. Yu-Ki Lee, Zhonghua Xi, Young-Joo Lee, Yun-Hyeong Kim, Yue Hao, Hongjin Choi, Myoung-Gyu Lee, Young-Chang Joo, Changsoo Kim, Jyh-Ming Lien, and In-Suk Choi. [Computational wrapping: A universal method to wrap 3D-curved surfaces with nonstretchable materials for conformal devices](#). *Science Advances*, 6(15):eaax6212, apr 2020.
158. Lorna J. Gibson and Michael F. Ashby. *Cellular Solids*. Cambridge University Press, may 1997.
159. Martin Brandenbourger, Xander Locsin, Edan Lerner, and Corentin Coulais. [Non-reciprocal robotic metamaterials](#). *Nature Communications*, 10(1):4608, dec 2019.
160. Corentin Coulais, Dimitrios Sounas, and Andrea Alù. [Static non-reciprocity in mechanical metamaterials](#). *Nature*, 542(7642):461–464, feb 2017.
161. Corentin Coulais. [As the extension, so the twist](#). *Science*, 358(6366):994–995, nov 2017.
162. Alexandra Ion, Johannes Frohnhofen, Ludwig Wall, Robert Kovacs, Mirela Alistar, Jack Lindsay, Pedro Lopes, Hsiang-Ting Chen, and Patrick Baudisch. [Metamaterial Mechanisms](#). In *Proceedings of the 29th Annual Symposium on User Interface Software and Technology*, pages 529–539, New York, NY, USA, oct 2016. ACM.
163. Ahmad Rafsanjani, Katia Bertoldi, and André R. Studart. [Programming soft robots with flexible mechanical metamaterials](#). *Science Robotics*, 4(29):eaav7874, apr 2019.
164. Jordan R. Raney, Neel Nadkarni, Chiara Daraio, Dennis M. Kochmann, Jennifer A. Lewis, and Katia Bertoldi. [Stable propagation of mechanical signals in soft media using stored elastic energy](#). *Proceedings of the National Academy of Sciences*, 113(35):9722–9727, aug 2016.
165. Myungwon Hwang and Andres F. Arrieta. [Input-Independent Energy Harvesting in Bistable Lattices from Transition Waves](#). *Scientific Reports*, 8(1):3630, dec 2018.
166. Hongbin Fang, K.W. Wang, and Suyi Li. [Asymmetric energy barrier and mechanical diode effect from folding multi-stable stacked-origami](#). *Extreme Mechanics Letters*, 17:7–15, nov 2017.
167. Bolei Deng, Pai Wang, Qi He, Vincent Tournat, and Katia Bertoldi. [Metamaterials with amplitude gaps for elastic solitons](#). *Nature Communications*, 9(1):3410, dec 2018.
168. Xiao-Fei Guo and Li Ma. [One-way transmission in topological mechanical metamaterials based on self-locking](#). *International Journal of Mechanical Sciences*, 175:105555, jun 2020.
169. Ming Lei, Wei Hong, Zeang Zhao, Craig Hamel, Mingji Chen, Haibao Lu, and H. Jerry Qi. [3D Printing of Auxetic Metamaterials with Digitally Reprogrammable Shape](#). *ACS Applied Materials & Interfaces*, 11(25):22768–22776, jun 2019.
170. Muamer Kadic, Graeme W. Milton, Martin van Hecke, and Martin Wegener. [3D metamaterials](#). *Nature Reviews Physics*, 1(3):198–210, mar 2019.
171. Giorgio Oliveri and Johannes T.B. Overvelde. [Inverse Design of Mechanical Metamaterials That Undergo Buckling](#). *Advanced Functional Materials*, 30(12):1909033, mar 2020.

172. Helena M. A. Kolken, Shahram Janbaz, Sander M. A. Leeflang, Karel Lietaert, Harrie H. Weinans, and Amir A. Zadpoor. [Rationally designed meta-implants: a combination of auxetic and conventional meta-biomaterials](#). *Materials Horizons*, 5(1):28–35, 2018.
173. F. S. L. Bobbert, S. Janbaz, and A. A. Zadpoor. [Towards deployable meta-implants](#). *Journal of Materials Chemistry B*, 6(21):3449–3455, 2018.
174. Amir A. Zadpoor. [Mechanical performance of additively manufactured meta-biomaterials](#). *Acta Biomaterialia*, 85:41–59, feb 2019.
175. Wenwang Wu, Xiaoke Song, Jun Liang, Re Xia, Guian Qian, and Daining Fang. [Mechanical properties of anti-tetrachiral auxetic stents](#). *Composite Structures*, 185:381–392, feb 2018.
176. M. Azaouzi, A. Makradi, and S. Belouettar. [Deployment of a self-expanding stent inside an artery: A finite element analysis](#). *Materials & Design*, 41:410–420, oct 2012.
177. Ellen T. Roche, Robert Wohlfarth, Johannes T. B. Overvelde, Nikolay V. Vasilyev, Frank A. Pigula, David J. Mooney, Katia Bertoldi, and Conor J. Walsh. [A Bioinspired Soft Actuated Material](#). *Advanced Materials*, 26(8):1200–1206, feb 2014.
178. Ellen T. Roche, Markus A. Horvath, Isaac Wamala, Ali Alazmani, Sang-Eun Song, William Whyte, Zurab Machaidze, Christopher J. Payne, James C. Weaver, Gregory Fishbein, Joseph Kuebler, Nikolay V. Vasilyev, David J. Mooney, Frank A. Pigula, and Conor J. Walsh. [Soft robotic sleeve supports heart function](#). *Science Translational Medicine*, 9(373):eaaf3925, jan 2017.
179. Brian A. Houston, Keyur B. Shah, Mandeep R. Mehra, and Ryan J. Tedford. [A new “twist” on right heart failure with left ventricular assist systems](#). *The Journal of Heart and Lung Transplantation*, 36(7):701–707, jul 2017.
180. Aniket Pal, Debkalpa Goswami, and Ramses V. Martinez. [Elastic Energy Storage Enables Rapid and Programmable Actuation in Soft Machines](#). *Advanced Functional Materials*, 30(1):1906603, jan 2020.
181. I. Fernandez-Corbaton, C. Rockstuhl, P. Ziemke, P. Gumbsch, A. Albiez, R. Schwaiger, T. Frenzel, M. Kadic, and M. Wegener. [New Twists of 3D Chiral Metamaterials](#). *Advanced Materials*, 31(26):1807742, jun 2019.

VITA

Debkalpa Goswami was born in Kolkata, India. He completed his Bachelor's degree in Production Engineering from Jadavpur University, India, in 2015. He was awarded the European Commission's Erasmus Mundus Fellowship in 2013 and spent a year as a guest researcher at the University of Bremen, Germany, where he worked on simulation-based optimization of semiconductor manufacturing systems. He joined Purdue University as a Ross Fellow in Fall 2015 to pursue his PhD in Industrial Engineering at the FlexiLab under the supervision of Prof. Ramses V. Martinez. His research interests are in the general areas of flexible electronics, soft robotics, biomedical devices, and nanofabrication. He has (co-)authored 19 peer-reviewed journal articles and 1 book chapter.

PUBLICATIONS

[Google Scholar Profile](#)**Journal Articles**

19. C.R. Matthews, **D. Goswami**, N.K. Ramchandani, A.L. Huffard, K.M. Rieger, J.V. Young, R.V. Martinez, and K.A. Kesler: ‘[The Influence of Airway Closure Technique for Right Pneumonectomy on Wall Tension during Positive Pressure Ventilation: An Experimental Study](#)’, *Seminars in Thoracic and Cardiovascular Surgery*, 2020, in press.
18. J.C. Munera, **D. Goswami**, R.V. Martinez, and E.A. Ossa: ‘[Time-dependent Mechanical Response at the Nanoscale](#)’, *Mechanics of Materials*, 2020, 148, 103443.
17. A. Pal, V.G. Nadiger, **D. Goswami**, and R.V. Martinez: ‘[Conformal, waterproof electronic decals for wireless monitoring of sweat and vaginal pH at the point-of-care](#)’, *Biosensors and Bioelectronics*, 2020, 160, 112206.
16. A. Pal, **D. Goswami**, and R.V. Martinez: ‘[Elastic Energy Storage Enables Rapid and Programmable Actuation in Soft Machines](#)’, *Advanced Functional Materials*, 2020, 30(1), 1906603. —***Featured on the Cover*** —***Media Highlights***.
15. B.K. Mahajan, B. Choudhuri, **D. Goswami**, A.K. Tiwari, M.B. Sarkar, and A. Mondal: ‘[Enhanced Photodetection with Crystalline Si Nanoclusters](#)’, *Journal of Nanoscience and Nanotechnology*, 2020, 20(4), 2344–2350.
14. M. Sala de Medeiros, D. Chanci, C. Moreno, **D. Goswami**, and R.V. Martinez: ‘[Waterproof, Breathable, and Antibacterial Self-powered e-Textiles based on Omnipobic Triboelectric Nanogenerators](#)’, *Advanced Functional Materials*, 2019, 29(42), 1904350. —***Featured on the Cover*** —***Media Highlights***.

13. **D. Goswami**, S. Liu, A. Pal, L.G. Silva, and R.V. Martinez: ‘3D-Architected Soft Machines with Topologically Encoded Motion’, *Advanced Functional Materials*, 2019, 29(24), 1808713. — **Featured on the Cover** — **Media Highlights**.
12. B. Sadri, **D. Goswami**, M. Sala de Medeiros, A. Pal, B. Castro, S. Kuang, and R.V. Martinez: ‘Wearable and Implantable Epidermal Paper-based Electronics’, *ACS Applied Materials & Interfaces*, 2018, 10(37), 31061–31068. — **Media Highlights**.
11. B. Sadri, **D. Goswami**, and R.V. Martinez: ‘Rapid Fabrication of Epidermal Paper-Based Electronic Devices Using Razor Printing’, *Micromachines*, 2018, 9(9), 420.
10. A. Pal, **D. Goswami**, H.E. Cuellar, B. Castro, S. Kuang, and R.V. Martinez: ‘Early detection and monitoring of chronic wounds using low-cost, omniphobic paper-based smart bandages’, *Biosensors and Bioelectronics*, 2018, 117, 696–705.
9. **D. Goswami**, J.C. Munera, A. Pal, B. Sadri, C.L.P.G. Scarpetti, and R.V. Martinez: ‘Roll-to-Roll Nanoforming of Metals using Laser-induced Superplasticity’, *Nano Letters*, 2018, 18(6), 3616–3622. — **Media Highlights**.
8. A. Pal, H.E. Cuellar, R. Kuang, H.F.N. Caurin, **D. Goswami**, and R.V. Martinez: ‘Self-Powered, Paper-Based Electrochemical Devices for Sensitive Point-of-Care Testing’, *Advanced Materials Technologies*, 2017, 2(10), 1700130. — **Media Highlights**.
7. **D. Goswami** and S. Chakraborty: ‘Multi-objective optimization of electrochemical discharge machining processes: a posteriori approach based on bird mating optimizer’, *OPSEARCH*, 2017, 54(2), 306–335.
6. **D. Goswami** and S. Chakraborty: ‘A Study on the Optimization Performance of Fireworks and Cuckoo Search Algorithms in Laser Machining Processes’, *Journal of the Institution of Engineers (India): Series C*, 2015, 96(3), 215–229.
5. **D. Goswami** and S. Chakraborty: ‘Parametric optimization of ultrasonic machining process using gravitational search and fireworks algorithms’, *Ain Shams Engineering Journal*, 2015, 6(1), 315–331.
4. **D. Goswami** and S. Chakraborty: ‘Differential search algorithm-based parametric optimization of electrochemical micromachining processes’, *International Journal of Industrial Engineering Computations*, 2014, 5(1), 41–54.

3. R. Mukherjee, **D. Goswami**, and S. Chakraborty: ‘Parametric Optimization of Nd:YAG Laser Beam Machining Process Using Artificial Bee Colony Algorithm’, *Journal of Industrial Engineering*, 2013, Article ID: 570250.
2. D. Barman, **D. Goswami**, and B. Kundu: ‘An optimum longitudinal wet fin without the length-of-arc assumption’, *HVAC&R Research*, 2013, 19(4), 444–456. [Also presented at 2014 ASHRAE Winter Conference, New York, USA].
1. S. Mukherjee, **D. Goswami**, and B. Roy: ‘Solution of Higher-Order Abel Equations by Differential Transform Method’, *International Journal of Modern Physics C*, 2012, 23(9), 1250056.

Book Chapters

1. P. Bandyopadhyay, **D. Goswami**, N. Biswas, A. Dey, and A.K. Mukhopadhyay: ‘Contact Issues in Brittle Solids’, in ‘*Nanoindentation of Brittle Solids*’, (eds. A. Dey, et al.), 2014, Boca Raton, FL, CRC Press. ISBN 9781466596900.

Conference Papers

2. T. Hildebrandt, **D. Goswami**, and M. Freitag: ‘Large-Scale Simulation-Based Optimization of Semiconductor Dispatching Rules’, *Proceedings of the Winter Simulation Conference*, Savannah, GA, USA, 2014, 2580–2590, IEEE Inc.
1. **D. Goswami** and S. Chakraborty: ‘Optimal Process Parameter Selection in Laser Transmission Welding by Cuckoo Search Algorithm’, *Proceedings of the International Conference on Advanced Engineering Optimization Through Intelligent Techniques*, Surat, Gujarat, India, 2013, 40–44.

Manuscripts (Submitted or in Preparation)

3. **D. Goswami**, Y. Zhang, S. Liu, O.A. Abdalla, P.D. Zavattieri, and R.V. Martinez: ‘Mechanical Metamaterials with Programmable Compression-Twist Coupling’.

2. **D. Goswami**, S. Lin, P.C. Jenkins, and R.V. Martinez: ‘3D-printed Bioresorbable Surgical Instrumentation to Improve Rib Fixation’.
1. **D. Goswami**, J.C. Munera, A. Pal, and R.V. Martinez: ‘Roll-to-roll Fabrication of Flexible Metasurfaces using Low-Cost Laser Diode Engravers’.

Intellectual Property

2. R.V. Martinez and **D. Goswami**: ‘Continuous Laser Nanoforming Device’, *Provisional U.S. Patent Application No. 62/819,706*, Filed: March 18, 2019, Assignee: Purdue Research Foundation. [Public Abstract](#)
1. **D. Goswami** and R.V. Martinez: ‘Flexible, Soft Robots’, *Provisional U.S. Patent Application No. 62/780,400*, Filed: December 17, 2018, Assignee: Purdue Research Foundation. [Public Abstract](#)